Title
The Mechanoregulation of the Actin Cytoskeleton

Author
Jreij, Pamela

Publication Date
2016

The Mechanoregulation of the Actin Cytoskeleton

By

Pamela Jreij

A dissertation submitted in partial satisfaction of the

requirements for the degree of

Joint Doctor of Philosophy
with University of California, San Francisco

in

Bioengineering

in the

Graduate Division

of the

University of California, Berkeley

Committee in charge:

Professor Daniel A. Fletcher, Chair
Professor Sophie Dumont
Professor Matthew D. Welch

Summer 2016

The Mechanoregulation of the Actin Cytoskeleton

by Pamela Jreij

Abstract

The Mechanoregulation of the Actin Cytoskeleton

by

Pamela Jreij

Doctor of Philosophy in Bioengineering

University of California, Berkeley

Professor Daniel A. Fletcher, Chair

The actin cytoskeleton is essential for maintaining mechanical integrity of cells and tissues and for providing structural support during dynamic processes including migration, endocytosis and cytokinesis. From a molecular perspective, it consists of (1) actin monomers polymerized in double helical filamentous structures and (2) an ensemble of regulatory proteins that regulate shape and function of actin structures. From a mechanics perspective, the cytoskeleton is a dynamic entity that can generate force while being subject to various load perturbations. Though molecular understanding of actin networks is extensive, our understanding of how molecular signaling is converted to force output and how force input feeds back into molecular activity remains limited. The goal of this dissertation is to investigate how the interplay between molecular and mechanical attributes of the actin cytoskeleton results in desired cellular activity and physiological phenotypes.

We first focus on the leading edge of migrating cells where nucleation of branched actin structures is involved in membrane protrusion. In chapter 2, we investigate the effect of the biochemical composition of these structures on the observed dynamic properties of network growth. To do so, we reconstitute branched actin network assembly using a minimal set of essential proteins (i.e. nucleation promoting factors, ARP2/3 and capping proteins) and evaluate their role over a broad range of concentrations. We find that in the absence of opposing force, changes in the nanomolar range of soluble protein concentration significantly modulates architectural and kinetic properties of nucleating actin structures.

In cells, branched actin networks do not just transmit forces in the form of protrusion but also resists opposing load imposed by the membrane and other physical barriers. In chapter 3, we use atomic force microscopy to study the impact of external force on the biochemical composition and mechanical properties of reconstituted branched actin structures. Interestingly, we find that mechanical loading alters network density and

composition, which in turn modulates its bulk mechanical properties and renders it stiffer, more powerful and efficient.

Central to assembly and function of actin networks is the activity of actin binding proteins. We next extend our investigation to ask whether forces on actin filaments can influence actin binding protein (ABP) localization and activity in the cytoskeleton. Despite sharing the same cytoplasm, ABPs in cells spatially segregate and differentially regulate actin structures. In the context of the leading edge of migrating cells, cofilin binds and severs filaments in the lamellipodia, whereas tropomyosin is secluded as it binds and stabilizes filaments in the lamellum. In chapter 4, we hypothesize that these proteins are mechanosensitive and show that cofilin preferentially binds to network structures subject to compression whereas tropomyosin favors relaxed structures.

Lastly, in chapter 5, we explore the sensitivity of calponin homology domain-containing proteins to the mechanical state of actin filaments. We focus our study on wild type and mutated versions of the utrophin actin binding domain, which is used as a universal actin marker. Using a multiscale biophysical approach, we show that mutant utrophin can selectively bind highly stressed actin filaments in vitro and in cells. We use this mutant to develop a ratiometric actin mechanosensor for mapping physiological forces in-vivo which provides a new tool for exploring mechanoregulation of cellular processes. Overall, the findings in this dissertation provide direct evidence for the importance of mechanical perturbations in regulating structure and function of the actin cytoskeleton.

Dedicated to my mom

Table of Contents

Acknowledgements

I feel very fortunate to have been a member of the UC Berkeley/UCSF BioE community and especially the Fletcher lab! My experience over the past five years would not have been the same without the support, friendship and mentorship of several people. While I am thankful for every single one of them, I would like to take a moment and acknowledge a few that have shaped the incomparable time that I spent in graduate school.

First and foremost, I would like to thank my adviser Dan Fletcher. I have always been amazed by Dan's flexibility in adapting to our personal scientific interests while constantly encouraging us to think out of the box and nurturing our scientific curiosity. Even when I first joined the lab, Dan gave me the freedom to explore what I am interested in and provided me with the resources and needed guidance to pursue very challenging projects. Dan has not only been a scientific role model but also a great manager continuously ensuring we each reach our potential and gain the experiences and tools we need to fulfill our individual goals. This has created a very positive and collaborative environment in a multidisciplinary lab that was reflected on a daily basis through the excitement and happiness of each one of us. Dan's mentorship has not only been critical to my academic training but also to my preparation for my next career steps. I am very grateful for his openness and unique support in allowing me to explore career opportunities and ensuring that I am ready to move on to my next career step. I have learned tremendously from Dan's leadership and management style and can only wish that one day I will be as good of a manager!

I have had the great opportunity to work closely over the past two years with Andrew Harris. I have learned tremendously from witnessing Andrew's approach to tackling complex scientific questions and his enthusiasm for exploring new ideas. Collaborating with him and bouncing ideas on a daily basis have rendered my last two years in research intellectually stimulating while being simultaneously fun. Working with Andrew has greatly impacted my graduate research experience, and for that I am very grateful!

I am also very thankful for the opportunity to work alongside two post-docs Tai-De Li and Peter Bieling during my first two years in the lab. Peter and Tai-De's excitement and dedication to challenging experimental tools in order to address very complex scientific questions has been highly influential and contagious. Their guidance and introduction to force microscopy and the art of biochemistry among many others have been invaluable to my scientific training.

Despite the turnover of people, the culture in the Fletcher lab has always been a highly collaborative and supportive one. Being surrounded by a group of highly creative and talented scientists has rendered working in lab even more stimulating and fun. I have enjoyed scientific and non-scientific conversations and have learned a lot from each lab member in the past four years. I have especially enjoyed learning from and sharing grad school experiences with my BioE labmates: Matthew Bakalar, Carmen Chan, Daniel Friedman, Ari Joffe, Win Pin Ng and Arunan Skandarajah. I am also thankful for the advice and scientific guidance of current labmates: Brian Belardi, Marijia Podolski, Benjamin Ricca, Eva Schmid, Sungmin Son, Mike Vahey and lab alumni: Alba Diz-Munoz, Gautham Venugopalan and Kevin Webster. Their support and feedback have been invaluable in guiding my research, addressing experimental challenges and interpreting findings. In addition to the great depth of scientific knowledge and expertise in the lab, I have had the opportunity to witness hands on technological advances in software and hardware through the CellScope technology. I am thankful for the CellScope team: Mike D'Ambrosio, Frankie Myers, Clay Reber and Neil Switz, for all the fascinating demos and discussions on the use of optical systems for diagnostics and educational purposes. Outside of the lab, I have had the opportunity to work with and learn from several researchers at UC Berkeley and UCSF. I am especially thankful for collaborations and discussions with Evan Wang and Hengameh Shams.

I would also like to thank members of my dissertation committee Sophie Dumont and Matt Welch as well as members of my qualifying exam committee Sanjay Kumar, David Drubin and Zev Gartner. Their guidance and feedback has been essential to my thesis project and for ensuring my progress in graduate school.

My time in the BioE program would not have been the same without my classmates, cohort of 2011, my various housemates especially residents of the BioE mansion and members of our bioengineering student association with whom I have celebrated many holidays, explored the Bay Area and shared several grad school experiences. I am also very grateful for all the support from the BioE staff especially Kristin Olson and Stephanie Eistetter who have been of great help in dealing with several administrative issues.

There is no better distraction from the misery of failed experiments than a Lebanese party! I am very fortunate to have been surrounded by members of the Lebanese community in the Bay Area who have constantly reminded me of the importance of work life balance and the warmth of social gatherings. To all members of the Sahyoun clan especially Najat Sahyoun, Tania and Andrew Darzi, I am very fortunate to be adopted into your family and to have shared with you so many memorable milestones. You have made me feel at home!

To all my cousins in the States and in Lebanon, you have been a great support system. I will always be thankful for all your encouragement and support in juggling various responsibilities. I am especially thankful to Theresa Khouri and Rosie Khouri Najm whose continuous advice has been indispensable to ensuring my wellbeing in graduate school. Lastly, to my amazing family: Marie Khoury, Ziad Yasmine, Eliane Jreij and Georges Jreij, thank you for continuously going out of your way to help me achieve anything I set my mind to. You have, each in your own way, made sure I overcame every single challenge and kept me grounded throughout. A special thank you to my fearless mom whose resiliency has been a true inspiration! You dedicated your life to get us where we are today despite all the hurdles. For that, all what you have done and everything you taught me, I will be forever grateful!

Chapter 1 – Introduction

Conversion of Mechanical Signals into Biochemical Signals by the Actin Cytoskeleton

Actin is one of the most abundant proteins in eukaryotes and an essential element of the cytoskeleton (Pollard, 2003). In its monomeric form, the protein is a globular structure with four subdomains and 43 kDa in size. Actin monomers can polymerize and form a double helical filamentous structure that is polar, with monomers elongating its barbed end and dissociating from its pointed end (Bugyi, 2010; Carlsson, 2010).

In a cellular context, these filaments assemble to form higher order structures including branched structures, parallel bundles, and crosslinked cortical networks (Blanchoin, 2014). Each structure results in a unique function that is critical for normal physiological behavior. In fact, actin is essential to several biological processes including migration, endocytosis, phagocytosis and cell-cell adhesion (Olson, 2010).

Despite knowledge of the molecules important for the actin cytoskeleton and their biochemistry, our understanding of how a structural element such as the actin filament can fulfill a wide range of biochemical functions remains limited. A major gap in understanding is in the mechanoregulation of the actin cytoskeleton – how forces influence the organization and composition of actin networks. In this introductory chapter, we explore the structural diversity of actin filaments and the potential role of its polymorphism in modulating its interactions with regulatory proteins. We further overview recent findings and hypotheses of how mechanical signals are converted into biochemical signals by the actin cytoskeleton.

I - Structural diversity of actin filaments

I.1. Actin filament as a semi-flexible polymer

Actin filaments dynamically respond to external perturbations imposed by physical barriers (e.g. membranes) and molecular entities (e.g. myosin). With characteristic persistence lengths around the same order of their contour lengths, they act as semi-flexible polymers and undergo thermal fluctuations.

Under compressive and transversal forces, filaments bend and buckle when the applied force exceeds Euler's buckling force. The latter is proportional to the filament's flexural rigidity. In fact, several biophysical studies have been dedicated to characterizing the mechanical properties of an actin filament. Based on fluctuation spectrum of filaments due to thermal motion, Gittes et al. determined the flexural rigidity to be in the order of $7.3*10^{-26}$ $N.m^2$ (Gittes, 1993). Optical tweezers systems have also been used to assess filament's torsional rigidity based on its Brownian motion. Actin is compliant under twisting and bending motion, but exhibits low resistance to torsion with its breaking point decreasing from 600 pN to 320 pN (Tsuda, 1996).

Under tensile forces, filaments can stretch and extend beyond their end-to-end distance. Their extensibility profile captured by a Worm Like Chain (WLC) model has been characterized by two regimes. The first is non-linear and dominated by an entropic component due to the dampening of filament's fluctuations. In the second phase, linear behavior captures filament's extension as it approaches its contour length. This enthalpic response is due energy dissipation upon mechanical stretching of internal bonds (Liu, 2002).

In sum, defining the mechanical profile of an actin filament as a single material can be achieved using traditional physical approaches such as rheology, optical tweezers, microneedle manipulation etc. These readouts highlight the dynamic properties of an actin filament, yet they remain a manifestation of a bulk behavior and fail to capture filament's response at the actin binding protein (ABP) scale.

I.2. Filament polymorphism at the ABP binding scale

In order to understand how mechanical signals get converted to biochemical signals, the biological system needs to be understood at the scale of mechanical perturbation, biochemical response in addition to intermediate scales. In the context of actin mechanics, this spectrum spans micrometer scale perturbations and their impact on filament fluctuations in addition to nanometer scale polymorphism and its impact on filament twist. In this section, we discuss the structural diversity of actin filaments under various biochemical and mechanical conditions.

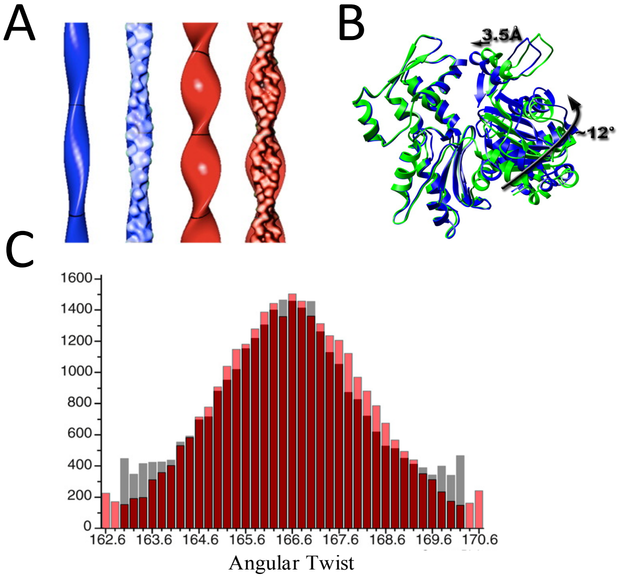

Figure 1: Intrinsic and ABP induced polymorphism of actin filaments
A: Decrease in crossover length upon cofilin binding (McCullough, 2008), B: Fimbrin induced shift in actin subdomains 1 and 2 arrangements (Galkin, 2008), C: Simulation (red) and experimental data (grey) showing variability in filament twist (Galkin, 2012) (adapted with permission from Elsevier)

I.2.a. Intrinsic structural diversity

The traditional notion of an actin filament is that it is a double helical strand with an angular twist of ~167°, ~9 nm width and ~27.3 Å rise/subunit. Meanwhile it has been highly debated whether these values are fixed and depict the static state of an actin filament or whether they are a resulting average of an ensemble of conformations. For multiple decade, electron microscopy, staining and various computing techniques have been employed to challenge the limits in imaging resolution and capture the intrinsic structural properties of an actin filament.

Using electron micrographs of negatively stained filaments and advanced computing approaches, Egelman et al. proposed a polymorphism model where the rise per subunit is maintained constant while the subunit rotation is variable resulting in an ensemble of structural states with highly variable crossover distances (Egelman, 1982). This model was challenged by Fujii et al. who resolved the filament structure down to 6 Å resolution using electron cryomicroscopy. The variance in twist of the resolved structure was shown to be less than a degree, suggesting that actin filaments exists in a single structural state under thermal motion (Fujii, 2010). The observed lack of flexibility has been subsequently proposed to be an artifact of the sample preparation approach (Galkin, 2012). In fact, a high resolution actin structure has been similarly advanced by Galkin et al. The resolved structure supports the polymorphism model and shows that flexibility in subdomain 2 of actin monomers could be at the origin of the various structural states that a filament can adopt (Galkin 2010).

While capturing the naked actin filaments in its natural state has been challenging, imaging of decorated, aged or stretched filaments have consistently supported models in which the actin filament can adopt multiple conformations. These findings are further discussed in the following sections.

I.2.b. Impact of ABP binding on structural diversity

Binding of regulatory proteins to actin filaments has been shown to drive changes in the filament conformation, further supporting the idea that actin filaments are not static structures (McGough, 1998). In fact, modulation of filament's helical twist and/or persistence length by ABPs has been demonstrated as early as 1987 when Stokes et al. investigated the effect of tropomyosin, troponin and myosin binding on the angular disorder in the filament. Tropomyosin/Troponin didn't affect filament twist. Meanwhile, myosin S1 reduced its twist variability, an effect that was subsequently hypothesized to be due to binding protein interactions leading to steric hindrance or to the actin-ABP bond locking the filament in place (Stokes, 1987).

While some proteins have been shown to stabilize actin, cofilin has been extensively studied for its effect in increasing filament flexibility. In fact, cofilin has been demonstrated to change the filament crossover length from 365 Å to 270 Å by changing the subunit angular twist (McGough, 1997). This increase in twist is further manifested in anisotropy measurements that shows decrease in torsional rigidity of cofilin decorated filaments (Prochniewicz, 2005). Flexural rigidity has also been shown to decrease by more than 75% in addition to the persistence length which is reduced down to 2.2 μm from 9.8 μm (McCullough, 2008). The implications of these findings are two-fold. First, given the cooperative nature of cofilin binding to filaments, local structural changes to the filament could propagate to a global level. Second, increasing filament twist could serve cofilin's physiological severing activity by lowering the energy barrier needed for filament breakage.

In addition to cofilin, proteins containing calponin homology domains have been shown to modulate filament's conformation by rearranging monomeric subdomain positions. Fimbrin's actin binding domain 2 (ABD2) which consists of the CH3 + CH4 domains stabilizes the filament and reduces its polymorphism (Galkin, 2008). Furthermore, findings of electron cryomicroscopy images of the N terminus of the protein (N 375) support a model in which changes in subdomain 1 of the actin monomer leads to reorganization of the filament (Hanein, 1997). Similarly, calponin has been shown to drive rearrangement of subdomain 1 towards subdomain 3 when bound to tropomyosin decorated filaments (Hodgkinson, 1997).

The changes in conformations of an actin filament has not only been observed with side binding proteins but also with nucleators and stabilizers. Formin nucleated filaments are thought to exhibit an increase in flexibility that is restored under the stabilizing effects of tropomyosin and myosin binding (Papp, 2006; Ujfalusi, 2009 & Ujfalusi, 2012). Stabilizing toxins such as phalloidin are also expected to counteract such increases in flexibility (Prochniewicz, 2005).

I.2.c. Impact of external force on structural diversity

Structural diversity of actin filaments can also arise from the range of mechanical forces that filaments are subject to in the physiological environment. While it is unclear how microscopic structure is coupled to macroscopic forces, both are expected to contribute to the filament’s conformation.

Recently, with the goal of developing a “bio-nano strain gauge”, Shimozawa & Ishiwata provided supporting evidence for structural rearrangement of stabilized filaments under tension. Using labeled actin as the imaging probe, they showed that independent of photobleaching effects, the fluorescence intensity can decrease by 6% when the filament is tensed beyond the minimal straightening force (~5 pN) (Shimozawa, 2009). This potential for structural diversity under force has been directly addressed by MD and SMD simulations of a 14 subunit long actin filament under tension. Under tensile forces below the breaking point (~200 pN), the filament’s torsional stiffness increased while its twist decreased by 20^{o} (Matsushita, 2011).

In sum, our understanding of how large scale mechanical perturbations correlate with structural diversity of an actin filament remains limited due to lack of tools that can simultaneously capture multiscale spatiotemporal responses. Advances in experimental approaches and development of new models could help elucidate the relationship between force, filament fluctuation and filament twist. Due to the cooperative nature of binding proteins to actin filaments, we expect ABPs to sense variations in mechanical state of these filaments not only at the single binding site level but also whole filament level.

How do ABPs respond to these various mechanical states of the actin filament? We will focus the discussion in the following section on recent findings of conversion of mechanical signals to biochemical activity of ABPs through their binding and regulation of actin structures.

II- Mechanosensitive binding of ABPs to structurally diverse filaments

The actin filament is a dynamic structure that serves as a binding surface for more than hundred actin regulatory proteins. With limited binding sites on the filament surface, binding and regulation can either be cooperative or competitive. Meanwhile, competition is not always for a given binding site. For example, cofilin/phalloidin and cofilin/tropomyosin binding to the actin filament is competitive. While the local binding sites of these proteins are different, they have been shown to preferentially bind to filaments of various mechanical states (McGough, 1997). In this section, we explore potential for direct coupling between the mechanical state of an actin filament and binding of regulatory proteins. To do so, we will first map out physiological forces that actin structures are subject to in a cellular environment. We will then discuss recent findings of mechanosensitive binding and regulation of ABPs to actin structures.

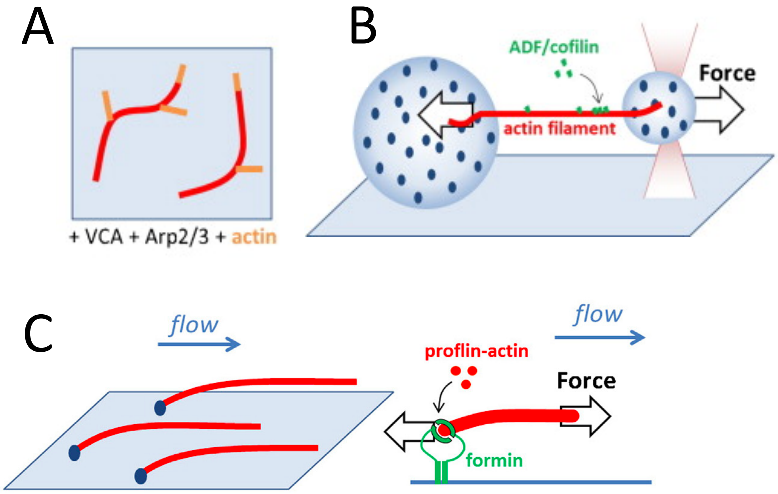

Figure 2: Force regulation of ABP binding and polymerization kinetics
A**:** Actin filament curvature biases Arp2/3 mediated nucleation, B: Cofilin severing activity decreases under tension, C: Formin mediated filament elongation is mechanosensitive (Romet-Lemonne, 2013) (adapted with permission from Elsevier)

II.1. Intracellular forces on actin structures

Several force microscopy techniques such as traction force microscopy have been implemented to estimate force distributions within cells. These approaches remain extracellular with the plasma membrane acting as a physical barrier that can dampen or alter the readout signal. Although the development of fluorescent probes for tracking displacement of actin structures under load yields an internal readout, the conversion of the displacement field thereafter to a force field is limited by modeling assumptions of material properties and anisotropic distributions (Ji, 2008).

Despite challenges in accurately mapping force values intracellularly, rough assumptions can be made. Stress fibers have been a hallmark for actin structures under tension. With a single myosin exerting 3-4 pN of tensile force (Finer 1994), we expect the overall force applied to a stress fiber bundle to be in the range of tens of pN to hundred pN depending on the number of myosin motors acting on the fiber.

Branched actin networks at the leading edge of a cell have been a hallmark for structures under compression. With a membrane resistance of ~ 100 pN/μm (Mogilner, 2002) and a network density of hundred filaments per μm (Grimm, 2003), we estimate the average force per filament to be ~ 1 pN. While the overall branched structure is under compression, single filaments pinned by nucleators within the meshed structure can be subject to a range of axial and transversal mechanical signals that can cause them to bend, buckle or even stretch.

II.2. Preliminary evidence of ABP mechanotransduction

The conversion of a mechanical input to a biochemical signal has been recently explored in the context of mechanosensitive binding of proteins to actin structures. Hayakawa et al. showed that tensile forces of up to 30 pN applied to a single filament in-vitro decreased cofilin severing activity. Scratching assays of a tethered actin mesh further demonstrated a bias in cofilin binding to relaxed filaments. These findings were supported with in-vivo observations of preferential cofilin binding to unstretched actin structures in cells (Hayakawa, 2011).

Force was also found to increase the affinity of myosin II motor domain to filament binding. Preferential binding to stretched filaments was observed under physiological settings and when external perturbations were applied. Building on previous findings of stabilizing effect of myosin on filament structures, Uyeda et al proposed a positive feedback loop model where mechanical perturbations and myosin II binding increase tension in filaments, locking it in a stable structural state to which myosin II favorably binds (Uyeda, 2011).

Bias in protein binding to a mechanical state of actin structures have also been observed with actin nucleators and traditional actin markers. Risca et al. provided evidence that curvature biases branch formation through Arp2/3 mediated nucleation, possibly through a shift in the bending fluctuation spectrum, which is also sensitive to applied tension (Risca, 2012). In correspondence to *Nature*, Munsie et al. challenged the universality of lifeact as actin marker and showed that lifeact does not colocalize with nuclear cofilin decorated actin rods. While cofilin is known to increase flexibility in actin structures, these findings raised the hypothesis of potential mechanosensitive behavior of lifeact and preferential binding to untwisted filaments (Munsie, 2009).

Together these studies suggest that in order for a protein to bind to an actin filament, the helix needs to be locked in a favorable structural state for the protein of interest. This locking mechanism could be induced by force and/or cooperative binding of ABPs capable of modulating the helical conformation.

II.3. Force regulation of polymerization kinetics

One of the most intriguing properties of actin structures is their ability to convert biochemical energy in the form of polymerization kinetics to mechanical work. In the context of formin mediated nucleation, a single filament can exert forces in the range of 0.25-1.3 pN (Kovar, 2004). Arp2/3 mediated actin polymerization at the leading edge exerts protrusive forces and drives cellular motility. Depending on the cell type and biophysical approach, forward protrusive forces can range from hundred piconewtons to couple nanonewtons (Prass, 2006 & Fuhs, 2013).

As each force is opposed by a counterforce, polymerization forces are counteracted by opposing forces of increasing magnitude in a physiological environment. The conversion of these mechanical inputs into biochemical output in the context of polymerization kinetics has been extensively explored using experimental and computational methods.

II.3.a. Formin mediated actin nucleation

The polymerizing activity of FH1 and FH2 domains of formin is modulated by force. In vivo, cells overexpressing formin have a larger pool of F-actin upon release of tension. Formin activation is directly observed in speckle microscopy under microneedle manipulation. This mechanosensitive response is independent of Ca^{2+}, Rho and kinase signaling but depends on profilin activity (Higashida, 2013 and Courtemanche, 2013). In-vitro reconstitution assays of FH1 anchored formins show that in the absence of profilin, application of tensile forces slows down actin polymerization. Meanwhile, the rate of filament elongation increases under tension at optimal profilin concentrations. These effects are reversible and highlight the mechanosensitive response of both the FH1 and FH2 domains of formin (Courtemanche, 2013).

II.3.b. Branched actin networks polymerization

Actin polymerization against an obstacle can affect architectural and dynamic properties of network structure. When growth is opposed by large forces, polymerization reaches a stall. With the goal of understanding the effect of force on the growth velocity of branched actin networks prior to stall, several models have been developed.

The autocatalytic model predicts a load-independent growth behavior. As larger forces are applied to the growing actin structure, new branches are generated. The number of working filaments increases, hence averaging the incremental change in force across the filament population (Carlsson, 2003). An alternative model, the Brownian Ratchet, predicts a strong dependence of velocity on force magnitude. The behavior is biphasic with a sharp decrease at small force ranges. The number of working filaments remains constant during nucleation while the total number of filaments increases (Peskin, 1993 and Mogilner, 2003).

Findings of in-vitro reconstitution assays have raised the question of whether a single theoretical model can sufficiently capture the F-V relationship of branched actin structures. Using a modified AFM system in stiffness-clamp mode and *Xenopus laevis* cytoplasmic extract, Parekh et al. observed force-independent network growth velocity from a functionalized cantilever surface at low forces before a decrease in velocity to stall at high loads (Parekh, 2005). Meanwhile, in extract free assays of purified proteins in force-clamp mode, force-dependent decrease in growth velocity was observed and followed a double exponential decay (Marcy, 2004 and Bieling, 2016). Independent of the exact shape of the F-V curve, force has consistently been shown to modulate branched network growth by affecting polymerization kinetics and/or architectural features.

III- Scope of dissertation

One of the key biological processes where mechanical input is converted to biochemical output and vice versa is cellular migration. In fact, it is the feedback between molecular assembly, load force and activity of actin regulatory proteins that leads to generation of forward motion during protrusion. Our understanding of how these interactions between biochemical and mechanical factors lead to biological function remains limited. With the ultimate goal of investigating how mechanical forces regulate biochemical activity of actin structures, the aim of this thesis is threefold:

1. Evaluating the role of molecular players in driving dynamic assembly of actin structures (Chapter 2)
2. Understanding how mechanical inputs to these structures affect their assembly kinetics (Chapter 3)
3. Assessing the sensitivity of actin regulatory proteins to the actin structures' various mechanical states (Chapter 4 & 5)

References:

1. Egelman E, Francis N and DeRosier D. (1982) F-actin s a helix with a random variable twist. Nature 298: 131 - 135
2. Fujii T, Iwane A, Yanagida T and Namba K. (2010) Direct visualization of secondary structures of F-actin by electron cryomicroscopy. Nature 467: 724 - 729
3. Galkin V, Orlova A, Schroder G, and Egelman E. (2010) Structural Polymorphism in F-actin. Nature Structural and Molecular Biology 17 (11): 1318 - 1324
4. Galkin V, Orlova A, and Egelman E (2012) Actin Filaments as Tension Sensors. Current Biology 22: 96-101
5. Gittes F, Mickey B, Nettleton J and Howard J. (1993) Flexural Rigidity of Microtubules and Actin Filaments Measured from Thermal Fluctuations in Shape. JCB 120 (4): 923-934
6. Liu X, Pollack G. (2002) Mechanics of F-actin Characterized with Microfabricated Cantilevers. Biophysical Journal 83: 2705-2715
7. Tsuda Y, Yasutake H, Ishijima A and Yanagida T. (1996) Torsional rigidity of single actin filaments and actin–actin bond breaking force under torsion measured directly by in vitro micromanipulation. PNAS 93: 12937-12942
8. Shimozawa T. and Ishiwata S. (2009). Mechanical Distortion of Single Actin Filaments Induced by External Force: Detection by Fluorescence Imaging. Biophysical Journal 96: 1036-1044
9. Matsushita S, Inoue Y, Hojo M, Sokabe M and Adachi T (2011). Effect of tensile force on the mechanical behavior of actin filaments. Journal of Biomechanics 44: 1776-1781
10. Stokes et al. (1987). The Variable Twist of Actin and Its Modulation by Actin-Binding Proteins. Journal of Cell Biology 104, 1005-1017
11. McGough A. (1998). F-actin binding proteins. Current Opinion in Structural Biology 8: 166-176.
12. McGough A et al. (1997). Cofilin Changes the Twist of F-Actin: Implications for Actin Filament Dynamics and Cellular Function. J Cell Bio. 138 (4): 771-81
13. Prochniewicz E. et al. (2005). Cofilin Increases the Torsional Flexibility and Dynamics of Actin Filaments. J. Mol. Biol. 353:990-1000
14. Hanein et al. (1997). Evidence for a Conformational Change in Actin Induced by Fimbrin (N375) Binding. Journal of Cell Biology 139, 387-396
15. Galkin et al. (2008). High-resolution cryo-EM structure of the F-actin-fimbrin/plastin ABD2 complex. PNAS 105: 1494-1498
16. Hodgkinson JL et al. (1997). 3-D image reconstruction of reconstituted smooth muscle thin filaments containing calponin: visualization of interactions between F-actin and calponin. J Mol Bio 273:150-159
17. Ujfalusi Z et al. (2012). Myosin and Tropomyosin Stabilize the Conformation of Formin-nucleated Actin Filaments. Journal of Biological Chemistry 287: 31894-31904
18. McCullough B.R. et al. (2008). Cofilin Increases the Bending Flexibility of Actin Filaments: Implications for Severing and Cell Mechanics. JMB 381 (3): 550-558
19. Papp G. et al. (2006). Conformational Changes in Actin Filaments Induced by Formin Binding to the Barbed End. Biophysical Journal 91: 2564-2572

20. Ujfalusi, Z., Vig, A., Hild, G., and Nyitrai, M. (2009) Effect of tropomyosin on formin-bound actin filaments. Biophys. J. 96, 162–168
21. Hayakawa et al. (2011). Actin filaments function as a tension sensor by tension-dependent binding of cofilin to the filament. Journal of Cell Biology 195, 721-727
22. Uyeda et al. (2011). Stretching Actin Filaments within Cells Enhances their Affinity for the Myosin II Motor Domain. Plos One 6 (10)
23. Risca et al. (2012). Actin Filament Curvature Biases Branching Direction. PNAS 109, 2913-2918.
24. Higashida et al. (2013). F- and G-actin homeostasis regulates mechanosensitive actin nucleation by formins. Nature Cell Bio 15: 395-405
25. Munsie L, Caron N, Desmond C and Truant R (2009). Lifeact cannot visualize some forms of stress-induced twisted f-actin. Nature Methods Correspondence 6 (5): 317
26. Ji L, Lim J, and Danuser G (2008). Fluctuations of intracellular forces during cell protrusion. Nature Cell Bio 10 (12): 1393-1400
27. Finer J, Simmons R, and Spudich J (1994). Single myosin molecule mechanics: piconewton forces and nanometer steps. Nature 368: 113 - 119.
28. Kovar D and Pollard TD (2004) Insertional assembly of actin filament barbed ends in association with formins produces piconewton forces. PNAS 101 (41): 14725-14730.
29. Mogilner A and Edelstein-Keshet L (2002). Regulation of Actin Dynamics in Rapidly Moving Cells: A Quantitative Analysis. Biophysical Journal 83: 1237-1258
30. Grimm H.P, Verkhovsky A.B, Mogilner A and Meister J.J (2003). Analysis of actin dynamics at the leading edge of crawling cells: implications for the shape of keratocyte lamellipodia. Eur Biophysical Journal 32: 563-577
31. Fuhs T. et al (2013). Inherently Slow and Weak Forward Forces of Neuronal Growth Cones Measured by a Drift-Stabilized Atomic Force Microscope. Cytoskeleton 70(1):44-53
32. Prass M et al (2006). Direct measurement of the lamellipodial protrusive force in a migrating cell. Journal of Cell Biology 174 (6): 767-772
33. Courtemanche N, Lee J, Pollard TD, Greene EC (2013). Tension modulates actin filament polymerization mediated by formin and profilin. PNAS 110 (24): 9752-9757
34. Mogilner A. and Oster G (2003). Force Generation by Actin Polymerization II: The Elastic Ratchet and Tethered Filaments. Biophysical Journal 84: 1591-1605
35. Peskin C, Odell G and Oster G (1993). Cellular Motions and Thermal Fluctuations: The Brownian Ratchet. Biophysical Journal 65: 316-324
36. Marcy Y, Prost J, Carlier M and Sykes C (2004). Forces generated during actin-based propulsion: A direct measurement by micromanipulation. PNAS 101 (16): 5992-5997
37. Parekh S, Chaudhuri O, Theriot J and Fletcher DA (2005). Loading history determines the velocity of the actin network growth. Nature Cell Bio 7 (12): 1219-1223
38. Carlsson A.E. (2003) Growth Velocities of Branched Actin Networks. Biophysical Journal 84: 2907-2918

39. Bieling P, Li TD, Weichsel J, McGorty R, Jreij P, Huang B, Fletcher DA and Mullins RD. (2016) Force Feedback Controls Motor Activity and Mechanical Properties of Self-assembling Branched Actin Networks. Cell 164: 115-127
40. Olson E. Olson E. & Nordheim A. (2010). Linking actin dynamics and gene transcription to drive cellular motile functions. Nature Reviews Molecular Cell Biology 11: 353-365
41. Pollard T and Borisy G. (2003) Cellular Motility Driven by Assembly and Disassembly of Actin Filaments. Cell 112: 453-465
42. Bugyi B and Carlier MF. (2010) Control of Actin Filament Treadmilling in Cell Motility. Annual Review of Biophysics 39: 449-470
43. Carlsson A (2010) Actin Dynamics: From Nanoscale to Microscale. Annual Review of Biophysics 39: 91-110
44. Blanchoin L, Boujemaa-Paterski R, Sykes C and Plastino J (2014). Actin Dynamics, Architecture and Mechanics in Cell Motility. Physiological Reviews 94 (1): 235-263
45. Romet-Lemonne G, Jegou A. (2013) Mechanotransduction down to individual actin filaments. European Journal of Cell Biology 92: 333-338

Chapter 2

Interplay Between Nucleation, Capping, and Branching in Surface Growth of Branched Actin Networks

This chapter is in collaboration with Peter Bieling, Tai-De Li and Daniel A. Fletcher

Abstract:

At the leading edge of migrating cells, branched actin networks exert protrusive forces through the dynamic machinery of Arp2/3-mediated actin polymerization. Previous studies have shown that network assembly can be reconstituted on nucleation promoting factor (NPF)-coated surfaces from a minimal system of purified proteins including actin, profilin, Arp2/3, and capping protein. Variation in concentrations of these components has produced insight into their biochemical interplay and resulting network structure. However, in most studies to date, the requirement for actin networks growing around beads or bacteria to break symmetry before exhibiting steady-state growth introduces non-uniform stresses that could alter network structure and has limited the range of protein concentrations that could be explored. To investigate branched actin network assembly in the absence of symmetry breaking, we reconstituted branched actin networks on planar glass surfaces using silane-PEG-maleimide chemistry to pattern NPF APVCA domains on defined areas. We followed growth for a broad range of NPF densities, Arp2/3 and capping protein concentrations. Our findings show that the net rate of actin incorporation into the network is independent of changes in NPF density, Arp2/3 concentration, and capping protein concentration, even though network growth rates vary significantly in response to these changes. We estimate internal network stresses and find that they increase with NPF density but decrease with capping protein concentration. Our estimates of nucleation rates, filament lengths, and changes in number of free barbed ends across a range of Arp2/3 and capping protein concentrations suggest a key role of internal stresses in regulating density and growth rate, and they help to constrain predictive models of branched actin network growth.

Introduction:

Actin structures are essential drivers of several biological processes including endocytosis, phagocytosis and cell migration (Rottner, 2010). During cell migration, branched actin networks convert biochemical energy into mechanical work in the form of forward protrusive forces. The assembly and disassembly of these networks have been studied extensively.

When stimulated by an extracellular signal, membrane bound nucleation promoting factors (NPF) get activated and expose their VCA domains. Activated NPF interact with soluble Arp2/3 complex and an existing mother filament to nucleate a new side branch. The free ends of mother and daughter filaments designated as barbed ends serve as a binding site for ATP-bound actin monomers. It is then through the insertion of monomers between elongating filaments and the opposing membrane that the edge is pushed forward. In order to preserve a continuous pool of actin monomers and maintain filaments short and stiff, elongation is terminated by binding of capping proteins to free barbed ends (Pollard, 2003; Pollard, 2009).

This system is sustained and regenerated through disassembly mechanisms. As monomers get incorporated into filaments and age, their nucleotide state is converted from ATP to ADP-Pi then ADP state. Aged ADP-actin monomers dissociate from filaments' pointed end (Bugyi, 2010). While this process takes place following basic dissociation kinetics, it can also be mediated by severing proteins such as cofilin.

Despite the complex dynamic and biochemical footprints of branched actin network growth, it can be reconstituted using a minimal set of essential proteins including NPF, Arp2/3 and capping proteins (Loisel, 1999). While these essential proteins have distinct kinetic effects on the growth dynamics of branched structures, variations in their physiological expression levels can be detrimental and drive pathological effects in vivo. For example, knockdown of Arp2/3 and capping proteins leads to morphological defects in S2 cells (Rogers, 2003). Furthermore, overexpression of capping proteins has been associated with faster migration in pancreatic cancer cells (Thompson, 2007).

Our understanding to date of how the biochemical interplay between these proteins results in network growth remains limited. Several theoretical models have been established with the goal of addressing the effects of nucleation rates, capping rates and opposing force on network growth velocity (Carlier, 1997; Carlsson, 2001 & 2003; Mogilner, 1996, 2002 & 2003). Though these models are extensively developed they remain limited in what they can predict and have raised questions that needs to be addressed experimentally.

On the other hand, while reconstitution of network growth has been achieved on NPF coated bacteria and bead surfaces, these assays remain very challenging and limited in the biochemical conditions they can probe (Wiesner, 2003; Akin, 2008). The need for symmetry breaking further restricts the range of protein concentration that can be tested for and the size of polymerizing surface (Bernheim-Growasser, 2002). Additionally, these structures are grown under conditions of non-uniform stress distributions which could alter network structure (Dayel, 2009; Upadhyaya, 2003).

In this chapter, we aim to address these issues and investigate the relative role of capping protein concentration, NPF density and Arp2/3 concentration in modulating network growth and architecture. Using reconstitution assays in the absence of symmetry breaking, we probe for a large parameter space of concentrations to understand the interplay between essential proteins.

Results:

Reconstitution in the absence of symmetry breaking

Using a minimal system of purified proteins, we have reconstituted branched nucleation on functionalized planar surfaces. Glass surfaces were chemically passivated using silane-peg chemistry and functionalized with a maleimide cross-linker and UV exposure (Walchman, 2011; Bieling, 2010). mCherry Scar APVCA with an N-termini KCK linker was covalently linked to patterned islands and titrated until saturation was reached at 10 μM. For densities lower than 100% NPF, the total surface bound protein was kept at 10 μM and mcherry labeled NPF was supplemented with KCK-dCherry (Supp. Figure 1).

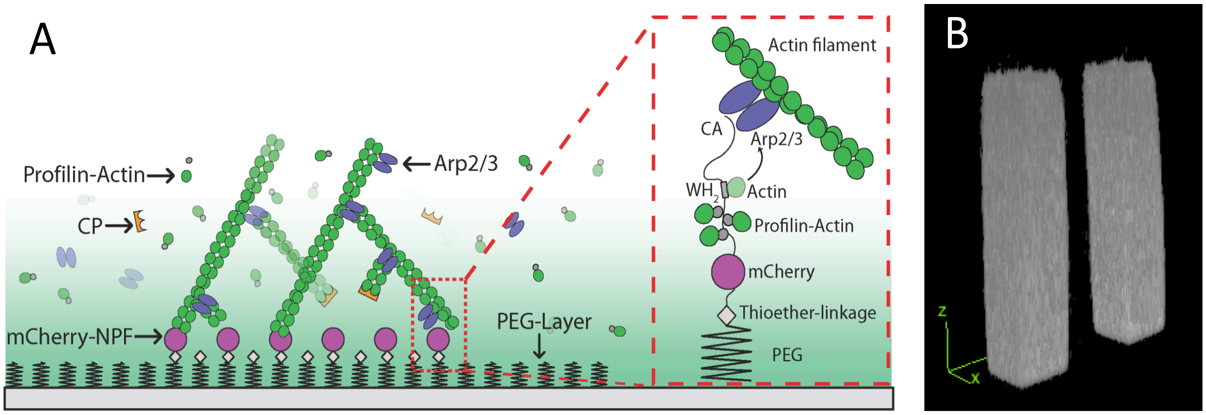

Figure 1: Reconstitution of branched actin structures on planar surfaces
A: Schematic representation of network growth on NPF functionalized surface and in presence of a minimal system of purified proteins. B: 3D Reconstruction of actin networks grown on NPF coated islands

Nucleation was achieved with the minimal set of essential proteins (Figure 1). Actin and profilin concentrations were set at 5 μM. Capping proteins, Arp2/3 concentrations and NPF densities were varied to investigate their role in driving network growth. With the goal of understanding assembly mechanisms, the system was kept void of any severing proteins.

Real time network growth was followed in three dimensions. In the absence of a need for symmetry breakage, we were able to reconstitute assembly on planar islands of varying sizes (2-40 μm). Furthermore, this allowed for probing of a large multi-dimensional parameter space of essential protein concentrations (5-400 nM for capping proteins, 20-500 nM for Arp2/3 and 40-100% NPF density). Growth was sustained for > 1 hr as actin-profilin were available in excess. Taking advantages of these key features, we investigated the individual effect as well as collective interplay between Arp2/3, capping proteins and nucleation promoting factors in driving optimal growth dynamics.

To do so, we tracked the change in height of networks per unit time to measure instantaneous growth velocities and monitored capping protein and actin density throughout the network using a triple color confocal imaging system. The intensity of NPF was limited to the surface and followed a Lorentzian-Cauchy function while the density of actin and capping proteins was constant throughout the network and the fluorescence intensity followed a sigmoidal function (Muhammad, 2010) (Figure 2).

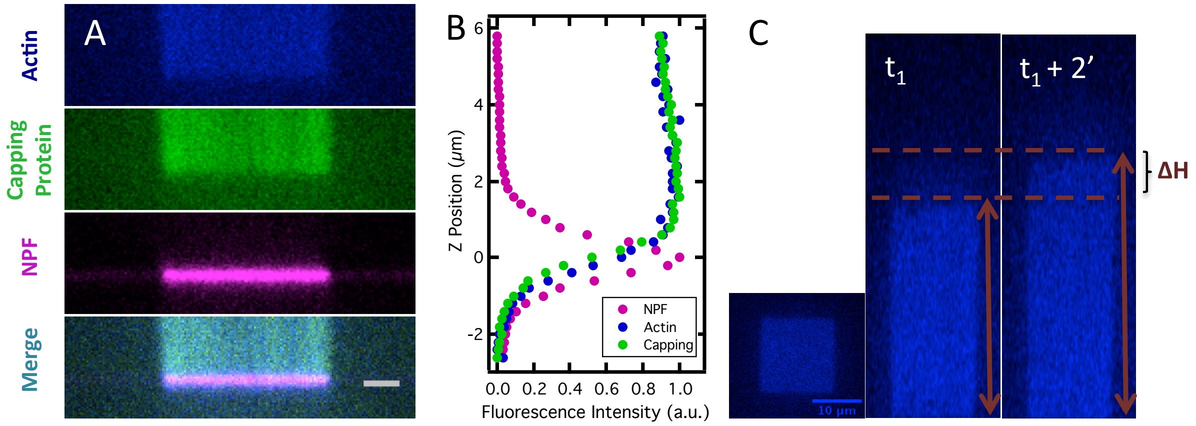

Figure 2: Characterization of kinetic properties of network growth
A: 3 color confocal imaging of alexa-405 actin, alexa-488 capping protein and mCherry-APVCA (Scale Bar: 3μm). B: Variations in fluorescence intensity of NPF, actin and capping proteins relative to nucleating surface (z=0). C: Bottom view and xz projections of an actin network grown on a 14x14 μm^2 island.

__Actin flux is constant despite variable growth dynamics__

The total amount of actin incorporated into the network denoted by actin flux is proportional to the product of the network growth velocity and its actin density. We found that the actin flux is independent of the Arp2/3, capping protein concentrations and NPF density (Figure 3). Although the same amount of actin gets incorporated to the networks per unit time under various biochemical conditions, they exhibit significant differences structurally. In fact, small changes in the nM range of essential protein concentrations can drive changes in the actin density. We see a fivefold decrease at higher capping protein concentrations and an increase with increase in Arp2/3 concentrations and NPF density (Figure 4 and Supp Figure 2).

Furthermore, growth kinetics of these structures are highly dependent on the amount of NPF, capping protein and Arp2/3 present in the assay. An increase in capping protein concentration from 5 nM to 300 nM drives changes in growth velocities from 3 μm/min to 10 μm/min. Meanwhile an increase in Arp2/3 concentration and NPF density result in more than 80% decrease in growth velocities (from 13 μm/min to 2 μm/min) (Figure 5).

These growth velocity profiles are counterintuitive: more pushing ends are expected to be generated under conditions of high nucleating factors (NPF and Arp2/3) hence accelerating growth, while an increase in capping proteins is expected to cap these ends and slow down growth.

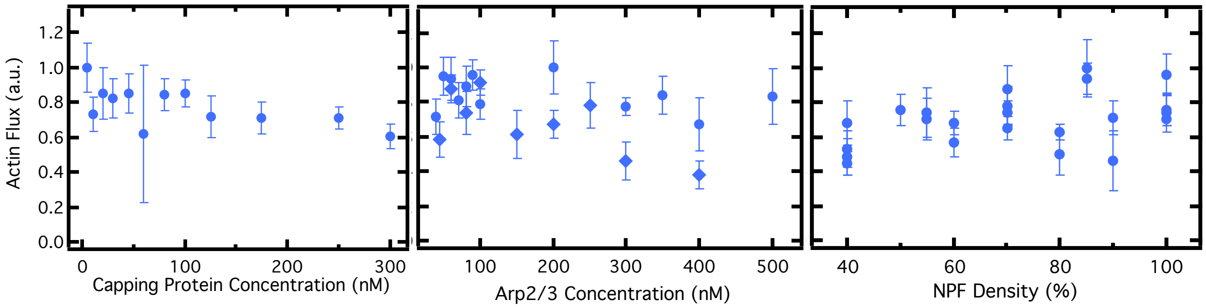

Figure 3: Rate of actin incorporation into the network per unit time (Actin Flux) as a function of Arp2/3, capping protein concentrations and NPF density

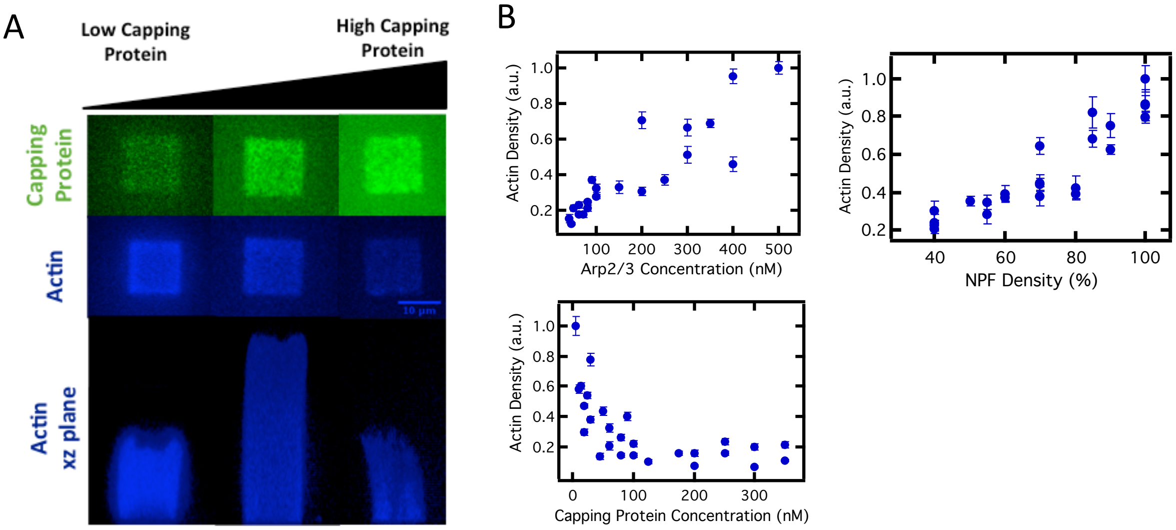

Figure 4: Variations in protein concentrations modulate network densities
A: Planar and side view confocal images of reconstituted actin networks under different concentrations of capping proteins. B: Actin densities as measured by actin fluorescence under variable conditions. NPF density was set at 60% for the Arp2/3 titration where capping protein concentration was 100 nM and for the capping protein titration where Arp2/3 concentration was 100 nM. For the NPF titration, Arp2/3 and capping protein concentrations were 100 nM.

To further understand how the network growth kinetics are modulated, we evaluated the nucleation rates of actin filaments. The nucleation rate is proportional to the product of two measured experimental parameters: growth velocity and capping protein density.

We found that the nucleation rate scales consistently with Arp2/3, capping protein concentration and NPF density (Figure 5). While higher rates of nucleation were expected in presence of higher levels of nucleators, not only did the nucleation rate increase with capping proteins but also the rate of change is much more significant than in the case of Arp2/3 and NPF titrations.

In sum, by reconstituting branched actin network growth on planar surfaces in the absence of symmetry breakage, we are able to investigate the effects of essential proteins (NPF, Arp2/3 and capping proteins) over a broad range of concentrations. Our findings show that variations in the nM range of these proteins lead to significant structural and kinetic changes while maintaining a constant flux of actin into the networks. In the next section, we further investigate these findings and directly probe for the potential role of internal forces in driving distinct network architectures and growth kinetics under various biochemical conditions.

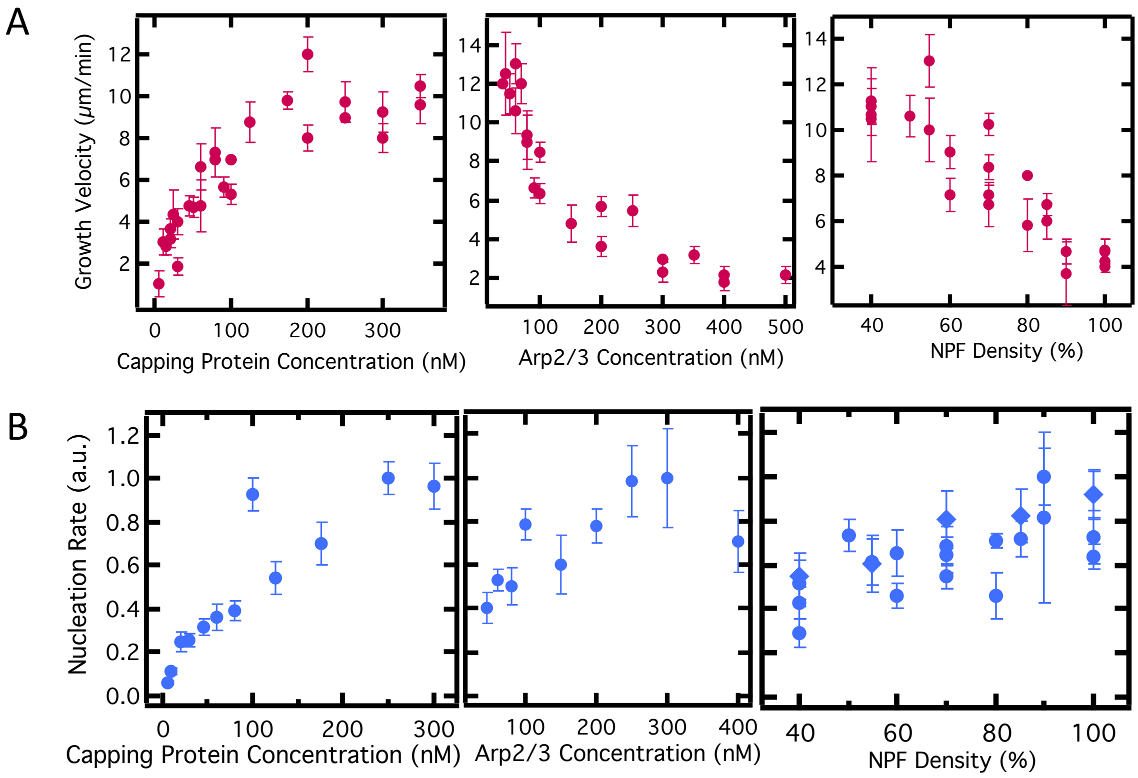

Figure 5: Kinetic properties of reconstituted branched structures are sensitive to nM range changes in essential proteins concentrations
A: Measurements of growth velocities through real time monitoring of network heights as determined by actin channel. B: Estimated measurements of nucleation rates based on network growth velocities and capping protein densities

Internal drag forces drive distinct growth dynamics

For a given load force, the resulting growth velocity, work done against the load force and number of pushing ends are correlated as follows (Peskin, 1993):

$$v = v_0 e^{\frac{-w}{B}}$$

$$v_0 \; = \; k_{on}[A]\delta cos(\theta)$$

$$w \; = \frac{F\delta cos(\theta)}{k_B T}$$

Where v is the measured growth velocity, v_o the free polymerization rate, w the total work done against load force, B the number of filament, k_{on} on-rate of ATP-actin, δ incremental displacement due to actin monomer addition, [A] actin concentration, θ angle that filament forms with normal to surface and F opposing force.

In a physiological environment, these forces can either be external as is the case of membrane resistance or internal due to WH_2-barbed end interactions and/or Arp2/3-NPF-mother filament interactions (Taunton, 2006). In the absence of any external mechanical perturbations, opposing forces in our reconstituted system are limited to internal drag forces generated by interactions between the surface bound nucleation promoting factor and growing network.

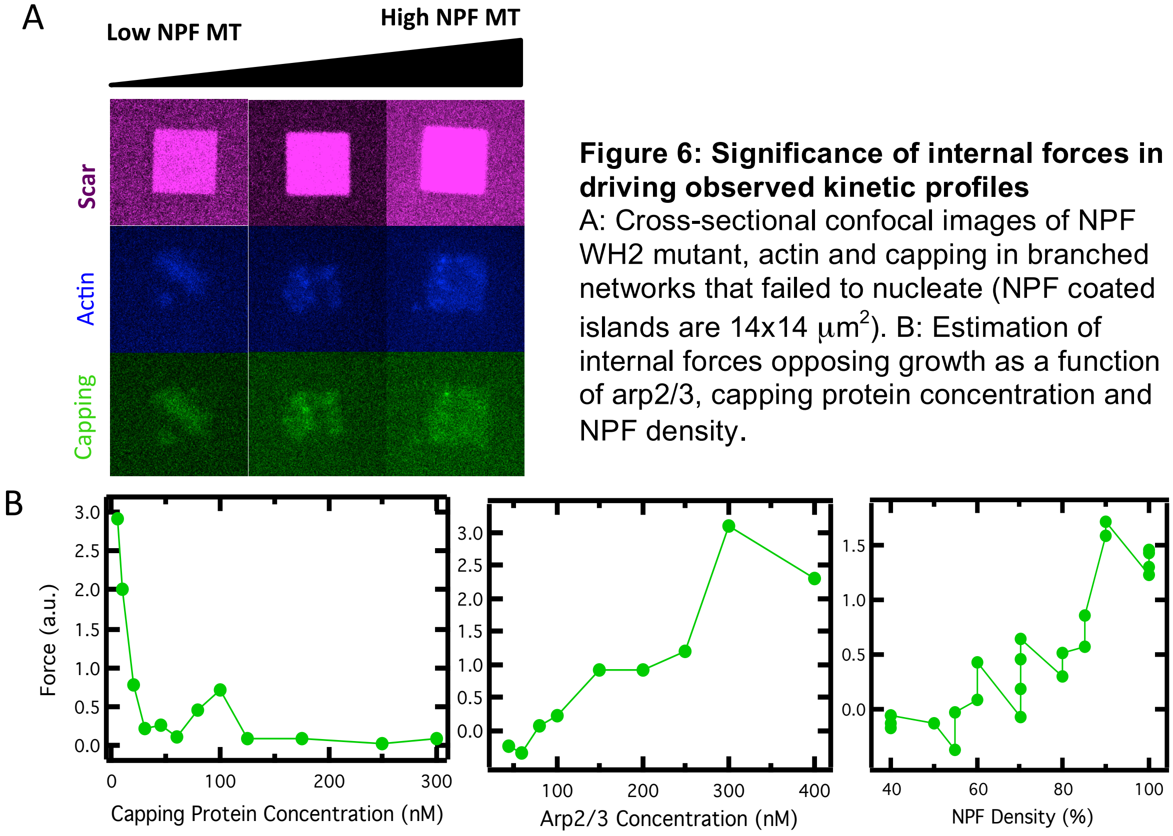

Figure 6: Significance of internal forces in driving observed kinetic profiles
A: Cross-sectional confocal images of NPF WH2 mutant, actin and capping in branched networks that failed to nucleate (NPF coated islands are 14x14 μm^2). B: Estimation of internal forces opposing growth as a function of arp2/3, capping protein concentration and NPF density.

We studied the significance of internal forces and their role in the observed variations of network growth kinetics. To verify the impact of attachment forces on our reconstitution assay, we substituted the WT scar domain with a previously developed mutant (R438A) that exhibits low affinity of binding between the WH2 domain and the filaments' barbed ends (Taunton, 2006). We found that networks not only do not attach to the surface in presence of the WH2 mutant but also fail to nucleate (Figure 6). These findings hold even under high surface density of nucleators and further highlight the significance of attachment forces in the growth of branched actin structures.

Using our experimental measurements of growth velocities and estimates of number of barbed ends, we then evaluated the variation in internal forces under various biochemical conditions. In fact, the rate of change in number of barbed ends is given by:

$$\frac{dB}{dt} = R_{nuc} - R_{cap}B$$

$$R_{cap} = k_{on\_c}[CP]$$

Where B is the number of barbed ends, R_{nuc} the nucleation rate, R_{cap} the capping rate, k_{on_c} on-rate of capping, [CP] concentration of capping proteins. At steady state, the number of barbed ends can be calculated as the ratio of the rate of nucleation and the rate of capping.

Our results show a decrease in internal forces as a function of capping protein concentration. The opposite effect is observed at high conditions of arp2/3 concentration and NPF density (Figure 6). While the amount of Arp2/3 and NPF present at the nucleating surface modulate the frequency of tethering interactions and along with it the magnitude of opposing forces, we explored next whether these forces can explain the changes in network densities. We hypothesize that denser networks are built by packing more filaments per unit volume under drag. We tested this hypothesis by plotting the measured actin densities against the estimated forces for a given set of protein concentrations. Assuming no variations in angular distributions of filaments, our findings show that actin density scales with the internal drag force (Supp Figure 4).

These observations are in support of a model where Arp2/3, capping protein and NPF density alter network growth kinetics by modulating internal forces. At high NPF density and Arp2/3 concentrations, the frequency of tethering interactions is increased. Hence, drag forces are higher and growth is slowed down allowing for more filament to be packed per unit volume since the actin flux is constant. Meanwhile, these tethering effects are released at higher capping protein concentrations as nucleation rates increase significantly. Hence, drag forces are lower and growth is faster leading to lower density of filament packing per unit volume.

Discussion:

Reconstituting branched actin network growth in the absence of symmetry breaking has allowed us to access a large parameter space and understand the interplay between NPF, Arp2/3 and capping proteins in driving network growth and changes in density. While maintaining a constant actin flux, variations in the nM levels of these essential proteins highly modulate growth kinetics in ways that are consistent with changes in internal network stresses.

Role of capping proteins

The effect of capping protein on branched actin structures has been studied in in-vivo and in-vitro settings (Bear, 2002; Sinnar, 2014). While capping has been shown to drive faster motility, two hypothesis have been advanced to explain this behavior. On one hand, the funneling hypothesis supports a model where capping of a population of filaments funnels a larger amount of soluble actin to uncapped ends, the increase in monomer flux can then drive faster growth (Carlier, 1997). On the other hand, the monomer gating model is built on evidence of constant actin flux under different capping protein concentrations. The model suggests that an actin monomer is more likely to be destined to participate in a nucleation event rather than an elongation event as more free barbed ends get capped. The increase of nucleation rates and release of Arp2/3 from tethering interactions at the surface under higher capping concentrations is then manifested at the whole network level in the form of faster growth velocities (Akin, 2008). While no other experimentation has tested either hypothesis (Welch, 2013), our reconstitution assay is the first to explore these models. With a constant flux and an increase in nucleation rates as a function of capping protein concentration, our findings are in agreement with the monomer gating model. We conclude that capping proteins are modulating growth kinetics by increasing the nucleation rate.

Role of Arp2/3 and NPF

The effect of Arp2/3 and NPF on kinetic properties of actin based motility have been previously explored (Pantaloni, 2000; Weisswange, 2009). While some studies have observed NPF-independent growth velocity profiles (Cameron, 1999), others have seen strong correlations when NPF was adsorbed to nucleating surface as well as kept soluble in solution (Bugyi, 2010; Wiesner, 2003). We have explored the impact of NPF on growth dynamics of branched actin structures over a broad range of surface-adsorbed protein concentrations. Our findings show monophasic decrease in growth velocities as a function of NPF density. We also observed a negative correlation between growth velocities and Arp2/3 concentration which is in agreement with previous findings (Akin, 2008).

Role of internal forces

In addition to generating external forces that displace membranes or push bacteria, actin networks can generate internal forces that arise from polymerization-driven forces and filament-mediated binding to the nucleating surface. Our experiments provided an opportunity to test the effects of protein concentration on internal forces without the confounding influences of symmetry breaking and geometry that complicate interpretation of bead and bacterium studies. For a constant concentration of soluble

Arp2/3, more Arp2/3 is released from the nucleating surface at higher capping protein concentrations and fewer drag forces are exerted on the growing structure. Under lower drag forces, networks can grow faster but exhibit lower actin density as the overall actin flux remains constant.

Nucleation promoting factors and Arp2/3 are often thought of solely in the context of their nucleating function, which have served as the basis for several theoretical models (Mogilner, 2002; Grimm, 2003; Tania, 2013). Our findings are in support of a model where NPF and Arp2/3 affect the kinetics of network growth by generating more drag forces rather than amplifying nucleation events. We hypothesis that larger ranges of drag forces are at the origin of slower growth profiles and higher packing densities of actin. This hypothesis is further supported by evidence that inactive PPase-treated Arp2/3 can also slow down growth in bead motility assays (Akin, 2008).

In sum, using a minimalist approach to in-vitro reconstitution, we have shown that it is through the balanced interplay between NPF, Arp2/3 and capping proteins that optimal growth of branched actin networks is driven. Levels of essential proteins need to be high enough to nucleate but not too high to hinder growth. Tipping the balance between these players would lead to abnormal growth kinetics, network architectures and subsequently pathological phenotypes.

Methods:

Cloning and protein purification: For cloning and purification of all proteins, refer to the methods section in Chapter 3 (Bieling, 2016)

Surface functionalization: Surface functionalization and patterning was achieved as described in Bieling et al. (Bieling 2016, Fourniol 2014). Briefly, 22x22 mm^2 coverslips (Zeiss, #474030-9020-000) were stacked in teflon holder and sonicated in 3M NaOH (Sigma) for 15 min. Extensive washing in milliQ then followed. Coverslips were then added to a fresh beaker for piranha wash. Piranha solution was 1x hydrogen peroxide (BDH 30% Stabilized, 7690), 2x sulfuric acid. After a 30 min sonication step, coverslips were washed extensively then stored in milliQ. They were dried and arranged in weighing jars (Fisher, 034205C), sandwiches with one drop GOPTS (Sigma) were then formed. Surface silanization was allowed for 1hr at 75 deg. Separation of silanized surfaces took place in acetone (Sigma, 650501). Following wash and storage in acetone, cleaned coverslips were dried and arranged in weighing jars for Pegylation step. A saturated diamino-PEG (Rapp, 11 2000-21) solution was prepared (150 mg in 500 μL acetone) and 25 μL were added to each coverslip sandwich. The later were stored for 4hr at 75 deg.

After the pegylation step, silane-peg coverslips were washed, sonicated for 3 min in milliQ then washed again in milliQ. Dried slides were then sandwiched with 7.5 μL of 1M b-mercaptoethanol solution (Sigma, M3148) in anhydrous DMF (Sigma, 227056) and incubated at room temperature for 10 min. Next, coverslips were washed, stored in

DMF (Sigma, 270547) then dried. The final functionalization step consisted of adding 25 uL of a saturated BMPS (Fisher, 22298) solution (50 mg of crosslinker in 500 uL anhydrous DMF). The incubation step was 30 min at room temperature and was followed with two wash steps in DMF and final storage in DMSO (Sigma, 67685).
The UV illumination step was achieved using a custom built system (Fourniol 2014). Prior to illumination, masks were cleaned and sonicated in piranha for 30 min then washed extensively in milliQ and dried with N_2. For each assembled mask-coverslip setup, the coverslip was first cleaned in DMSO, ethanol then dried. The mask was cleaned and sonicated for 6 min in SUI solution (NH_3OH:H_2O_2:H_2O 1:4:50), washed extensively with milliQ, rinsed with ethanol then dried with N_2. Illumination of each coverslip lasted 6 min following which the patterned surface was sonicated in ethanol for 2 min, milliQ for 2 min then dried using a spin coater.

A PDMS flow chamber was then assembled and consisted of a counter-slide with two PDMS stripes on each edge to which the patterned coverslip bound. Desired percentage of KCK-mcherry-APVCA was mixed with KCK-dcherry to a final total protein concentration of 10 μM in the following buffer: 20 mM Hepes (pH 7.4), 350 mM NaCl, 1 mM EDTA. Proteins were allowed to bind to surface for 25 min in humidity chambers. They were then washed out and incubated for 3 min using 250 uL wash buffer (20 mM Hepes pH7.4, 350 mM NaCl, 1 mM EDTA and 5 mM b-ME). Wash buffer was finally exchanged with storage buffer (20 mM Hepes pH7.4, 350 mM NaCl, 1 mM EDTA and 1 mM TCEP) and flow chamber was stored in a humid container and stored at 4 deg.

Flow well setup: The flow well setup consisted of the patterned coverslip bound to a PLL-PEG passivated slide using 200 nm thick double-sided tape (Tesa). Briefly, 3''x1''x1mm glass slides (VWR) were cleaned in 1% micro-90, rinsed with milliQ, dried then plasma cleaned. Slides were then coated with PLL-PEG (g = 3.5) prepared as described in Bieling et al. 2010. PLL-PEG passivated counter-slides were finally rinsed with milliQ and stored dry at room temperature.

Reconstitution assay: Flow chamber was initially equilibrated with 50 μL equilibration buffer (100 mM KCl, 10 mM b-ME, 1x MEH, 1 mg/ml b-casein, 1 mM ATP in 20 mM HEPES pH 7.0) in the absence of any soluble proteins and imaged to localize NPF-coated islands. A 20x MEH pre-stock was prepared as follows: 400 mM HEPES pH 7, 30 mM MgCl2 and 20 mM EGTA. Equilibration buffer was then exchanged with 99 μL of reconstitution mix. The reconstitution mix consisted of four premixes:

1. Equilibration buffer (composition as described above)
2. Protein buffer pre-mix: 100 mM KCl, 10 mM b-ME, 1x MEH, 100 μg/mL b-casein and 1 mM ATP in 20 mM HEPES pH 7.0
3. Essential proteins pre-mix: For standard growth assays, Arp2/3 and capping proteins were used at 100 nM final concentration. Alexa-488 capping was used at a 20% labeling ratio. Pre-mix included Arp2/3 and capping proteins at desired concentration in addition to 5 μM profilin in 20 mM HEPES pH 7.0, 100 mM KCl solution.

4. Actin pre-mix: 5 μM final actin concentration in G-buffer (2mM Tris-Cl pH 8.0, 0.2 mM ATP, 0.5 mM TCEP, 0.1 mM CaCl2). Alexa-405 monomeric actin was introduced at 2% labeling ratio.

Imaging: Network growth occurred instantaneously following addition of reconstitution mix to flow well setup. Growth was followed using a spinning disk confocal microscope (Yokogawa CSU10, Zeiss Observer Z1), a 63x 1.4 N.A. oil objective (Zeiss) and a Photometrics Cascade II camera. For each sample, heights of 14x14 μm^2 islands was followed over 3 min. For each time-point, stacks of 1um slices were acquired. For a given pair of network pillars, two instantaneous velocities were measured by tracking displacement in micrometer during one minute. This was repeated for 3 pairs, leading to a total of 6 instantaneous velocities per sample. For actin, capping and NPF density measurements, z-stacks (200 μm frames) were acquired for a total height of 10 μm. This was done for 8 networks, fluorescence intensities were then plotted as a function of distance and curve fitting was performed to determine the constant actin and capping protein fluorescence intensity within the network and peak NPF fluorescence intensity on the surface.

Supplemental Figures:

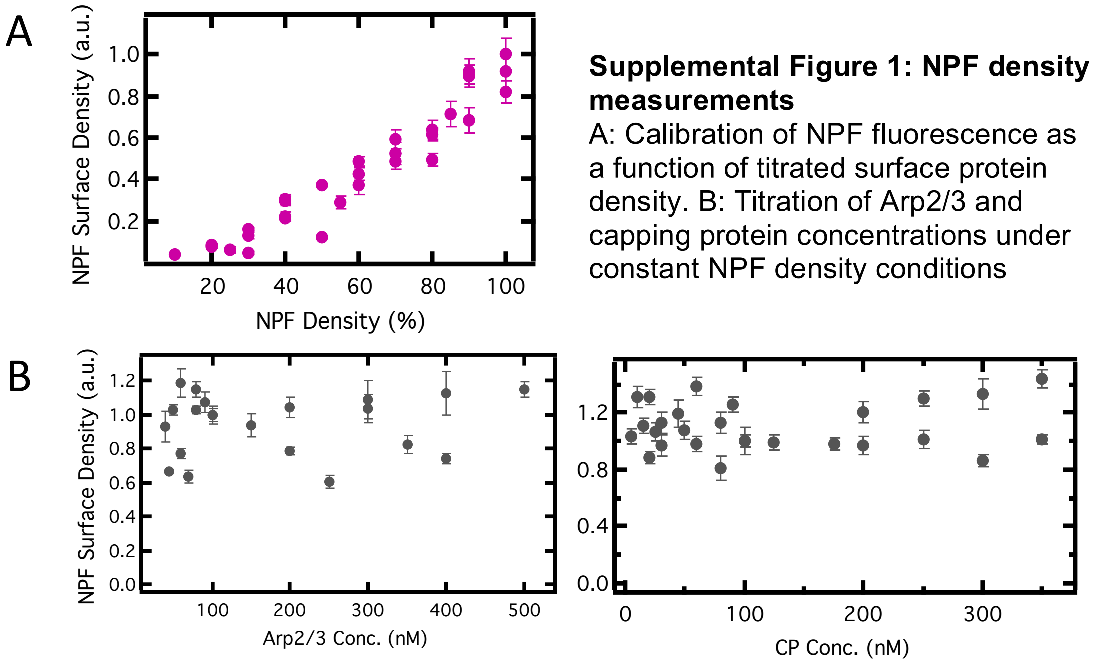

Supplemental Figure 1: NPF density measurements
A: Calibration of NPF fluorescence as a function of titrated surface protein density. B: Titration of Arp2/3 and capping protein concentrations under constant NPF density conditions

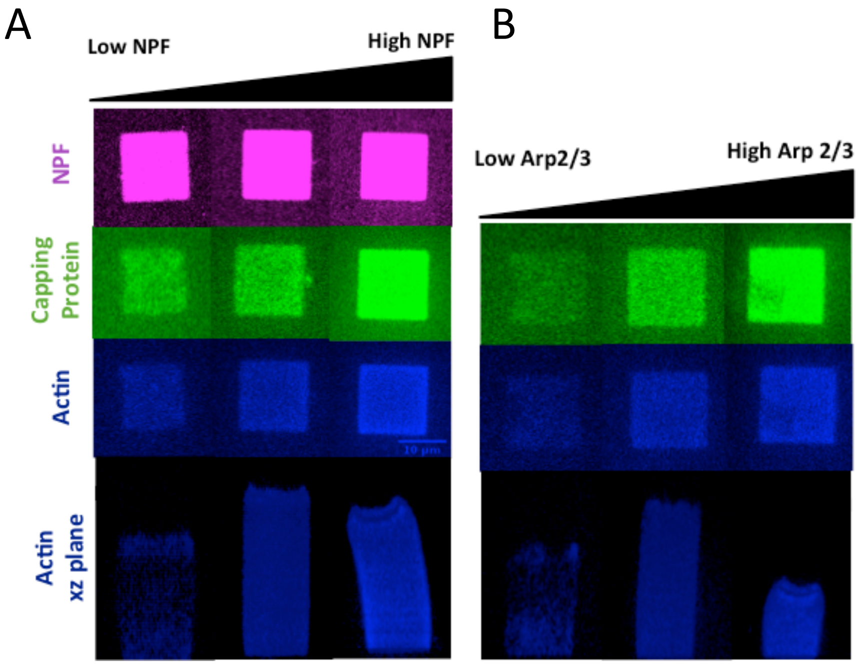

Supplemental Figure 2: Structural Changes in actin networks
A: Variations under different NPF surface density conditions. B: Variations under different soluble Arp2/3 concentrations

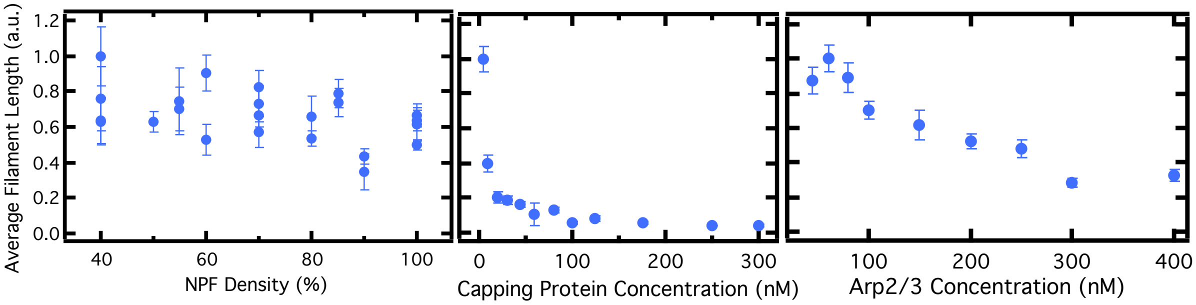

Supplemental Figure 3: Modulation of average filament length based on measurement of actin and capping protein densities

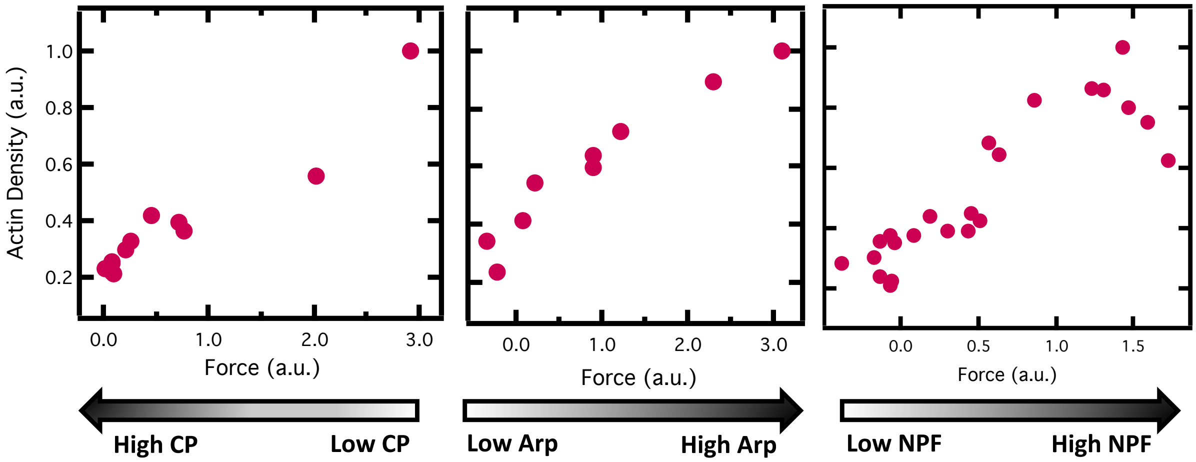

Supplemental Figure 4: Cross-correlation between estimated internal forces and measured actin densities for a corresponding arp2/3, capping protein concentration and NPF density

References:

1. Pollard T and Borisy G (2003). Cellular Motility Driven by Assembly and Disassembly of Actin Filaments. Cell 112: 453-465
2. Bugyi B and Carlier M (2010). Control of Actin Filament Treadmilling in Cell Motility. Annual Review Biophysics 39: 449-470
3. Pollard T and Cooper J (2009). Actin a central player in cell shape and movement. Science 326 (5957): 1208-12
4. Rottner K, Hanisch J and Campellone K (2010). WASH, WHAMM and JMY: regulation of Arp2/3 complex and beyond. Cell 20 (11): 650 - 661
5. Rogers S, Wiedemann U, Stuurman N and Vale RD (2003). Molecular requirements for actin-based lamella formation in Drosophila S2 cells. Journal of Cell Biology 162 (6): 1079–1088
6. Thompson CC et al (2007). Pancreatic cancer cells overexpress gelsolin family-capping proteins, which contribute to their cell motility. Gut 56 (1): 95-106
7. Loisel T, Boujemaa R, Pantaloni D and Carlier M (1999). Reconstitution of actin-based motility of Listeria and Shigella using pure proteins. Nature 401: 613 - 616
8. Upadhyaya A and van Oudenaarden A (2003). Biomimetic Systems for Studying Actin-Based Motility. Current Biology 13:734-744
9. Dayel M, Akin O, Landeryou M, Risca V, Mogilner A and Mullins RD (2009). In Silico Reconstitution of actin-based symmetry breaking and motility. Plos Biology 7 (9): e1000201
10. Wiesner S et al. (2003). A biomimetic motility assay provides insight into the mechanism of actin-based motility. JCB 160 (3): 387-398
11. Carlier M and Pantaloni D (1997). Control of Actin Dynamics in Cell Motility. J. Mol. Biol 269: 459-467
12. Akin O and Mullins RD (2008). Capping Protein Increases the Rate of Actin-Based Motility by Promoting Filament Nucleation by the Arp2/3 Complex. Cell 133: 841-851
13. Mogilner A and Oster G (1996). Cell motility driven by actin polymerization. Biophysical Journal 71(6): 3030-3045
14. Mogilner A and Edelstein-Keshet L (2002). Regulation of actin dynamics in rapidly moving cells: A quantitative analysis. Biophysical Journal 83 (3): 1237-1258
15. Mogilner A. and Oster G (2003). Force Generation by Actin Polymerization II: The Elastic Ratchet and Tethered Filaments. Biophysical Journal 84: 1591-1605
16. Carlsson AE (2001). Growth of branched actin networks against obstacles. Biophysical Journal 81(4): 1907-1923
17. Carlsson A.E. (2003) Growth Velocities of Branched Actin Networks. Biophysical Journal 84: 2907-2918
18. Peskin C, Odell G and Oster G (1993). Cellular Motions and Thermal Fluctuations: The Brownian Ratchet. Biophysical Journal 65: 316-324
19. Co C, Wong D, Gierke S, Chang V and Taunton J (2006). Mechanism of Actin Network Attachement to Moving Membranes: Barbed End Capture by N-WASP WH2 Domains. Cell 128: 901-913

20. Bernheim-Groswasser A, Wiesner S, Golsteyn R, Carlier M, Sykes C (2002). The dynamics of actin-based motility depend on surface parameters. Nature 417: 308-311
21. Sinnar S, Antoku S, Saffin J, Cooper J, Halpain S (2014). Capping protein is essential for cell migration in vivo and for filopodial morphology and dynamics. Mol Biol Cell 25(14): 2152-2160
22. Bear J et al (2002). Antagonism between Ena/VASP Proteins and Actin Filament Capping Regulates Fibroblast Motility. Cell 109: 509-521
23. Welch MD, Way M (2013). Arp2/3 mediated actin based motility: a tail of pathogen abuse. Cell Host Microbe 14: 242-255
24. Pantaloni D, Boujemaa R, Didry D, Gounon P, Carlier M (2000). The Arp2/3 complex branches filament barbed ends: functional antagonism with capping proteins. Nature Cell Bio 2: 385-391
25. Bugyi B, Didry D and Carlier M (2010). How tropomyosin regulates lamellipodial actin-based motility: a combined biochemical and reconstituted motility approach. EMBO 29: 14-26
26. Cameron L, Footer M, van Oudenaarden A, and Theriot J (1999). Motility of ActA protein-coated microspheres driven by actin polymerization. PNAS 96: 4908-4913
27. Weisswange I, Newsome T, Schleich S, and Way M (2009). The rate of N-WASP exchange limits the extent of ARP2/3-complex-dependent actin-based motility. Nature Letters 458: 87-92
28. Bieling P, Li TD, Weichsel J, McGorty R, Jreij P, Huang B, Fletcher DA and Mullins RD. (2016) Force Feedback Controls Motor Activity and Mechanical Properties of Self-assembling Branched Actin Networks. Cell 164: 115-127
29. Fourniol F, Li TD, Bieling P, Mullins RD, Fletcher DA, Surrey T (2014). Micropattern-Guided Assembly of Overlapping Pairs of Dynamic Microtubules. Methods Enzymol. 540: 339-360
30. Bieling P. et al. (2010). Fluorescence Microscopy Assays on Chemically Functionalized Surfaces for Quantitative Imaging of Microtubule, Motor, and +TIP Dynamics. Meth Cell Bio 28: 555-580
31. Muhammad M.S. and Choi T.S. (2010). 3D Shape Recovery By Image Focus Using Lorentzian-Cauchy Function. Proceedings of 2010 IEEE 17th International Conference on Image Processing.
32. Walchman S. et al. (2011). Maleimide Photolithography for Single-Molecule Protein-Protein Interaction Analysis in Micropatterns. Anal. Chem. 83: 501-508.
33. Grimm H, Verkhovsky A, Mogilner A and Meister J. (2003) Analysis of actin dynamics at the leading edge of crawling cells: implications for the shape of keratocyte lamellipodia. Eur Biophysical Journal 32: 563-577
34. Tania N, Condeelis J, Edelstein-Keshet L. (2013) Modeling the Synergy of Cofilin and Arp2/3 in Lamellipodial Protrusive Activity. Biophysical Journal 105: 1946-1955

Chapter 3

Force Feedback Controls Motor Activity and Mechanical Properties of Self-Assembling Branched Actin Networks

Reprinted with permission from Elsevier.
Bieling P, Li Tai-De*, Weichsel J, McGorty R, Jreij P, Huang B, Fletcher DA and Mullins RD. (2016) "Force Feedback Controls Motor Activity and Mechanical Properties of Self-Assembling Branched Actin Networks" Cell 164, 115-127. * Equal Contribution*

Abstract:

Branched actin networks—created by the Arp2/3 complex, capping protein, and a nucleation promoting factor—generate and transmit forces required for many cellular processes, but their response to force is poorly understood. To address this, we assembled branched actin networks in vitro from purified components and used simultaneous fluorescence and atomic force microscopy to quantify their molecular composition and material properties under various forces. Remarkably, mechanical loading of these self-assembling materials increases their density, power, and efficiency. Microscopically, increased density reflects increased filament number and altered geometry but no change in average length. Macroscopically, increased density enhances network stiffness and resistance to mechanical failure beyond those of isotropic actin networks. These effects endow branched actin networks with memory of their mechanical history that shapes their material properties and motor activity. This work reveals intrinsic force feedback mechanisms by which mechanical resistance makes self-assembling actin networks stiffer, stronger, and more powerful.

Introduction:

Cells are physical objects that interact with the world around them by generating, transmitting, and resisting forces (Janmey and McCulloch, 2007; Kasza et al., 2007). In eukaryotic cells, many of these forces flow through the collection of cross-linked, branched, and entangled filament networks that form the actin cytoskeleton (Fletcher and Mullins, 2010; Pollard and Cooper, 2009). Branched actin networks, for example, generate pushing forces (Mogilner and Oster, 1996) required for many cellular processes, including protrusion of leading edge membranes in migrating cells (Bisi et al., 2013; Wu et al., 2012), motility of intracellular pathogens (Welch and Way, 2013), healing of cell ruptures (Clark et al., 2009), endocytosis (Mooren et al., 2012), phagocytosis (Insall and Machesky, 2009), and the formation of tight cell adhesions (Yamaguchi et al., 2005). These dynamic actin networks are created by the branching activity of the Arp2/3 complex, which creates new filaments from the sides of preexisting filaments (Mullins et al., 1998). In addition to the Arp2/3 complex, assembly of force-generating networks requires two accessory proteins: a WASP-family nucleation promoting factor (NPF) and a filament capping protein (Akin and Mullins, 2008). Despite the mechanical nature of their functions, we know little about how branched actin networks respond to force at the molecular or the material level (Chaudhuri et al., 2007; Marcy et al., 2004; Parekh et al., 2005; Pujol et al., 2012). Previous work focused on mechanics of isotropic actin networks held together by entanglement or cross-linking (Stricker et al., 2010), which are dominated by ‘‘entropic elasticity’’ of individual actin filaments (Gardel et al., 2004a; MacKintosh et al., 1995; Storm et al., 2005; Wagner et al., 2006). Theory developed from this work explains effects of ‘‘pre-stress’’ on actin gels (Gardel et al., 2006), but its connection to the dynamic and anisotropic cytoskeletal networks created by living cells remains unclear.

Cells construct actin networks by concentrating assembly factors at specific sites, establishing physical boundary conditions that dictate dynamics and architecture of the network. Filament nucleation and branching by the Arp2/3 complex, for example, creates actin networks that generate force to drive membrane movement (Svitkina and Borisy, 1999; Vinzenz et al., 2012; Wu et al., 2012). Because Arp2/3 activity depends on membrane-associated NPFs, new filaments are created only in a narrow zone adjacent to the membrane. Imposing this boundary condition on filament formation produces anisotropic networks in which most growing filament ends point toward the membrane (Maly and Borisy, 2001; Weichsel et al., 2012) and has profound mechanical consequences. Isotropic networks assembled in vitro from soluble and randomly distributed Arp2/3 complexes are mechanically weak (Nakamura et al., 2002), while networks assembled from surface-immobilized NPFs are more coherent and much stiffer (Chaudhuri et al., 2007; Marcy et al., 2004). Once polarized, growing actin networks encounter obstacles and experience external forces that may affect their assembly.

Here, we ask how mechanical forces affect the biochemical interactions that underlie network assembly, and we investigate how the mechanical history of self-assembling networks affects their material properties and motor activity. To measure molecular and mechanical responses of branched actin networks to force, we applied simultaneous total internal reflection fluorescence (TIRF) and atomic force microscopy (AFM) to actin networks assembled from purified components. To create biologically relevant boundary conditions for network growth, we micro-patterned the surface of glass coverslips with a WASP family NPF. We then quantified incorporation of proteins into growing networks by TIRF microscopy. At the same time, we used an AFM cantilever to apply force and quantify network growth velocity. To understand the functional consequences of biochemical responses to force, we also used the AFM cantilever to measure material properties of branched actin networks grown under different physical and biochemical conditions.

We find that force fundamentally alters the assembly, architecture, and function of branched actin networks: growth velocity decreases while filament density increases in response to force. Microscopically, the increase in filament density reflects two changes: (1) greater number of pushing filaments, and (2) tighter filament packing. Average filament length, however, does not change with force. Interestingly, the fractional energy of polymerization converted into mechanical work increases with applied force. Macroscopically, force on growing actin networks enhances their stiffness and mechanical resilience. Networks exhibit their maximum stiffness when loaded with the same forces they experienced during growth. These force-induced changes in material properties, however, do not scale with density or stress according to ‘‘universal’’ laws derived for isotropic actin gels (Gardel et al., 2004b, 2006). This argues that the physics of Arp2/3-generated actin networks differs fundamentally from that of random, cross-linked networks. Furthermore, we find that assembling branched actin networks under changing load forces produces materials whose stiffness and force-velocity relationships are dominated by their loading history rather than molecular composition.

Results:

Assembly of branched actin networks with physiologically relevant boundary conditions

To mimic enrichment of WASP-family NPFs on cellular membranes, we immobilized the Arp2/3-activating region of WAVE1 on functionalized coverslips (Fourniol et al., 2014) (Figure 1A). We then added purified components—monomeric actin, Arp2/3 complex, and capping protein (CP)—to the WAVE1DN patterns to create polarized actin networks. To prevent spontaneous nucleation, we also added the actin-binding protein profilin (Pantaloni and Carlier, 1993; Tilney et al., 1983). By confocal fluorescence microscopy, networks formed three-dimensional ‘‘pillars’’ growing from WAVE1DN-coated squares (Figure 1B) at 7.33 ± 1.61 mm/min (Figure S1A), at a rate comparable to actin assembly at the leading edge of migrating cells (Renkawitz et al., 2009). Growth velocity did not strongly depend on NPF pattern size, indicating that network assembly is not limited by diffusion (Figure S1B). Because <0.01% of the coverslip is coated with the NPF, network growth did not significantly deplete the pool of soluble protein components, and the filament networks grew with constant density and velocity for more than an hour (Figure S1C). The distribution of fluorescent Arp2/3 (not shown) and CP (Figures 1C and 1D) were also homogeneous throughout the networks.

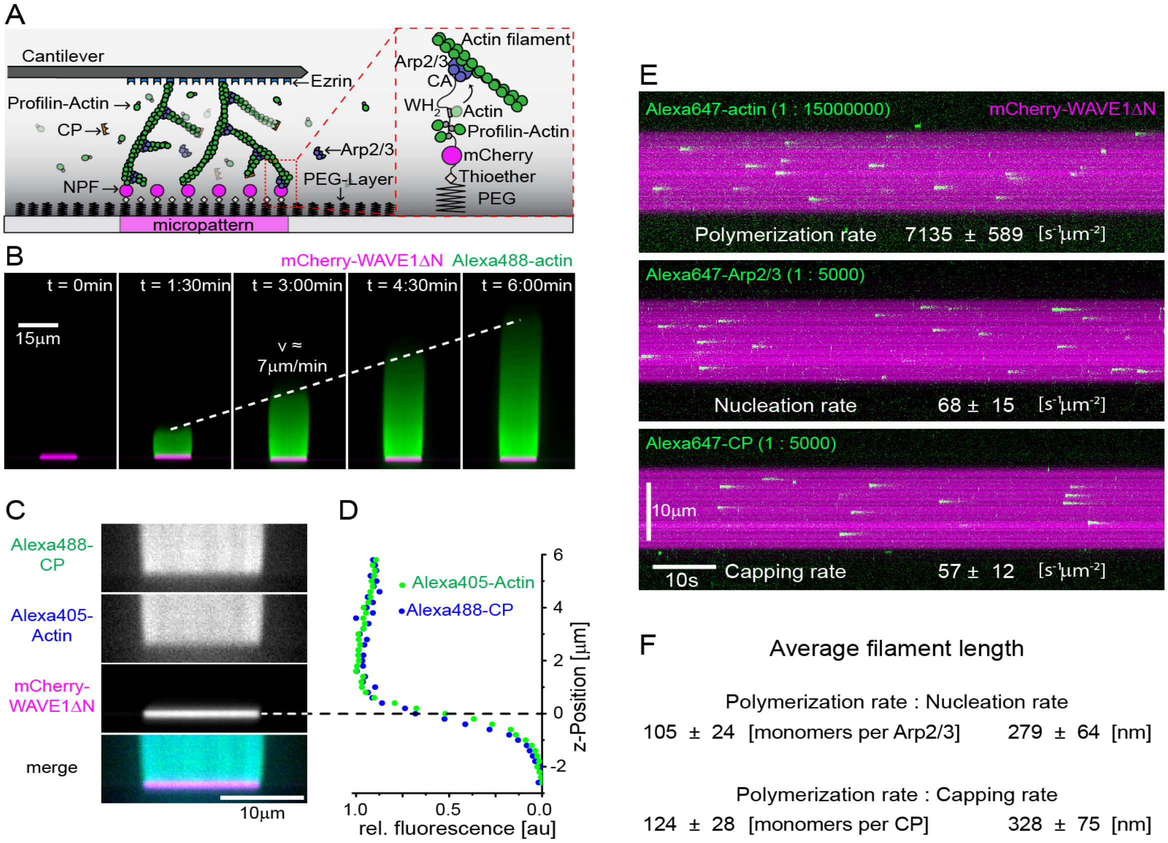

Figure 1. Reconstitution of branched network with in-vivo-like properties from micropatterned surfaces

(A) Scheme: NPF patches, bound to a PEG passivated coverslip, rapidly assemble branched networks from profilin-actin, CP and Arp2/3. Networks are visualized by fluorescence microscopy and mechanically manipulated through an AFM cantilever.

(B) Confocal microscopy (reconstructed axial view) of actin assembly (Alexa488-actin, green) from WAVE1DN micropatterns (magenta) after indicated time of protein addition (5 μM actin [1% Alexa 488-labeled], 5 μM profilin, 100 nM Arp2/3, 100 nM CP).

(C) Reconstructed axial view for indicated branched network components from confocal imaging. Conditions as in (B) with 15% TMR-CP and 5% Alexa647-Arp2/3.

(D) Intensity profiles of actin (blue) and CP (green) along axial dimension from confocal microscopy. Surface position (z = 0) was defined by the maximal mCherry-WAVE1 fluorescence signal (dashed line).

(E) Space-time plots (kymographs) from single molecule TIRF imaging of either actin (top), Arp2/3 (middle), or CP (bottom) incorporation into branched networks at a small reference stress of 25 pN/μm^2. Rates were determined by the product of the incorporation rate and the known labeling ratio.

(F) Average filament lengths as determined by the ratio of the single-molecule polymerization and the nucleation (top) or the capping (bottom) rate. All error indicators are SEM.

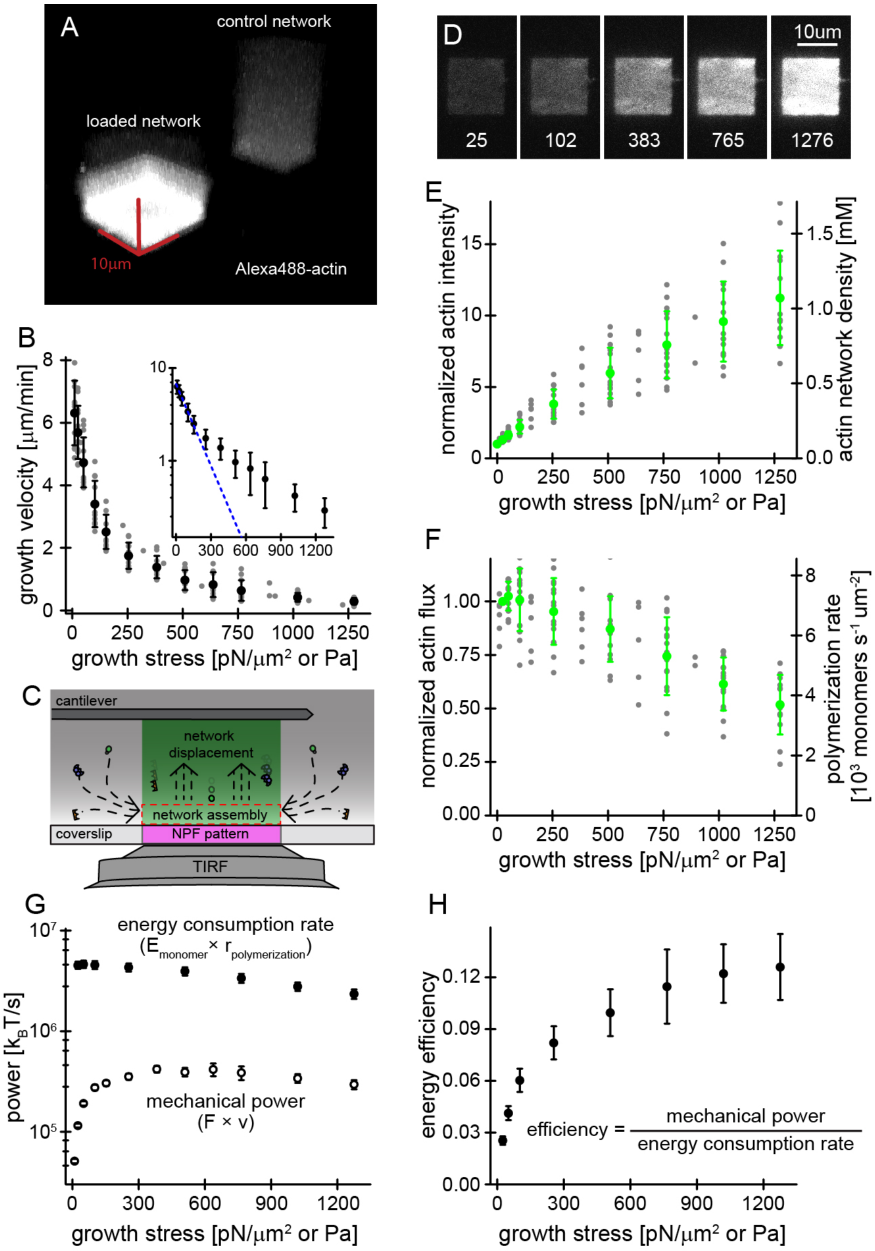

Figure 2. Force-feedback increases density and mechanical efficiency of branched actin networks

(A) Three-dimensional reconstruction from confocal microscopy of two networks growing under an AFM cantilever (left) or freely into solution (right).

(B) Steady-state growth velocities of networks as a function of growth stress. Grey, raw data; black, averages. Inset: semi-logarithmic replot together with a single exponential fit (dashed blue line) to the low-force data. Error bares are SD. (C) Scheme of network assembly visualized by TIRFM.

(D) TIRFM images of networks (Alexa488-actin) at indicated growth stress.

(E) Actin intensity (left y axis, normalized to unloaded control) and the calculated actin density (right y axis, calibrated by single molecule experiments (Figure 1E) as a function of growth stress. Grey, raw data; green, averages. Error bars are SD.

(F) Actin flux (left y axis, product of network density, and growth velocity, normalized to flux at 25 pN/µm^2) and polymerization rates (right y axis, calibrated by single molecule experiments) as a function of growth stress. Grey, raw data; green, averages. Error bars are SD.

(G) Semi-logarithmic plot of energy consumption rate (product of polymerization rate ($r_{polymerization}$, Figure 2F) and free energy change per monomer ($E_{monomer} = 3.18\ k_BT$) and mechanical power (calculated by the product of velocity [v] and force [F], see Figure 2E) as a function of growth stress. Error bars are SEM.

(H) Mean energy efficiency (determined by the ratio of the mechanical power and the energy consumption rate, see Figure 2G) as a function of growth stress. Error bars are SEM.

We used TIRF microscopy to quantify the rate at which individual molecules of actin, CP, and Arp2/3 join the growing network at the NPF-coated surface. We reduced the fraction of labeled actin to 1 in 1.5 x 10^6 molecules, which enabled us to visualize incorporation of individual actin monomers into the network. Each incorporation event was marked by the sudden appearance of a fluorescent spot within an NPF square (Figure 1E, top panel) that subsequently decayed exponentially with time as the molecule moved with the growing network out of the evanescent excitation field (Figures 1E and S1D). We counted single-molecule binding events and then divided their frequency by the actin labeling ratio to compute a total polymerization rate of 7,135 actin monomers-$s^{-1}\mu m^{-2}$ under our experimental conditions. Using this single-molecule approach, we also determined the total rates of nucleation/branching (68 Arp2/3-$s^{-1}\mu m^{-2}$) and capping (57 CP-$s^{-1}\mu m^{-2}$; Figure 1E, middle and bottom). The similarity of these rates indicates that most growing filament ends generated by NPF-stimulated Arp2/3 activity at the coverslip surface are also capped near this surface, within the shallow TIRF illumination field. We calculated the average filament length in two ways: by the ratio of polymerization rate to the rate of nucleation or capping (Figure 1F) and found that our filaments grew to a mean length of 300 nm (or 110 monomers), similar to filament lengths observed in branched networks in vivo (Vinzenz et al., 2012). We conclude that our reconstituted system captures the basic architecture and assembly dynamics of cellular actin networks.

Effect of load on branched actin network velocity, density, and efficiency

To measure network growth and to apply compressive forces, we positioned an AFM cantilever over an NPF-coated square before initiating network assembly (Figure 2A). To apply constant force to a growing network, we used optical feedback to maintain constant deflection of the AFM cantilever. We divide the cantilever force by the cross-sectional area of the actin network (200 μm^2) and report our measurements as force per unit area or stress (pN/μm^2 or equivalently, Pa). We first applied a stepwise series of increasing load forces to a growing network and measured steady-state growth velocity after the network adapted to the new growth force (Figure S2). This steady-state growth velocity fell sharply under small loads (Figure 2B) but did not stall completely until the load exceeded 1,250 pN/μm^2, a value comparable to pushing and pulling stresses generated by crawling cells (Gardel et al., 2008; Prass et al., 2006). The new steady-state growth velocity did not depend on previous forces (Figure S3), indicating that instantaneous force alone determines network growth at steady state. Finally, the force velocity curve does not follow a simple exponential decay as expected for a fixed number of growing filaments by Elastic Brownian Ratchet models (Peskin et al., 1993). Instead, velocity falls sharply at low force but decreases more gradually at higher force (Figure 2B), suggesting a possible load-dependent effect on filament density. To determine the effect of force on filament density, we performed TIRFM of fluorescent actin incorporating into networks growing under load (Figure 2C). While growth velocity decreases with applied load, the density of actin filaments in the network increases strongly (Figures 2D, 2E, and S3). This increased filament density does not reflect elastic compression but rather stable, force-induced changes in the material (see next section). The fall in growth velocity and the rise in filament density nearly compensate each other, adding up to a surprisingly weak, load-dependent decrease in the rate of actin incorporation (flux) into the network (Figure 2F). Using our single molecule measurement of actin polymerization under low growth force (Figure 1E) as calibration, we calculated assembly rates and filament densities for networks grown under other loading conditions (right y axes, Figures 2F and 2E). Over the functional force range—from zero load to network stall—filament concentration in the network increases from 0.125 mM to 1 mM (filament volume fractions of 0.5%–3.7%). From basic thermodynamics (Hill and Kirschner, 1982), we estimated the free energy change of one actin monomer adding to the barbed end of a filament under our experimental conditions. Multiplying this value by the actin flux yields the rate of energy consumption by the network as it pushes against various loads (Figure 2G). We used the force-velocity relationship of our branched networks (Figure 2B) to calculate the mechanical power output (product of force and growth velocity) at each force (Figure 2G). The ratio of the power output to the energy consumption rate yields the efficiency of the branched actin network as a motor (Figure 2H). This efficiency turns out to be highly load-dependent, increasing from ~3% at low force to ~14% at high force. Thus, polymerizing filaments appear to share their burden more evenly under high load, with fewer futile polymerization events occurring away from the network/load boundary.

Architecture and assembly kinetics of branched networks adapt to load

We find that force increases filament density in branched actin networks, but does this reflect (1) more polymerizing filaments, (2) a shift in network microstructure to denser packing, or (3) both (Figure 3A)? To determine whether load increases the number of polymerizing filaments, we developed an ‘‘arrestand-label’’ method to visualize free filament ends in the network (Figure S4). Briefly, we assembled two branched networks sideby-side: one unloaded and one growing against defined load. We then arrested network assembly by adding Phalloidin and Latrunculin B, together with a fluorescent derivative of CP (Figure 3B). The two small-molecules rapidly freeze actin dynamics (Akin and Mullins, 2008), while the fluorescent CP labels free barbed ends of filaments in the network (Figures 3B and S4). Accumulation of labeled CP was biphasic (Figures S4D and S4E), with rapid binding to free barbed ends followed by a very slow exchange of labeled CP with unlabeled CP throughout the network (Reymann et al., 2011; Schafer et al., 1996). In addition to TIRFM, we used three-dimensional stochastic optical reconstruction microscopy (3D-STORM) (Huang et al., 2008) to count free barbed ends in the network. The use of 3D-STORM enabled us to rule out potential TIRF artifacts, such as compression of free ends into the evanescent field (Figure S5). Both TIRF and 3D-STORM imaging of fluorescent CP after growth arrest showed that the number of free barbed ends in the branched network increases strongly (3.3-fold) with force (Figure 3C). To estimate the absolute number of free barbed ends, we combined these data with single-molecule measurements of actin incorporation. Based on the growth velocity of our networks under low force (7.33 μm/min, Figure S1), we estimate one free barbed end grows by 46 monomers per second, which implies the existence of 160 growing filament ends/μm^2 under low force. This number increases to 550/μm^2 at high load forces near stall. If growing barbed ends share this load equally, then each polymerizing filament generates 1.9 pN of force under high loads. This greater number of growing filaments only partly accounts for the observed increase in filament density under load (Figure 3D), suggesting that micro-structural changes also occur in the network. Since force causes changes in filament number and geometry we looked for other force-induced effects on network architecture, including changes in filament length. As above, we calculated average filament length in two ways, from the ratio of fluorescent Arp2/3 complex (on pointed ends) and CP (on barbed ends) to polymeric actin in the network (Figure 3F), which we calibrated with our single-molecule measurements of CP, Arp2/3 complex, and actin incorporating into networks under low force (Figures 1E and 1F). Remarkably, these measurements reveal that the mean filament length in a branched actin network remains constant from low loads that have little effect on network growth up to high loads that almost cause them to stall (Figure 3F). These results suggest that robustness of network stoichiometry under load reflects a close match between the force responses of filament elongation and capping.

Mechanics of branched actin networks depends on the force experienced during growth

How do load-induced changes in network architecture affect the ability of branched networks to transmit and resist forces? To address this question, we used AFM-based micro-rheometry to probe the material properties of branched actin networks grown under various loads (Figure 4A). We assembled networks under a constant growth force and arrested their assembly at a height of 10 μm with Latrunculin B. The slow dissociation of CP (Schafer et al., 1996) and the Arp2/3 complex (Beltzner and Pollard, 2008) from branched filaments ensured that networks remain essentially constant during the time required to measure their material properties (Figure S6A; Experimental Procedures). After assembly under load and kinetic arrest, we performed AFM micro-rheometry on networks at a small, constant force (12.5–25 pN/μm^2). Under these ‘‘relaxed’’ conditions we measured elasticity in the range of 10^3 –10^4 Pa, consistent with previous measurements on branched networks (Chaudhuri et al., 2007; Marcy et al., 2004; Pujol et al., 2012) (Figure 4B). Both the elastic (Figure 4B) and viscous moduli (Figure S6C) increased with increasing growth force, a change that corresponded to increased filament density. Interestingly, when we removed the growth force immediately following arrest, the height of the network increased only slightly (<10%, Figure 4C), regardless of the magnitude of the force. This minimal height change shows that force-dependent increases in actin density are stored in the microarchitecture of the network and are not the result of elastic compression.

Branched actin networks are maximally elastic and minimally viscous under loads that match their original growth force

Many biological polymer networks assembled in the absence of force exhibit strong stiffening when subjected to subsequent loads or ‘‘pre-stress’’ (Gardel et al., 2006; Janmey et al., 1991; Storm et al., 2005). To investigate the mechanical response of branched networks, we performed rheology measurements on growth-arrested actin networks assembled at various growth forces and subsequently pre-stressed with a range of ‘‘test loads’’ (Figures 4D and S7). We find that branched actin networks are stiffest when the test load matches the original growth force experienced during its assembly. When tested at loads above or below the original growth force, the material either becomes softer or remains the same (Figure 4E). Sparse networks assembled at low growth forces exhibit little softening at lower test loads, while denser networks assembled under high growth forces soften more significantly (4-fold) (Figure 4E).

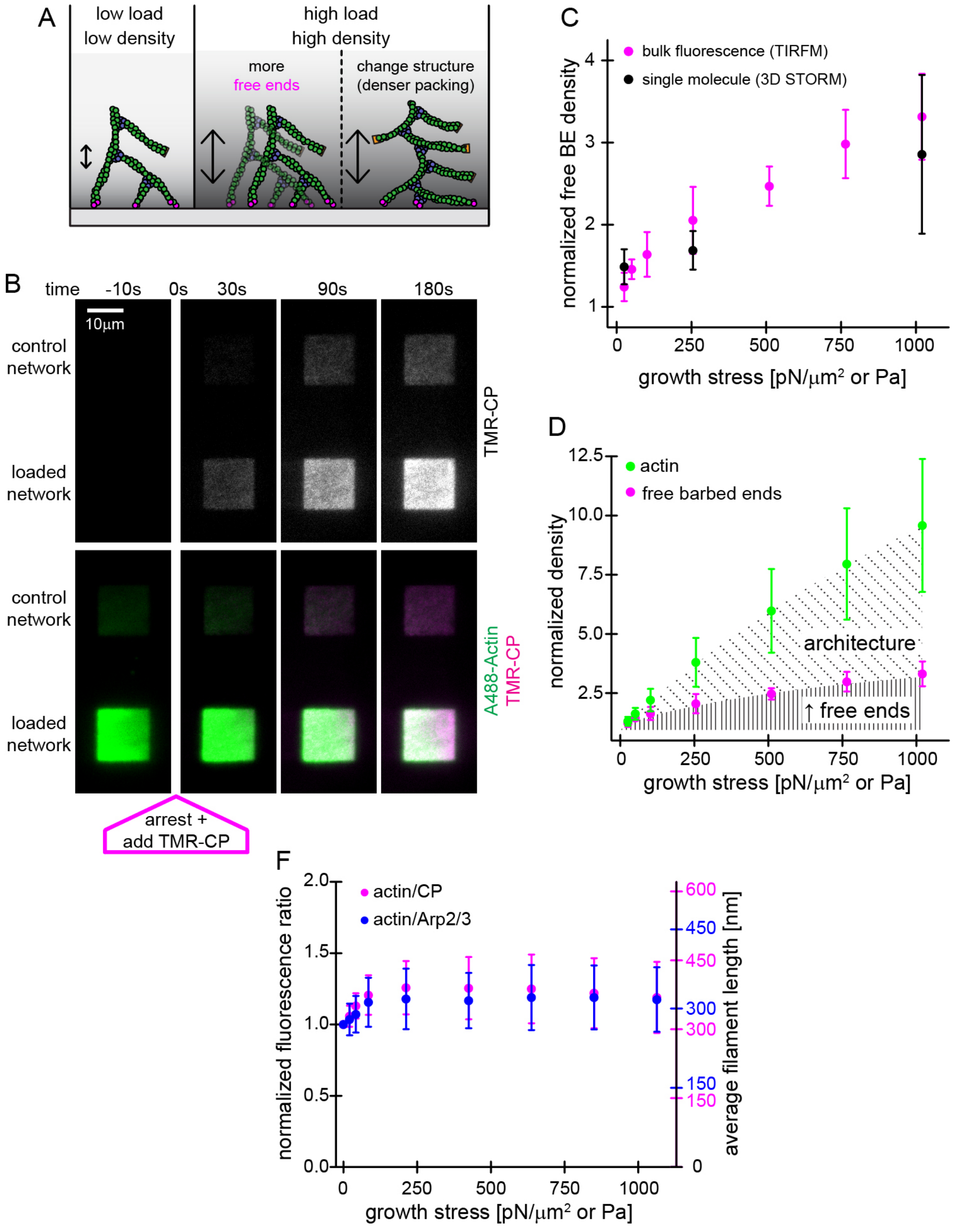

Figure 3. Force-feedback increases the density of free barbed ends within the network but does not alter the stoichiometry of its constituents

(A) Scheme of network assembly under low (left) or high stress (middle and right). Density increase by either rise in the number of free ends (middle) and/or changes in packing of filaments (right).

(B) TIRFM images of TMR-CP binding (top alone[greyscale] or as color merge with Alexa488-actin [green and magenta, bottom]) to networks either unloaded or assembled under 1,020 pN/μm^2 load at indicated times after kinetic arrest (t = 0 is the addition of labeling mix [27.5 μM Latrunculin B, 27.5 μM phalloidin, 18.5 nM TMR-CP]).

(C) Free barbed end densities (normalized to unloaded control) from either TIRFM (magenta) or 3D STORM (black) as a function of growth stress.

(D) Free barbed end (magenta) or actin (green) densities normalized to unloaded control as a function of growth stress. The increased free end density (vertical, solid lines) accounts for a fraction of actin density rise and the residual rise is due to denser filament packing (diagonal, dotted lines).

(E) Ratio of fluorescence intensities (left y axis, normalized to unloaded control) or average filament lengths (right y axis, calibrated by single molecule assays, Figure 1F) of actin/CP (magenta) or actin/Arp2/3 (blue) as a function of growth stress. Error bars are SD.

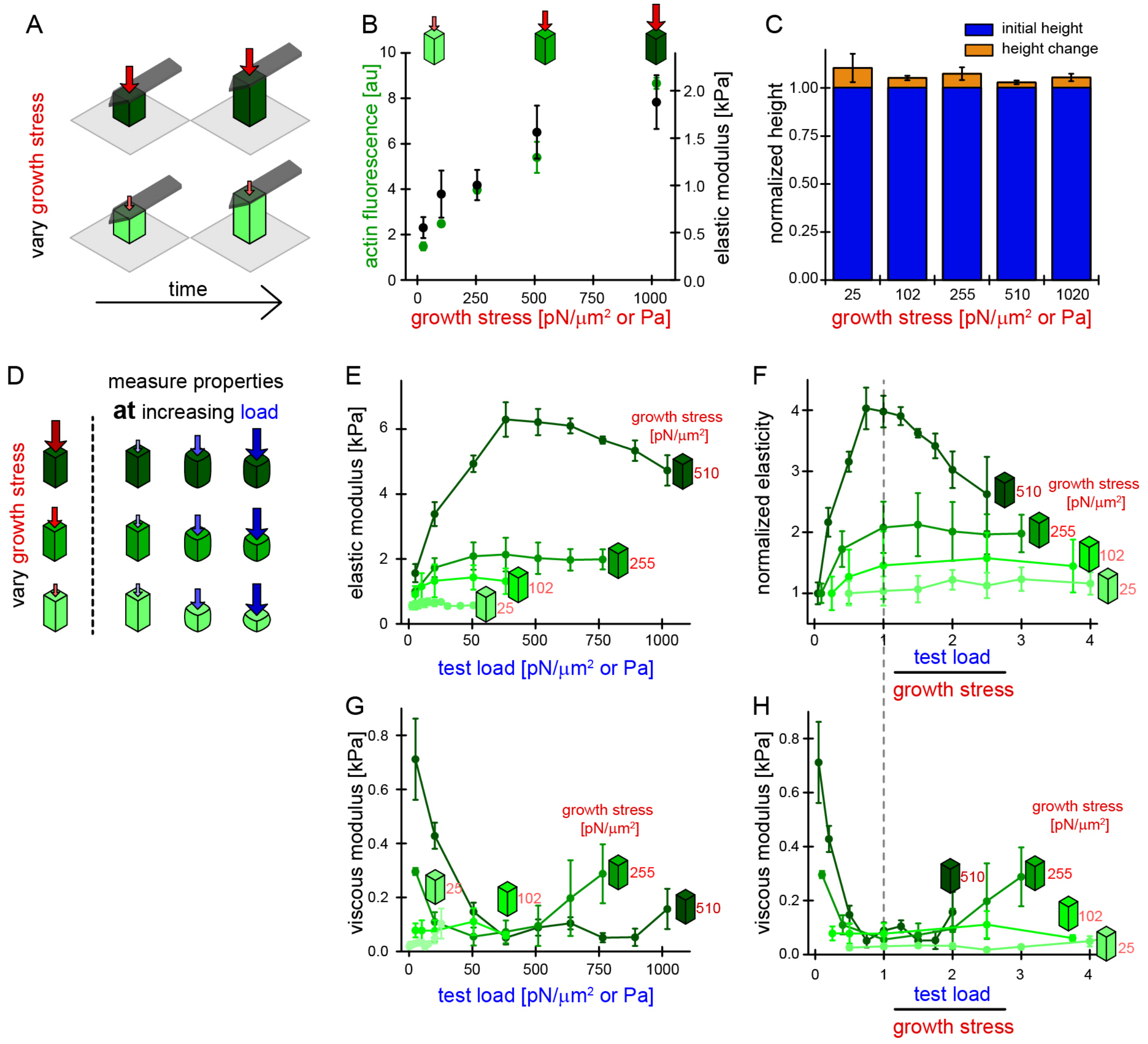

Figure 4. Adaptation to load- and growth-forces shapes the material properties of networks

(A) Scheme of network assembly under high (dark red arrow, top) or low (light red arrow, bottom) growth stress, resulting in high (dark green) or low (light green) network density.

(B) Actin fluorescence from TIRFM imaging (green, left y axis) and initial elasticity from micro-rheology (black, right y axis) as a function of growth stress. Measurements were performed at low test load (12.5–25 pN/μm^2) following network arrest. Error bars are SD.

(C) Change in network height (orange) after growth stress release to low levels (12.5–25 pN/μm^2) following arrest for networks assembled at different growth stresses as indicated. Height was normalized to the initial network height at the moment of growth arrest (blue). Error bars are SD.

(D) Scheme: networks are assembled under growth stresses (red arrows, left), arrested (dashed line) and then subjected to increasing test load (blue arrows, right). Elasticity is measured at each test load.

(E) Network elasticity as a function of test load for networks assembled at different growth stresses as indicated.

(F) Same as (E) with elasticity normalized to the initial elasticity and the test load normalized to the growth stress.

(G) Network viscosity as a function of test load for networks assembled under different growth stresses as indicated.

(H) Same as (G) but with the test load normalized to the growth stress. See also Figures S6 and S7. D-H: Error bars are one half SD

Similarly, when loaded beyond the growth force, the stiffness of sparse networks remained relatively constant, while dense networks softened. To better compare the behavior of branched networks assembled at different growth forces, we normalized the applied test load by the original growth force. We also normalized the elasticity measured under high test-loads by the initial elasticity of the ‘‘relaxed’’ material. The normalized data illustrate that maximum stiffness occurs when the test load equals the growth force (Figure 4F). Interestingly, the viscous modulus of branched actin networks falls to a minimum when the test load equals the growth force, and increases at lower and higher test loads (Figures 4G and 4H). These data reveal that growing branched actin networks adapt to a specific growth force to become maximally stiff and minimally viscous at that load.

Loading branched networks beyond their growth force results in mechanical failure

We next measured recovery of the height of self-assembled actin networks following release of a test load (Figure 5A). Purely elastic materials recover 100% of their original height after force release, but we found that branched actin networks show loaddependent, irreversible height loss following high loads (Figure 5B). Such irreversible plastic deformation is analogous to crushing of a material such as Styrofoam and usually reflects permanent micro-structural changes in the material. Networks assembled under high growth forces are stiffer and more resilient to deformation compared to networks grown under low load. Normalizing the test load by the growth force causes all of our deformation data to collapse onto a single curve (Figure 5C) and reveals that the growth force also defines a critical point beyond which the material irreversibly changes. Structural failure was also evident when we measured network elasticity. When subjected to test loads below the growth force, network stiffness recovered to nearly its original value upon test load release. Once loading exceeded the growth force, however, the network failed to recover its original elasticity (Figures 5D and 5E). Such irreversible changes could affect the growth rate and elastic properties of branched actin networks exposed to varying physical boundary conditions.

Time-varying forces create inhomogeneous actin networks with composite properties

In vivo actin networks experience changing forces in a complex and heterogeneous environment. Applying such time-varying forces to growing actin networks yields inhomogeneous materials, with layers of different filament density. To study such inhomogeneous materials we assembled branched networks under changing growth forces, arrested their assembly, and measured their elasticity under varying test loads. To create two-layered networks, we first assembled a dense network under 500 pN/μm^2 (Figure 5F, left). At a height of 4 μm, we reduced the load to 25 pN/μm^2 (Figure 5F, right) and assembled an additional 6 μm of sparser network. We compared the mechanics of this bi-layered material to homogeneous networks assembled under high or low force alone (Figure 5G). If the bi-layered network was purely elastic its stiffness would be dominated by the weaker material (Figure 5G, dashed magenta line). Instead, as the test load approached the higher growth force, we observed stiffening in the inhomogeneous material that was intermediate between those of the high- and low-density materials (Figure 5G, middle green line). This result is explained entirely by plastic deformation of the low-density layer when test load exceeds its growth force (Figure 5G, solid magenta line). Once the weaker layer is crushed, the properties of the composite shift toward those of the denser material. In this way, mechanical failure may enable inhomogeneous actin networks to adapt more quickly to high load forces.

Anisotropic, branched actin networks behave differently than isotropic, crosslinked networks

The stiffness of random, isotropic actin networks (both crosslinked or entangled) scales roughly as the square of filament density (Figure 6A) (Gardel et al., 2003). We wondered whether the same characteristic power-law scaling of stiffness with density describes anisotropic, branched actin networks assembled under load. Comparing our results with published data, we find that branched networks generated by localized activity of the Arp2/3 complex are much denser and stiffer than isotropic actin networks (Figure 6A). Their elastic modulus, however, scales much more weakly with filament density ($\sim c_A^{0.6}$, where c_A is the concentration of filamentous actin). Previous studies have also suggested that stress-induced stiffening of isotropic actin networks follows a ‘‘universal’’ power law, in which the elastic modulus increases as the ~1.5 power of the ‘‘pre-stress.’’ We find that, while branched actin networks exhibit stress-stiffening, this behavior does not match that of isotropic networks and does not follow a single power law across all network densities. Moreover, we observe branched network stiffening at forces more than an order of magnitude beyond the point of isotropic network failure (Figure 6B). The physics of branched actin networks, therefore, appears to be distinct from that of random gels.

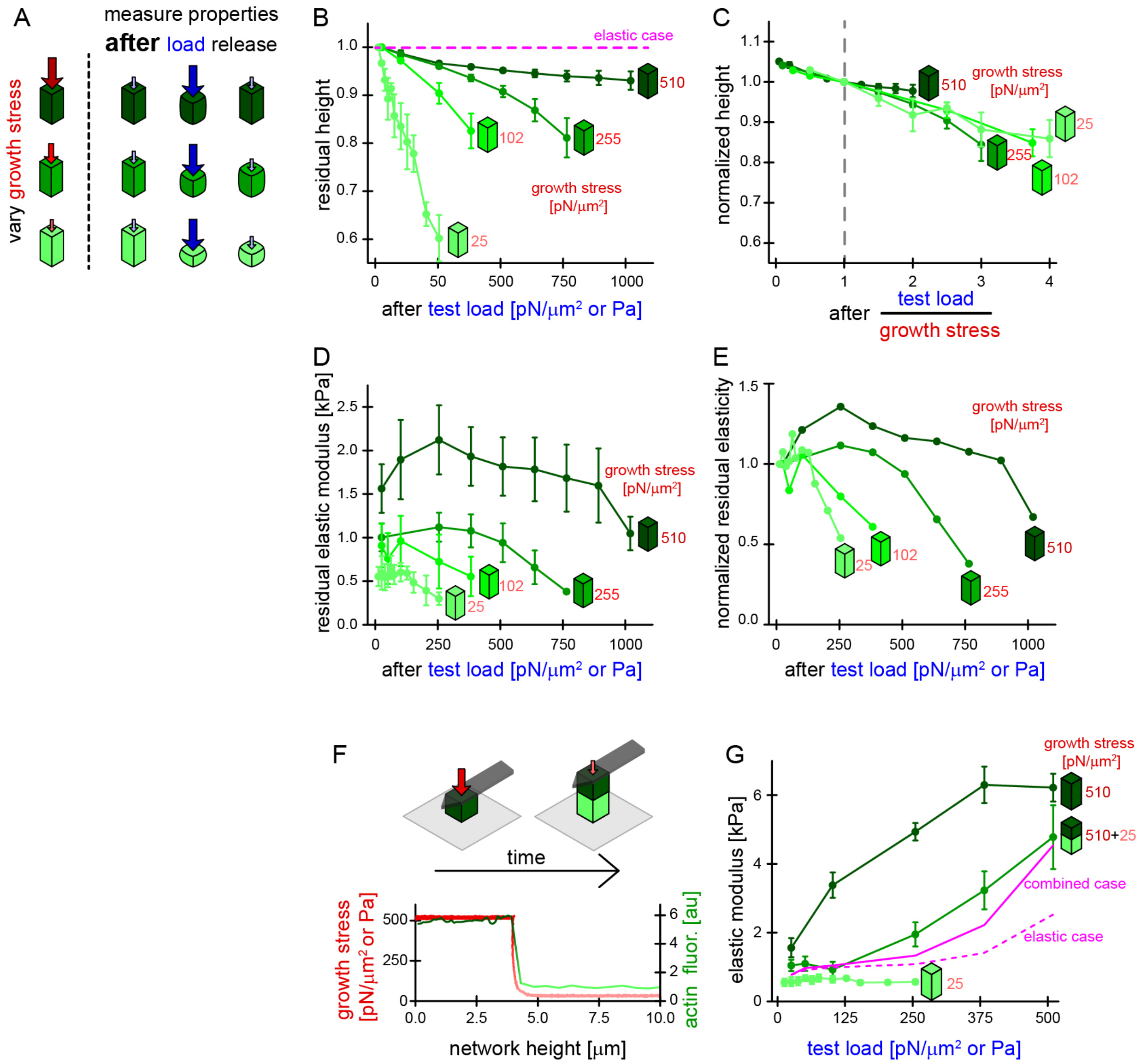

Figure 5. Loading beyond the growth force causes mechanical failure leading to history-dependent mechanical properties

(A) Networks are assembled at different growth stresses (red arrow, left) resulting in different network densities (green), arrested (dashed line) and initial height and elasticity are measured under low test load. Networks are then subjected to stress cycles consisting of high test load followed by a low test load, recovery step during which the residual height and elasticity is determined (blue arrows, right).

(B) Residual network height (normalized to the initial height) measured during the recovery step as a function of the previously applied high test load for networks assembled under different growth stress. The dashed magenta line is the ideal elastic case (full recovery).

(C) Same as (B) but with the test load normalized to the growth stress. Residual network height was normalized to the residual height after the test load reached the growth stress.

(D) Residual network elasticity measured during the recovery step as a function of the previously applied high test load for networks assembled under different growth stresses.

(E) Same as (D) but with the residual elasticity normalized to the initial elasticity.

(F) Top: composite network assembly. Networks are first assembled at a high growth stress, i.e., at high actin density (left). Upon reaching a defined height, growth stress is reduced giving rise to a sparse network layer (right). Bottom: growth stress (red, left y axis) and actin fluorescence (green, right y axis) of a discontinuous, two-layered network as a function of network height.

(G) Network elasticity as a function of test load for either homogenous networks assembled at constant growth stress (510 or 25 pN/μm^2) or a composite network assembled at 510 and 25 pN/μm^2 as indicated. Dashed magenta line is the estimated network elasticity for the composite network assuming purely elastic behavior. The continuous magenta line is an estimate that additionally includes mechanical failure (plastic deformation). All error bars are one-half SD.

Filament crosslinking proteins stiffen branched actin networks but do not shift the critical force that defines their material properties

Actin filament crosslinkers filamin-A and a-actinin are thought to strengthen some branched actin networks in vivo (Flanagan et al., 2001; Vinzenz et al., 2012). We investigated the effect of these crosslinkers by growing branched actin networks under constant force, terminating their growth with latrunculin B, and then adding either filamin-A or a-actinin. By visualizing labeled crosslinkers with confocal microscopy, we determined the affinities of filamin-A and a-actinin for branched actin networks to be K_D = 0.37 μM and 2.12 μM, respectively (Figure 6C), in agreement with previous studies (Nakamura et al., 2007; Wachsstock et al., 1993). Both crosslinkers stiffened branched networks (Figure 6D), but we observed interesting differences between them (Figure 6D). Dense actin networks assembled under high forces stiffened more when crosslinked by a-actinin than by filamin-A, while sparse networks assembled under low load showed the opposite behavior (Figure 6D, inset). Neither crosslinker qualitatively changed the shape of the stress-stiffening curve, indicating that the mechanical response of branched actin networks is dominated by their load-adaptive architecture rather than by properties of the crosslinker. Interestingly, filamin-A and a-actinin also produced different effects on plastic deformation of branched actin networks loaded above their growth force. Both crosslinkers protected sparse networks from plastic deformation, but a-actinin provided less protection than filamin-A (Figure 6E). Conversely, both crosslinkers increased plastic deformation of denser networks, probably by “locking in” filament contacts induced by compression. Under these conditions, a-actinin enhanced deformation more than filamin-A (Figure 6F).

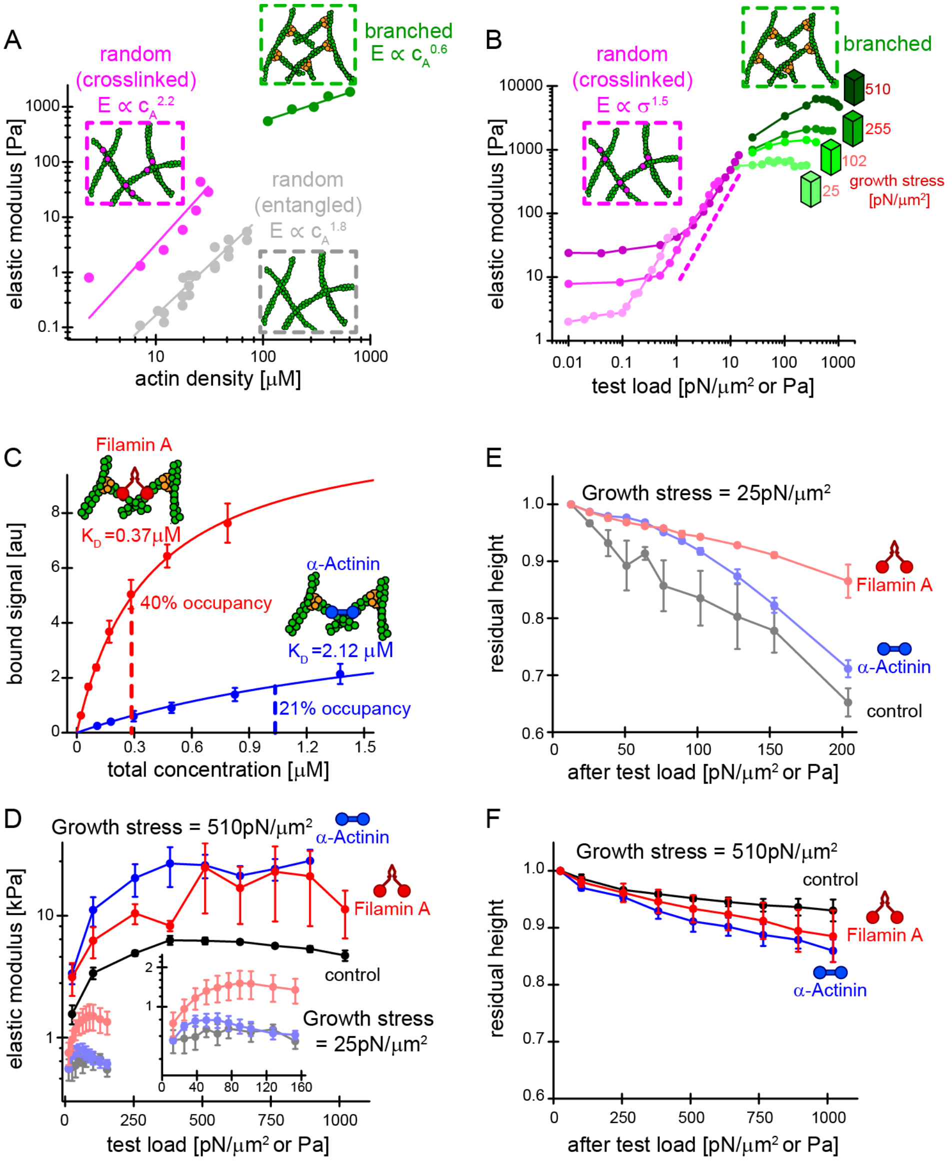

Figure 6. Branched network mechanics are distinct from random gels and not fundamentally changed by crosslinkers

(A) Elasticity of entangled (light gray, from Gardel et al., 2003) or crosslinked random gels (dark gray, from Gardel et al [2004a], 0.03 actin:scruin ratio) compared to branched networks (green) as a function of actin density. Lines are power laws with indicated scaling factors

(B) Double-logarithmic plot of network elasticity as a function of test load (prestress) for either random cross-linked networks of different actin concentration (magenta, from dark to light = 29.4, 21.4,8.33 μM, 0.03 actin:scruin ratio, from Gardel et al. [2004b]) or branched networks assembled at indicated growth stress (green). The dashed magenta line indicates the ‘‘universal’’ scaling behavior of random actin gels.

(C) Fluorescence of network-bound filamin-A (red) or a-actinin (blue) by confocal microscopy as a function of total concentration. Lines are fits to single-site binding models. Dashed lines indicate concentrations used for mechanical measurements resulting in a fractional occupancy of binding sites as indicated.

(D) Network elasticity as a function of test load for networks assembled at a growth stress of 25 (light) or 510 pN/μm^2 (dark) growth stress and additionally crosslinked with either filamin-A (red) or a-actinin (blue) or a buffer control (black).

(E) Residual network height (normalized to initial network height) for networks assembled at low (25 pN/μm^2) growth stress, crosslinked with filamin-A (red), a-actinin (blue) or a buffer control (black) as a function of the previously applied test load. Height was measured during the recovery step.

(F) Same as (E) but for networks assembled at high (510 pN/μm^2) growth stress. All error bars are one half SD.

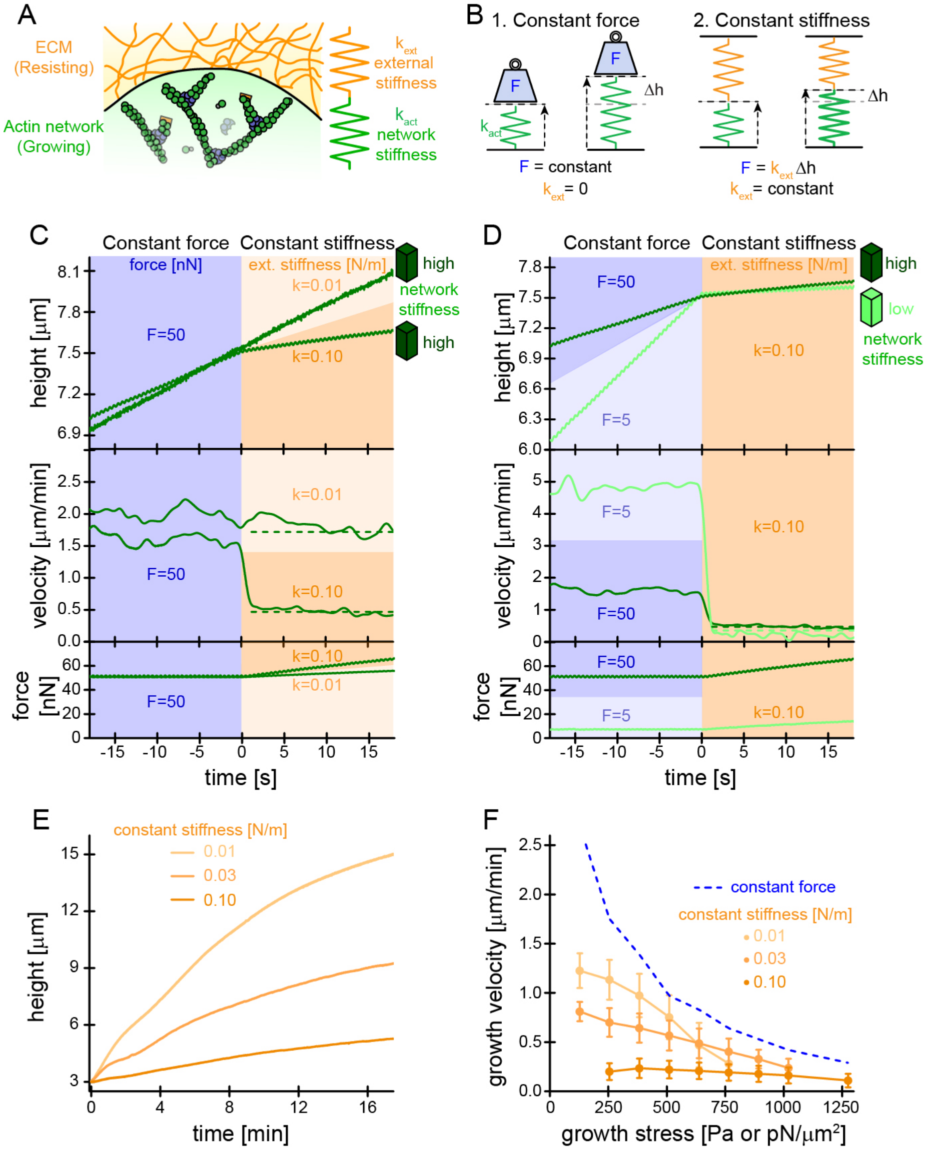

Figure 7. Branched network motor activity depends on the mechanical environment

(A) Scheme of branched actin networks (green) pushing against the ECM (orange) at the leading edge.

(B) Scheme of a network pushing against an AFM cantilever. The AFM can operate either keeping the force constant (zero external stiffness, left) or the external stiffness constant (defined force at a given cantilever deflection, right).

(C) Sample height (top), normalized growth velocity (middle), and force (bottom) for two networks assembled under constant high (50 nN) growth force (blue area), resulting in high (darkgreen traces) network stiffness. At t = 0, force feedback is disengaged and networks displace cantilevers imposing either high (k = 0.1 N/m, dark orange area) or low (k = 0.01 N/m, light orange area) external stiffness. The drop in velocity can be predicted (dashed lines) from the known network stiffness.

(D) Same as (C) for two networks grown under constant high (50 nN, dark blue area) or low (5 nN, light blue area) growth force (light blue area), resulting in high (dark green trace) and low (light green trace) network stiffness, respectively. After disengaging the force-feedback, networks are challenged with the same external cantilever stiffness (k = 0.1 N/m, dark orange area).

(E) Sample height as a function of time for networks pushing against cantilevers of different stiffness. Networks were grown in the absence of force to a height of 3 μm before cantilever contact (t = 0).

(F) Network growth velocity as a function of growth force under either constant force (blue dashed line, see Figure 2E) or constant stiffness conditions (orange) for three different external (cantilever) stiffness as indicated. Error bars are SD.

Motor activity of branched actin networks depends on loading history

What happens when a growing actin network pushes against a material with a defined stiffness rather than against a constant force? The extracellular matrix, for example, can offer defined mechanical resistance to actin-driven pseudopod extension (Figure 7A). A network growing against a barrier of defined stiffness does not feel constant force, but a steadily increasing force that depends on how far the barrier is displaced. We, therefore, compared the velocities of branched actin networks grown against AFM cantilevers whose deflection was controlled in two different ways. In one experiment, we applied a constant force (as before) by moving the cantilever base along with the growing network maintaining constant cantilever deflection (Figure 7B, left). Under these conditions, force on the network does not depend on network height. In the second experiment, the cantilever base remains stationary and deflection increases as the network grows (Figure 7B, right). In this mode, the cantilever mimics a Hookean spring or an elastic material with a constant stiffness. The more the cantilever is deflected, the more force it exerts. To investigate how network growth responds to changing mechanical constraints we performed two-step experiments. First, we assembled two networks under the same constant force. We then switched the two networks to grow against two boundaries of different constant stiffness. Interestingly, velocity of the network pushing against the stiffer barrier fell instantly even though force on the network increased gradually and by a small amount over the short time (<15 s) of this experiment (Figure 7C). Next, we assembled two networks under two different constant forces, one high and one low. We then switched both networks to grow against the same constant stiffness barrier. In this case, the velocity of the sparse network grown under low force immediately drops below that of the denser network, even though (1) the sparse network's velocity was initially much greater, and (2) the force the sparse network experiences during the second part of the experiment is much less than that experienced by the denser network (Figure 7D). This result can be explained by how the free energy of actin filament assembly partitions between cantilever deflection and deformation of the network. In constant stiffness mode, the network and cantilever act as two springs in series. When the cantilever mode switches from constant force to constant stiffness, the force immediately rises above the critical force of the network (the original growth force) and, therefore, actin assembly begins to both deflect the cantilever and to crush older parts of the network. This partitioning immediately reduces the growth velocity. To test our understanding of this energy partitioning within the network, we used several known parameters—network elasticity (Figure 4E), growth velocity under constant force (Figures 7C and 7D), and cantilever spring constant, to calculate the growth velocity expected at the moment of switching from constant force to constant stiffness. These calculated values agree well with measured velocities (dashed lines in Figures 7C and 7D) demonstrating how the instantaneous (but not the steady-state) growth velocity of branched actin networks depends on loading history. This complex dependence manifests in the different height changes of branched networks growing under constant stiffness barriers (Figure 7E) and in the force-velocity relationships calculated from them (Figure 7F). The steady-state velocities measured under constant force define the upper bound on growth rates at all forces (Figure 7F, blue dashed line). In contrast, the steadily increasing forces experienced during growth against an elastic barrier create a time-varying loading history and produce not one but a family of force-velocity relationships that define the ‘‘motor activity’’ of branched actin networks.

Discussion:

The present study demonstrates that force plays a major role in defining the architecture, mechanics, and function of branched actin networks. Specifically, we identified an intrinsic force-feedback mechanism by which load forces experienced during self-assembly increase filament density and make growing networks stiffer and more resistant to mechanical failure. Importantly, the change in mechanical properties associated with increased filament density does not obey scaling relationships that describe isotropic crosslinked or entangled actin gels.

Average filament length is invariant under load

Elongation of actin filaments slows dramatically under load, but this slowing has no effect on the average length of filaments in a self-assembling branched network. The reason is that filament capping responds to force in the same way as filament elongation. Individual filaments grow slower under load, but because capping is also slower, they grow for a proportionally longer time, reaching the same length. The force-invariance of filament length has important consequences for the material properties of branched actin networks. If, for example, filament length decreased with applied force, the overall coherence of the network would decrease due to loss of entanglement between branched filament arbors. Conversely, a force-induced increase in average filament length would produce filaments that buckle more easily under lower forces. Either response would nudge the material properties of the network toward a regime that is less capable of resisting the applied load.

Force alters internal architecture of branched actin networks

Over the range from zero load to forces that stall network growth, the filament density of a branched actin network increases by about an order of magnitude. A force-dependent increase in the number of free barbed ends (T.-D.L., P.B., D.M., and D.F., unpublished data) accounts for part of this increase in density (~3.5-fold), while the remainder (~3-fold) must reflect changes in filament packing. This is most easily visualized in terms of the angle between the filaments and the boundary surface they push against. In the absence of strong forces opposing growth, filaments in branched actin networks in vivo (Svitkina and Borisy, 1999; Weichsel et al., 2012), in vitro (Cameron et al., 2001), and in silico (Maly and Borisy, 2001; Schaus et al., 2007) are distributed symmetrically around an average angle of ~54° with respect to the membrane. This angle of attack is determined primarily by the geometry of ~72° y-branches made by the Arp2/3 complex. A 3-fold increase in filament density could be produced by a 3-fold decrease in the sine of the average angle of attack: from ~54° to ~16°. This shallower angle of attack could be produced by bending filaments or branch-points or by increasing the out-of-plane rotation of y-branches with respect to the membrane.

Branched actin networks exhibit unique material properties distinct from those of isotropic actin gels

The elastic modulus of branched actin networks scales more weakly with density ($\sim c_A^{0.6}$) compared to isotropic gels ($\sim c_A^2$) and their response to test load (“pre-stress”) does not follow a “universal” scaling law. The stress-stiffening of isotropic actin networks has shown to be dominated by the entropy of individual filaments under tension (MacKintosh et al., 1995). Our data, however, indicate that the mechanics of anisotropic, branched actin networks assembled under load are determined by different microscopic processes. Instead of the entropic elasticity of long filaments, the higher stiffness and weaker dependence on density might reflect direct bending of short, stiff filaments constrained by the branched network architecture. Higher order phenomena, such as the interlocking of meso-scale arbors of branched filaments, may also contribute under these conditions. New theoretical approaches to actin mechanics will help resolve these questions.

Crosslinkers have different effects on branched actin network material properties

Differences in affinity and in network micro-architecture likely explain the differential effects of a-actinin and filamin A on sparse and dense branched actin networks. Filamin-A is a v-shape crosslinker that prefers actin filaments that cross orthogonally. a-Actinin, on the other hand, is a rod-shaped, anti-parallel dimer that can drive formation of gels or bundles. Under low load forces, we suggest that the crossing angle between filaments from adjoining arbors will be ~72°, an angle determined by the geometry of Arp2/3-dependent branching and that favors binding of filamin A. As the geometry of the network changes under load filaments from adjacent arbors intersect at higher angles, approaching 180° (anti-parallel), a configuration that disfavors filamin A but not a-actinin. This might explain why, at low growth forces the incorporation of a-actinin has a modest effect compared to filamin-A, while at high growth forces the effect of a-actinin becomes more significant.

Motor activity of branched actin networks depends on loading history

Mechanical failure of actin networks may be an important element of their adaptation to mechanical loading. When the load on a growing network increases, newly formed material will be denser and stronger than older layers, which are crushed by the higher load forces. Plastic deformation of weaker layers reduces their contribution to the composite stiffness of the material and transiently reduces network expansion. Understanding the combined effects of force on assembly and mechanical collapse is essential to understanding how branched actin networks push against their cellular loads. Force-mediated coupling between filament assembly and material properties represents a key difference between the motor activity of branched networks and motor proteins such as myosin or kinesin. Under a given set of biochemical conditions, the activity of a motor protein is defined by a single force-velocity curve (Carter and Cross, 2005), whereas the motor activity of branched networks exhibits a spectrum of force-velocity relationships that depend on both the instantaneous internal stiffness of the network and the external stiffness of the material against which it pushes.

Methods:

Four main techniques are utilized in this paper: (1) reconstitution of branched networks from purified proteins (actin, profilin, Arp2/3, CP, and NPF), (2) biochemical surface micro-patterning of NPFs on coverslips, (3) atomic force microscopy to control the mechanical loading and to measure the material properties of the network, and (4) fluorescence microscopy (confocal, TIRF, and 3D STORM) of protein assembly in the network at bulk and single molecule levels. After immersing the NPF patterned surface (technique 1) in assembly mix (5 mM actin, 5 mM profilin, 100 nM Arp2/3, 100 nM CP), branched networks grew (technique 2) under loads imposed by the AFM (technique 3) and molecular assembly was observed by fluorescence microscopy (technique 4). This experimental approach allowed us to quantify the effects of force on branched network growth. We simultaneously measured mechanical properties and fluorescence intensities of branched actin networks that were grown under biochemically and mechanically defined conditions.

Surface micro-patterning

We coated the coverslip with a high density of diamino-polyethylene glycol (PEG), which was derivatized with maleimide. We then photo-eliminated maleimide groups in selected regions of the coverslip by UV irradiation through a photo mask, leaving square regions (14 x 14 μm^2 if not indicated otherwise) of intact maleimide. Unlike previous approaches (Reymann et al., 2010), our patterning method does not remove PEG molecules from the coverslip and therefore leaves the surface passivated. We reacted the intact maleimide regions with a WAVE1 mutant (WAVE1DN), which replaced the N-terminal SH1 domain by mCherry and contained a single reactive cysteine residue at its N terminus. This immobilizes the NPF in an oriented and mechanically stable manner.

Atomic force microscopy

To tightly couple the cantilevers to the network, we designed a custom cantilever holder to reduce the angle of the cantilever on glass substrate surface and coated cantilevers with a peptide from the filament-binding protein Ezrin. With these modifications, we never observed slippage between the cantilever and the network and, under loading conditions used in this study, we never observed the entire network macroscopically bend or buckle under the cantilever.

Acknowledgements

We thank Scott Hansen for reagents, discussions, and comments on the manuscript; Thomas Surrey, Michael Vahey, and Marcus Taylor for comments on the manuscript; and members of the D.A.F. and R.D.M. labs for discussions. This work was supported by NIH R01 GM074751 (D.A.F.), NIH R01 GM061010 (R.D.M.), HHMI (R.D.M.), HFSP LT-000843/2010 (P.B.), and EMBO ALTF 854-2009 (P.B.). T.-D.L. was supported by the Taiwan National Science Council. This project was an equal collaboration between the laboratories of D.A.F. and R.D.M. The order in which the corresponding authors are listed was determined by flipping a coin.

Supplemental Figures:

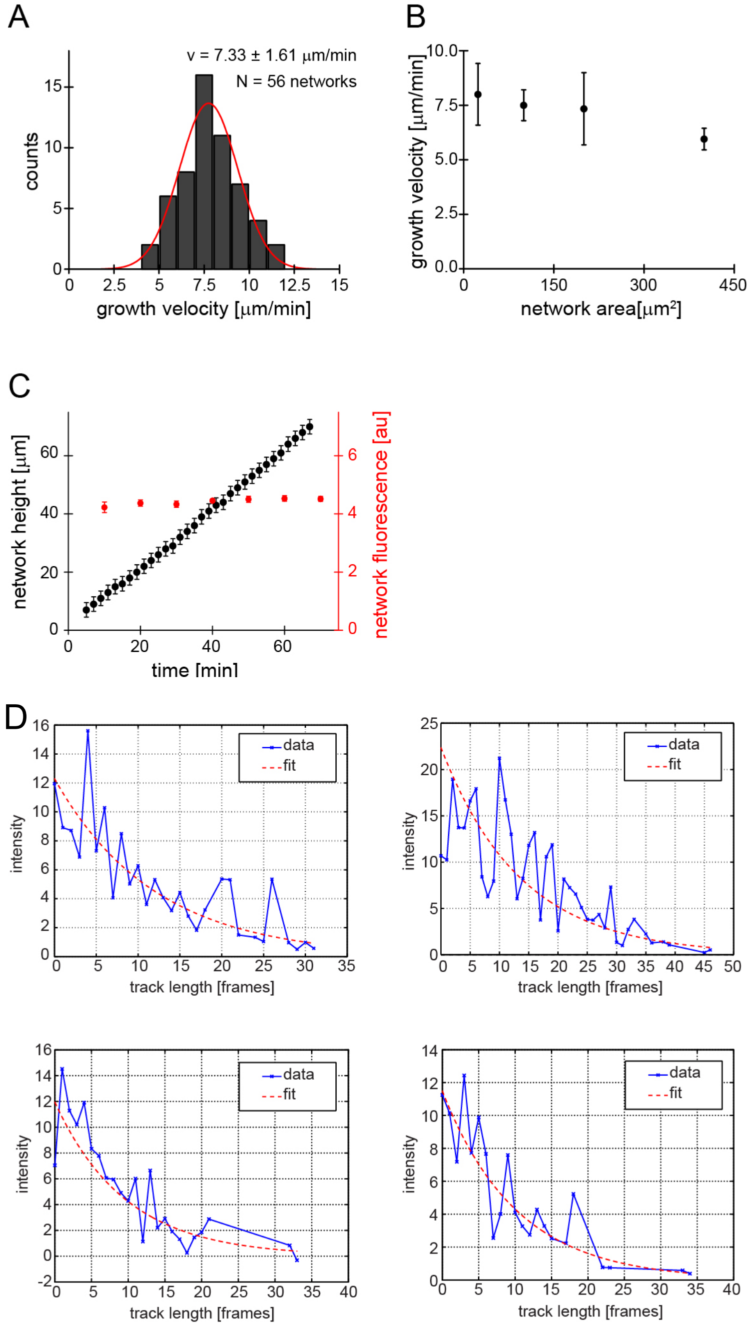

Figure S1. Branched network assembly in the absence of force, related to Figure 1

(A) Distribution of network growth velocities in the absence of load as determined by confocal microscopy for 56 networks from 12 independent experiments. The red line is a fit to a Gaussian function.

(B) Mean network growth velocity as a function of network area. Each point contains data from at least 10 networks for 2 independent experiments.

(C) Network height and actin network fluorescence as a function of time for networks grown at reduced profilin-actin concentrations (1.5 μM each). Data are from 6 networks. Error bars are SD.

(D) Representative intensity traces (blue) for individual Alexa647-labeled actin molecules incorporated into a growing branched network loaded with 25pN/μm^2 stress. The red dashed lines are fits to an exponential decay function $I(t) = I_0 e^{-kt}$ with I_0 = intensity at t = 0 and k = decay constant

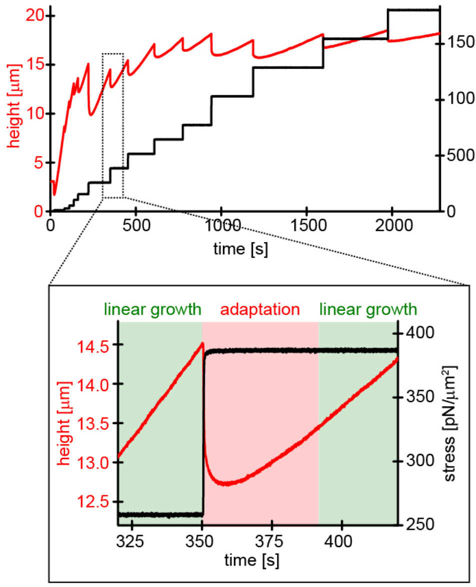

Figure S2. Branched network growth by atomic force microscopy, related to Figure 2 Height (red) and stress (black) as a function of time for a representative growing network. The stress was kept constant at a defined setpoint via the feedback mechanism of the AFM(“force-clamp mode”) until the height change over time appeared linear (inset, green area). The stress was then raised to a higher setpoint, to which the network responded by an adaptation phase (inset, red area) which was followed by a linear phase after reaching equilibrium. Network growth velocities and densities of components as a function of growth stress were determined from the linear, steady-state phases.

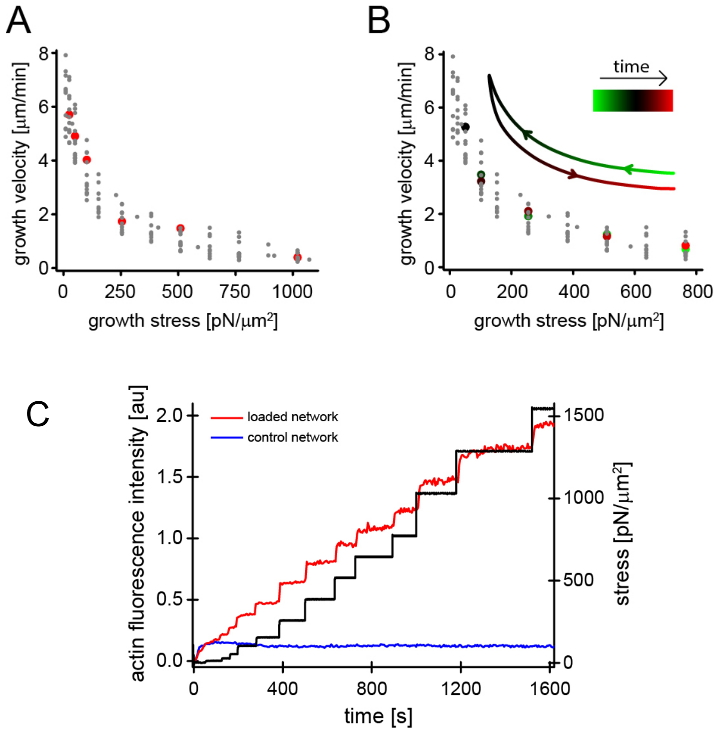

Figure S3. Network growth velocity is not dependent on loading-history, but actin polymer density increases in response to load, related to Figure 2
(A) Force dependence of growth velocity determined for networks grown under either a single, constant stress (red) or incrementally increasing growth stresses as mostly used throughout the manuscript (gray). Both methods yield similar growth velocities.
(B) Hysteresis test. Networks are subjected to a stress cycle, going from high to low load first (green symbols) and then back (red symbols). Note that growth velocities from the descending and ascending phase are very similar to each other and to velocities measured for steadily and gradually increasing stresses (gray).
(C) Actin fluorescence for a network (red) loaded at indicated stress (black) and an adjacent, unloaded control (blue) as a function of time.

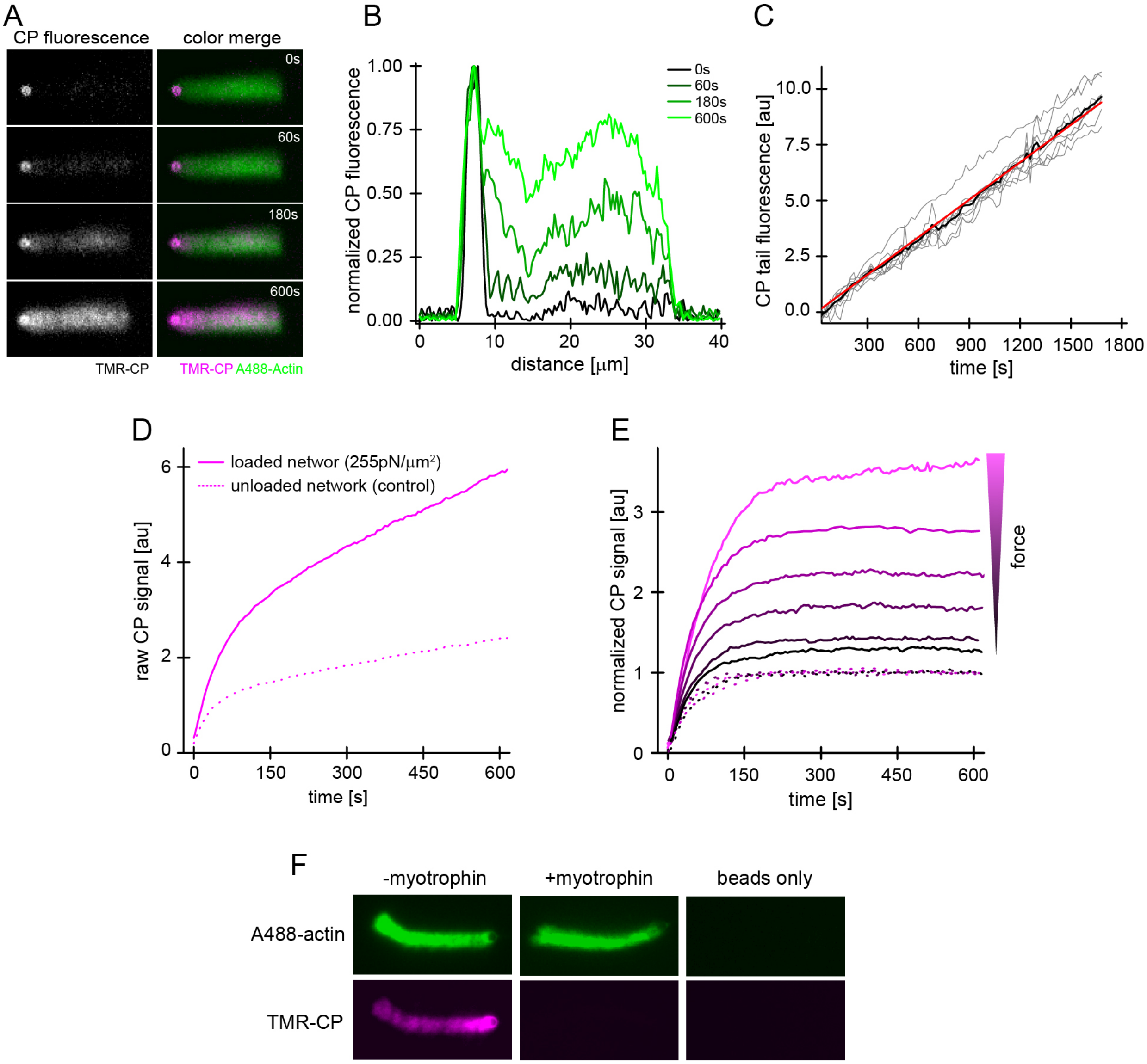

Figure S4. An ''Arrest and Label'' assay for the quantification of free barbed ends, related to Figure 3
(A) Images from time-lapse widefield fluorescence microscopy of comet-tail networks assembled from NPF-coated polystyrene beads at indicated times after kinetic arrest with LatrunculinB, phallodin and TMR-labeled CP. t = 0 is the start of time-lapse imaging which was about 30-60 s after biochemical arrest. Note the rapid appearance of a bead-proximal CP signal followed by the gradual accumulation of CP throughout the rest of the actin network. We interpret the first, rapid signal as capping of existing free barbed ends in the proximity to the NPF, whereas the gradual accumulation represents turnover.
(B) Normalized TMR CP fluorescence from line-scans across the comet tail along the axis of growth (front to rear = left to right) at indicated time after the beginning of imaging. Bead-proximal free ends are capped rapidly, whereas accumulation of labeled CP in the tail is gradual and slow.
(C) Kinetics of CP turnover in the comet tail for 10 individual networks (gray lines). The black line is the averaged signal and the red line is a linear fit. Note that turnover kinetics are slow and can be assumed to be linear over times < 1500s.

(D) Raw TMR-CP signal for branched networks grown from NPF-micropatterns either at 510pN/μm^2 stress (continuous line) or in the absence of load (dashed line) as a function of time after kinetic arrest. The signal was fitted to a sum of an exponential and a linear function (with the exponential phase representing capping of existing free ends and the linear phase representing turnover of capped ends). Subtraction of the turnover signal and normalization the unloaded internal control yields the normalized barbed end signal.

(E) The barbed end signal as a function of time for representative networks loaded with increasing load (25, 102, 255, 510, 765 and 1020pN/μm^2, continuous lines) normalized to the internal, unloaded control network (dotted lines).

(F) TMR-CP fluorescence (magenta) accumulated in actin comet tails (green) 45 min after kinetic arrest in the presence (middle panels) or absence (left panels) of myotrophin (a strong competitive CP inhibitor). The right panels represent a negative control for NPF-coated beads without an actin network. Note that CP does not localize to the NPF beads alone and that CP binding to the actin network is potently inhibited by myotrophin.

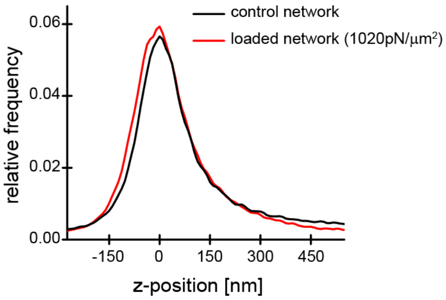

Figure S5. Axial localization of free ends by STORM, related to Figure 3
Relative frequency of barbed end localization as a function of z-position for either a representative network loaded with 1020pN/μm^2 (red) or an unloaded control (black). The position is set to z = 0 at the maximal relative frequency.

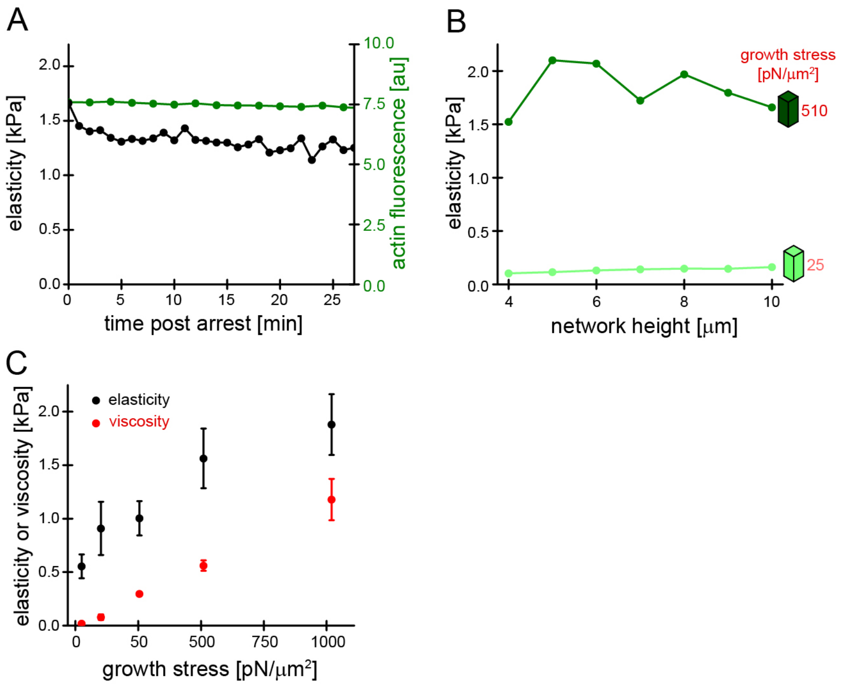

Figure S6. Branched networks are stable after kinetic arrest, related to Figure 4
(A) Network elasticity and actin fluorescence as a function of time after kinetic arrest by addition of LatrunculinB.
(B) Network elasticity during the assembly phase at 25 pN/μm^2 (light green) or 510 pN/μm^2 (dark green) as a function of sample height, showing that elasticity is nearly constant with network height. Elasticity measurements below 4um sample height were not reliable, because of the hydrodynamic influence of the proximal coverslip surface on the AFM cantilever.
(C) Initital elastic (black) and viscous modulus (red) from microrheology as a function of growth stress. Measurements were performed at low test load (12.5-25 pN/μm^2) following the arrest of network assembly.

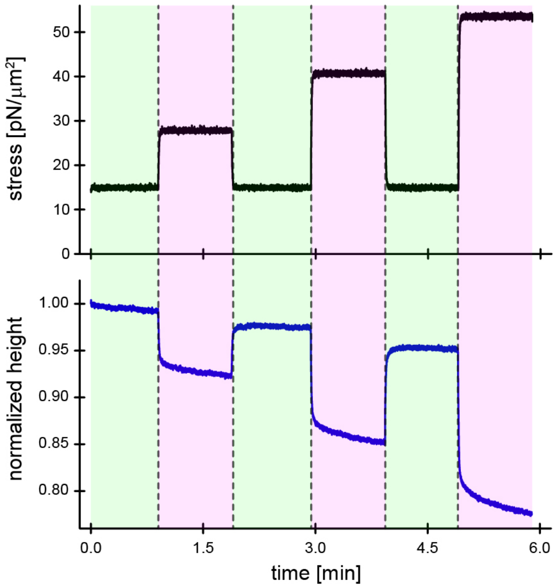

Figure S7. Application of test load cycles to branched networks, related to Figure 4
Representative force and height traces for branched networks subjected to test load cycles. Applied test load (black, upper panel) and resulting normalized network height (blue, lower panel) for a network assembled under 25 pN/μm^2 growth stress. Test loads are applied in form of alternating steps of increasing stress (magenta area) intermitted with recovery steps at a constant low test load (green area).

Supplemental Methods:

1. Protein biochemistry:

1.1 Coverslip-immobilized proteins (NPFs and mCherry variants): The coding sequence of Human WAVE1 lacking the N-terminal SH1 domain (AA 171-559, WAVE1ΔN) was codon-optimized for expression in E. Coli (GeneArt) and fused to an N-terminal mCherry-tag harboring an N-terminal LysCys-Lys-(KCK-)tag (for surface immobilization) followed by a His10-tag (for purification) and cloned into a modified pET vector containing a TEV-cleavable z-tag. To prevent surface attachment via protein sites other than the N-terminal KCK-tag, endogenous Cysteine residues of WAVE1 (Cys 296 and 407) were replaced with Serine without affecting protein activity. A non-fluorescent version of this mCherryNPF fusion construct was generated by introducing a Tyr71->Ser mutation in mCherry (darkCherry) to facilitate multicolor TIRF microscopy when direct visualization of the NPF was not necessary. For the purification of mCherry or dark mCherry lacking NPF activity, we introduced a STOP codon between the Cherry and NPF moiety. Proteins were expressed in E.Coli (Star pRARE) for 16h at 18°C and purified by IMAC over a HiTrap Chelatin column, followed overnight TEV cleavage on ice, ion-exchange chromatography over a Source Q (XK 16-20) column and gelfiltration over a HiLoad Superdex 200 column. Proteins were SNAP-frozen in liquid nitrogen in storage buffer (20mM HEPES (pH=7.5), 150mM NaCl, 0.5mM TCEP, 0.1mM EDTA, 20% Glycerol).

1.2 Actin: Native, cytoplasmic actin from Amoeba castellanii was purified by ion-exchange chromatography and a cycle of polymerization-depolymerization as described previously (Hansen et al., 2013) and stored in filamentous form dialyzing against polymerization buffer (20mM Imidazole (pH=7.0), 50mM KCl, 1.5mM $MgCl_2$, 1mM EGTA, 0.5mM ATP, 0.5mM TCEP). 5ml fractions of the filamentous pool were depolymerized at a time by dialyzing into G-Buffer (2mM Tris-Cl (pH=8.0), 0.1mM $CaCl_2$, 0.2mM ATP, 0.5mM TCEP) for 1 week, followed by gelfiltration over a HiLoad Superdex 200 (XK16-60) column. Actin was kept in monomeric form after gelfiltration at 4C for up to two months. Actin was fluorescently labeled with Alexa488-Maleimide at Cys 374 as previously described (Hansen et al., 2013). For labeling actin with Alexa405- or Atto540Q-NHS, the profilin-actin complex was formed in G-Buffer with a 1.5-fold excess of profilin. The complex was isolated by gelfitration over a Superdex 75 column in labeling buffer (2mM HEPES (pH=8.0), 0.1mM $CaCl_2$, 0.2mM ATP, 0.5mM TCEP), concentrated and labeled at reactive lysine residues by incubating with a 10-fold excess of the NHS-dye for 1h on ice. After quenching with Tris-Cl (2mM, pH=8.0), actin was polymerized by addition of 10x polymerization buffer and a small quantity (1% of total actin) of freshly sheared filaments. After polymerization for 1h at room temperature, filaments were pelleted by ultracentrifugation (20 min at 80 krpm in a TLA100.2 rotor) and then depolymerized in G-Buffer for 1 week in the dark. Depolymerized, labeled actin was then gelfiltered over a Superdex 75 column and stored on ice.

1.3 Arp2/3 complex: The native, bovine Arp2/3 complex was purified from calf thymus glands (PelFreez) by a series of ammonium sulfate precipitation and ion-exchange chromatography (DEAE, Source Q and Source S) steps followed by gelfiltration

(Superdex 200) as described previously (Doolittle et al., 2013). Arp2/3 was fluorescently labeled by addition of 3-fold excess of maleide-dye conjugate, incubated for 1.5h on ice, quenched by adding DTT to 1mM and desalted into VCA Buffer A (5mM TrisCl (pH=8.0), 5mM NaCl, 1mM DTT, 0.2mM $MgCl_2$, 0.1mM ATP). To remove a small subfraction of Arp2/3, which irreversibly bound to the NPF after labeling, the complex was bound to a 5ml NPF affinity column (N-WASP VCA immobilized on a HiTrapNHS resin) and eluted by a 10CV gradient to VCA Buffer B (5mM Tris-Cl (pH=8.0), 5mM NaCl, 0.2mM $MgCl_2$, 0.1mM TCEP, 0.1mM ATP). Peak fractions were pooled, concentrated and gelfiltered over a Superose 6 column. Proteins were SNAPfrozen in liquid nitrogen in storage buffer (5mM HEPES (pH=7.5), 50mM NaCl, 0.5mM $MgCl_2$, 0.5mM TCEP, 0.5mM EGTA, 0.1mM ATP, 20% Glycerol).

1.4 Capping protein: To generate wt CP, the α1 and β2 isoforms of murine heterodimeric capping protein were cloned into pETM20 and pETM33, respectively. To generate fluorescently tagged, wt CP, an Nterminal SNAP-tag (Keppler et al., 2003) was fused to the beta subunit. Proteins were co-expressed in E.Coli (Rosetta) for 16h at 18C and purified by IMAC over a 5ml HiTrap Chelatin column followed by overnight TEV/Prescission cleavage of the N-terminal His-tags on ice. After desalting over a HiLoad Desalting column, uncleaved protein and free tags were removed by recirculation over the IMAC column. The flow through was subjected to ion-exchange chromatography over a Mono Q column and gelfiltration over a Superose 6 column. Proteins were SNAP-frozen in liquid nitrogen in storage buffer (10mM Tris-Cl (pH=7.5), 50mM NaCl, 0.5mM TCEP, 20% Glycerol). Addition of the N-terminal SNAP-tag did not affect capping activity in the absence of force as measured by polymerization of pyrene-actin in bulk or capping in single filament TIRFM assays.

1.5 Profilin: Human profilin 1 was expressed and purified as previously described (REF) and SNAPfrozen in liquid nitrogen in storage buffer (10mM Tris (pH=8.0), 50mM KCl, 1mM EDTA, 0.5mM TCEP, 20% Glycerol)

1.6 Ezrin-ABD: The C-terminus of human Ezrin (aa 553-586) followed by a 13aa Gly-rich linker and a C-terminal KCK-motif was cloned into pGEX-6P-2, expressed in E.Coli (Rosetta) for 8h at 25C, purified over a GST Trap column followed by overnight GST-Prescission cleavage on ice and desalting. Desalted protein was filtered over a GST Trap column to remove free GST and GST-Prescission. The flow through was gelfiltered over a Superdex 75 column and SNAP frozen in liquid nitrogen in in storage buffer (10mM Tris (pH=8.0), 150mM KCl, 0.5mM TCEP, 20% Glycerol)

1.7 Myotrophin/VI: Full length, human myotrophin was cloned into a modified pETM11 vector containing a TEV-cleavable, N-terminal His10-tag and expressed in expressed in E.Coli (Rosetta) for 8h at 25C, purified over a HiTrap Chelatin column followed by overnight TEV cleavage on ice and desalting. Desalted protein was filtered over a HiTrap Chelatin column to remove free His-tag and TEV. The flow through was gelfiltered over a Superdex 200 column and SNAP frozen in liquid nitrogen in in storage buffer (20mM HEPES (pH=7.5), 150mM KCl, 0.5mM TCEP, 20% Glycerol)

2. Surface functionalization and protein immobilization:

2.1 Coverslip functionalization, photolithography and protein immobilization: Glass coverslips (22x22 mm, #1.5, high precision, Zeiss) were functionalized and patterned as described previously (Fourniol et al., 2014). Briefly, surfaces were rigorously cleaned by consecutive incubation in 3M NaOH and Piranha solution (3:2 concentrated sulfuric acid to 30% hydrogen peroxide) followed by silanization with (3-Glycidyloxypropyl)trimethoxysilane. Silanized surfaces were then passivated by reacting with diamino-PEG. Subsequently, exposed amino groups were reacted with a heterobifunctional crosslinker (BMPS) to create PEG-maleimide coated coverslips, which were subjected to UV-microlithography using a chrome-on-quartz photomasks, which selectively protected maleimide groups within chrome-covered areas from UV exposure. Micropatterned PEG-maleimde coverslips were then loosely attached to flow chambers constructed of PLL-PEG passivated microscopy counter slides and thin PDMS stripes (flow cell volume=40μl). For the immobilization of NPF on micropatterned PEG-maleimide coverslips, protein aliquots of KCK-Cherry- WAVE1ΔN (NPF) and KCK-Cherry (mock protein) were rapidly thawed and und pre-reduced with 1mM beta-mercaptoethanol for 30min on ice and then desalted twice into Immobilization Buffer (20mM HEPES (pH=7.5), 300mM NaCl, 0.5mM EDTA). Protein concentration was determined by Au280nm and NPF protein mix was prepared by diluting desalted proteins to 10μM total in immobilization buffer, followed by direct incubation for 25min at room temperature with the freshly patterned PEG-maleimide coverslip in the flow cell contained in a humidified chamber. The NPF density was controlled by adjusting the relative percentage of KCK-darkCherry-WAVE1ΔN (NPF) and KCKdarkCherry (mock protein). Coverslips were prepared using a percentage of 60% NPF and 40% mock protein. For the FRET experiments determining the WH2 occupancy, coverslips were prepared using 50% KCK-darkCherry-WAVE1ΔN, 10% CLPTE-darkCherry-WAVE1ΔN (Alexa488-Cys490) and 40% KCK- darkCherry. After protein immobilization, flow cells were washed with 6 flow cell volumes wash buffer (20mM HEPES (pH=7.5), 300mM NaCl, 0.5mM EDTA, 5mM beta-mercaptoethanol), incubated for 3min to quench residual maleimide groups, washed with 6 flow cell volumes storage buffer (20mM HEPES (pH=7.5), 300mM NaCl, 0.5mM EDTA, 2mM TCEP) and stored at 4°C in a humid container for up to 5 days.

2.2 Cantilever functionalization: Tipless, uncoated cantilevers were chemically cleaned by incubating in Piranha solution (3:2 concentrated sulfuric acid to 30% hydrogen peroxide), washed, transferred to custom-built PDMS incubation chambers and functionalized by incubating for 1.5 h in Silane-PEG5000- Maleide (Nanocs, freshly resuspended to 2% (w/w) in 95% ethanol, 5% water, pH=5.0) at room temperature. The cantilevers were then washed twice in excess ethanol, dried for 1h at 75°C and washed with ultrapure water. Ezrin-ABD was diluted to 20μM in cantilever buffer (2mM Tris-Cl, pH=8.0) and immobilized on PEG-Maleimide-functionalized cantilevers by overnight incubation at 4C in custom-built PDMS incubation chambers. Immediately before the experiment, Ezrin-coated cantilevers were washed in excess cantilever buffers and dried.

3. Fluorescence and atomic force microscopy systems:

3.1 TIRFM-AFM system: Imaging was performed on an Observer.Z1 (Zeiss) microscope equipped with a total internal reflection fluorescence (TIRF) slider (Zeiss), a TIRF objective (PlanApochromat 100X 1.46 TIRFM, Zeiss) and a cooled charge-coupled device camera (iXon888, Andor). Fluorescence excitation was accomplished by three diode-pumped solid-state laser lines (488, 561 and 644nm), which were controlled using an acousto-optical filter and coupled into a single fiberoptic light guide (custom laser launch, Spectral Applied Research). Micro-Manager (Edelstein et al., 2010) was used to control the shutters, acousto-optical filter, dichroic mirrors and camera. Laser intensity and exposure was minimized to avoid photo-bleaching. For bulk multi-color fluorescence measurements of branched network component densities, images (300ms exposure time) were taken at custom intervals of increasing time (5-30s to avoid bleaching in networks growing with reduced velocity at elevated forces). Fast, one-color imaging of single molecules was performed at an increased frame rate of 10 frames/s and a 100 ms exposure time (‘‘streaming’’ mode).

Force measurements were performed using commercial AFM system (BioScope Catalyst, Bruker) which was extensively modified to a) have larger force range, b) lower the angle between the NPF-coated coverslip and the cantilever, c) prevent evaporation of aqueous solution, and d) perform micro-rheology measurements as described in detail below:

a) To increase the dynamic force range of our AFM system, we replaced the commercial AFM photodiode detector with a position sensitive detector (PSD) (Pacific Silicon Sensor, DL100-7PCBA3), which has a larger sensor area (10x10 mm^2) to detect larger bending of the soft AFM cantilever. We also aligned the AFM laser close to the base of cantilever to have larger optical lever sensitivity (OLS) to gain larger cantilever bending within the detectable range of the PSD. To reduce high frequency noise, the deflection and sum signal from the PSD were processed by a low-pass filter (Krohn-Hite, 3364) with 30 Hz cut-off frequency. Custom software written in LabView (National Instruments) was used for data acquisition, force feedback, and cantilever z-position control.

b) The typical contact angle of our commercial AFM (15 degree) was too large for our experiments since it resulted in slippage of actin network on cantilever surface when applying large forces and also exerted non-uniform stress on the actin network. We therefore constructed a custom-build cantilever holder with a very low contact angle of about 3.5 degree. The conventional spring-clamp mechanism for AFM cantilever mounting on the holder is not suitable for this low-angle design. To fix AFM cantilever on the holder, we used paraffin wax (Sigma-Aldrich, 327212) as biocompatible adhesive to mount the AFM cantilever onto the low angle cantilever holder.

c) We constructed a custom sample holder that was mounted on the microscope stage to visualize branched networks through an inverted TIRFM microscope from the bottom and perform AFM measurements from the top. Because of the open AFM configuration leading to evaporation, we overlaid the reaction mix (150µl) with 80ul mineral oil containing a surfactant (20 mg/ml Cithrol DPHS, Croda Health Care, USA) to passivate the liquid-oil interface.

d) For AFM-based microrheology measurements (Alcaraz et al., 2003; Mahaffy et al., 2000) we applied a sinusoidal wave with frequency of 2Hz and amplitude of 20 nm to the z-piezo which vertically drives the AFM cantilever. When the oscillating cantilever was in contact with the network, the cantilever normal deflection started to oscillate with the same frequency (2 Hz). The amplitude and phase shift of the oscillatory normal deflection were detected by a lock-in amplifier (7270, Signal Recovery) and used to determine the mechanical properties of the actin network.

3.2 Confocal-AFM system: Imaging was performed on an Observer.Z1 (Zeiss) microscope equipped with a confocal scanner (CSU-X1; Yokogawa Electric Corporation), a 63x objective (PlanApochromat 63X 1.4, Zeiss) and a cooled charge-coupled device camera (CascadeII, Photometrics). Fluorescence excitation by three diode-pumped solid-state laser lines (401, 488, 561 and 644nm), which were controlled using an acousto-optical filter and coupled into a single fiberoptic light guide (custom laser launch, Solamere Technology Group). Micro-Manager (Edelstein et al., 2010) was used to control the shutters, acousto-optical filter, dichroic mirrors and camera. Laser intensity and exposure was minimized to avoid photo-bleaching. Multicolor z-stacks (100ms exposure time at 0.2-1mM step sizes) were acquired at 1min time intervals. The custom AFM was constructed using a 850 nm laser (Blue Sky Research), a Position Sensitive Device (PSD, Pacific Silicon Sensor, DL100-7PCBA3), 3 piezo stages (Mad City Labs), a x-y motorized stage (Thorlabs), a manual vertical translational stage (Newport, MVN50), 3 manual translational stages (Thorlabs, MT1), a home-made cantilever holder, a home-made sample holder, and a home-made adaptor plate. The vertical linear stage was used to coarse control the AFM in z-direction. The laser, PSD, and home-made AFM cantilever holder were mounted on the vertical linear stage through 2 translational stages in x-y-, 1 translational stage in x-, and 1 piezo stage (NanoOP100, Mad City Labs) in z-direction respectively. The home-made sample holder was mounted on the adaptor plate through x-y piezo (Nano-OP100, Mad City Labs) and x-y motorized stages for fine and coarse sample navigation in x-y-direction. The bottom of the adaptor plate is designed to fit conventional microscopy stages. During measurements, the vertical linear stage, together with all the components on it, were mounted on the confocal microscope through a custom-built adaptor plate. All the AFM electronic signals from PSD were pre-processed by an electronic filter (Krohn-Hite, 3362) set to dc low-pass at 30 Hz. Custom-written software in LabView was used for signal processing, data acquisition, and piezo stage control.

3.3 3D STORM-AFM system: The AFM system used for the 3D STORM is the same home-built AFM which is described in section 3.2. Single-molecule imaging experiments were performed on a custombuilt microscope based on a Nikon Ti-U inverted microscope with an Olympus 100× UPlanSApo 1.4 N.A. objective and custom-built focus stabilization utilizing the reflection of an IR laser off the interface between the glass coverslip and sample. Four lasers (OBIS 405-50, OBIS 488-50, OBIS 647-120 and Sapphire 561-200-CW; Coherent) are combined with dichroic mirrors, expanded and focused to a position at the back focal plane of our objective that is controlled with a motorized stage so that the angle of the illumination light exiting the objective may vary. After the objective and tube lens the emission light passes through a cylindrical lens with a focal length of 700 mm to allow for 3D localization of individual molecules. Following the cylindrical lens a pair of relay lenses brings the image to an electron multiplying CCD camera (Ixon+ DU897E-CS0-BV; Andor). We recorded images at a frame rate of 60 Hz with continuous 640-nm excitation for the Alexa647. Activation of Alexa647 was controlled with a 405-nm laser using a power density of less than 1 W/cm^2.

4. Denditic network assembly assays:

4.1 General branched network assembly assay: Flow cells of micropatterned, NPF-coated coverslips were washed with twice with 250ul of ultra-pure water (Milli-Q grade) and disassembled by removal of the coverslips. Excess water was removed by a brief (5s) spin on a spin coater. Drying did not affect NPF activity if the coverslip was not kept in air for >30min. The coverslip was fixated on a custom-built sample holder by adhering to a thin PDMS O-ring and the whole assembly was transferred to the microscope stage. An ezrin-coated AFM cantilever was immobilized with a drop of hot paraffin wax on a custom built cantilever holder and then attached to the AFM head, which was mounted on the microscope and lowered to close proximity to the coverslip. 100 ml assembly buffer (20mM HEPES (pH=7.0), 100mM KCl, 20mM beta-Mercaptoethanol, 1.5mM $MgCl_2$, 1mM EGTA, 1mM ATP, 0.5mg/ml betacasein, 10nM Alexa488-labelled actin) were added in between coverslip and cantilever holder. Low amounts of labelled actin were included in the buffer to visualize the NPF patterns indirectly via the binding of actin monomers. 80ul of mineral oil containing 20mg/ml Cithrol DPHS (to passivate the oilbuffer interface) was overlaid onto the buffer to seal if from air exposure. The Optical Lever Sensitivity (OLS) is characterized by measuring the force-distance curve in contact with the hard glass surface, prior to every measurement. An NPF pattern was then positioned at an axial distance of 3um directly under the AFM cantilever via the motorized stage and the x- and y-piezoelectric stage control. Actin network growth was finally initiated by addition of 50μl of network proteins in assembly buffer (final concentration: 5μM actin, 5μM profilin, 100nM Arp2/3, 100nM CP if not indicated otherwise). Synchronously, multicolor TIRFM time-lapse imaging was initiated. For bulk fluorescence, multicolor TIRFM experiments, the protein mix was supplemented with 1%Alexa488-actin, 5% Alexa647-Arp2/3 and 15% TMR-SNAP-CP. After the height of the growing network reached the cantilever (as indicated by cantilever displacement and a rise in force), the force was kept constant at a defined setpoint by engaging the force-feedback mechanism (“force-clamp mode”). The force was maintained until both network fluorescence and growth velocity reached a steady state, upon which the force was changed to a higher setpoint. This cycle was repeated until network growth was slowed to velocities <200 nm/min, close to mechanical stall. Network growth did not exhibit hysteresis, hence the order or duration by which the individual forces were applied did not affect the growth velocity (Supplemental Fig. 3).

4.2 Single molecule branched network assembly assay for TIRFM-AFM: Assays were carried out as described in the section 4.1 with the following exceptions: For single color, single molecule imaging, assembly buffer was supplemented with an oxygen scavenger system (40mM glucose, 125 g/ml glucose oxidase, 40 g/ml catalase) and

2mM Trolox and the protein mix contained either 0.02% (1 in 5000) Alexa647-Arp2/3, 0.02% (1 in 5000) Alexa647-SNAP-CP or 0.000066% (1 in 1500000) Alexa647-Actin.

4.3 “Arrest and label” assay for the visualization of free barbed ends by TIRF-AFM: Assays were carried out as described in the section 4.1 with the following exceptions: Assembly buffer was supplemented with an oxygen scavenger system (40mM glucose, 125 μg/ml glucose oxidase, 40 μg/ml catalase) and 2mM Trolox and the protein mix contained only Alexa488-Actin (1% of total) as fluorescent label. The force was maintained a single setpoint until the network reached steady state growth and a minimum height of >5 μm. Network growth was then arrested by carefully diluting the reaction (150 μl total) by adding 400 μl fixing buffer (assembly buffer containing Latrunculin B (15M final), Phalloidin (15 μM final) and TMR-CP (100nM final; the fraction of labelled capping after arrest was thus 100nM of 127nM total, hence 79% of total). Synchronous addition of Latrunculin and Phalloidin has previously been shown to maintain the ratio of filamentous and polymeric actin in branched networks (Akin and Mullins, 2008). Therefore, labeled capping protein can, after its addition, immediately bind to available free ends as well as capped ends that become uncapped during further incubation of the sample (turnover). This turnover fraction can be quantified and subtracted from the data (see section 5.3).

4.4 “Arrest and label” assay for the visualization of free barbed ends by 3D STORM-AFM: Assays were carried out as described in the previous section (4.3) with the following exceptions: Reactions were scaled down to half of the volume (75μl total in comparison to 150μl for standard conditions) and did not contain Trolox. Network growth was arrested by carefully diluting the reaction (75μl total) by adding 25μl fixing buffer (assembly buffer containing Latrunculin B (15μM final), Phalloidin (15μM final) and Alexa647-CP (30μM final). The fraction of labelled capping after arrest was therefore 30nM of 105nM total, hence 28%. This lower labeling fraction (compared to section 4.3) was required to achieve labeling densities suitable for single molecule STORM imaging. We inhibited further capping after 150s after network arrest by addition of 1ml dilution mix (assembly buffer containing Latrunculin B (1μM final), Phalloidin (1μM final), an oxygen scavenger system (40mM glucose, 125 μg/ml glucose oxidase, 40μg/ml catalase), 1mM beta-Mercaptoethanol and 3.7μM Myotrophin (competitive, high-affinity CP inhibitor (Bhattacharya et al., 2006)). The short incubation period with labeled CP after arrest (150s) was sufficient for the near complete capping of all free ends (Supplemental Fig. 4), but minimized the contribution of the turnover fraction of already capped ends to the overall signal.

4.5 Measurement of network mechanical properties: After the actin network reached a height of 10μm, LatrunculinB (15μM final) was added to the reaction to terminate further actin polymerization and kinetically arrest the network. To avoid large force fluctuations during this arrest step, the AFM force clamp was transiently disengaged at the point of addition and turned back on once the vertical AFM signal stabilized. Potential drift in the vertical signal or the AFM stage during assembly and arrest was corrected for by carefully disengaging the AFM cantilever from the actin network, moving to a position away from the network and bringing it into contact with the coverslip surface to recalibrate the surface position. After 10min following kinetic arrest, the AFM cantilever was positioned back to the top of actin network. The height and the elasticity of the actin network were first measured at minimum load stress (12.5-25 pN/μm^2). The load force was then gradually increased in form of a load cycle (Supplemental Fig. 7), with 1min long steps at the low stress 12.5-25 pN/μm^2) alternating with 1min long steps at increasing high stresses. Actin fluorescence, sample rheology amplitude and phase as well as sample height were continuously measured during assembly of the network and the load cycles after arrest and further processed for data analysis (Section 5.8-9). To study the growth velocity of actin network against a defined external stiffness (Fig. 7), we first grew the actin network at a constant growth force (under force clamp conditions, hence at zero external stiffness) until a height of 4um had been reached and then disengaged the force clamp. Disengaging the force clamp results in the network pushing against the defined external stiffness of the cantilever, to which we refer as stiffness clamp mode. The external stiffness was varied by using cantilevers with different force constants (0.1-0.01 N/m).

5. Data analysis:

5.1 Quantification of network growth velocity: Constant growth forces were applied to a growing network under AFM force clamp control. The growth velocity of the network was determined by the slope of height-time curve at individual constant growth forces. However after switching to a new growth force, the network needed time to adapt the new growth force to reach constant growth. Therefore, the slope is not considered for growth velocity until the network reached the steady constant growth where the slope is constant.

5.2 Quantification of bulk fluorescence intensities from TIRFM and confocal imaging:
The mean intensities of all network components (actin, Arp2/3, CP) from multicolor, time-lapse TIRFM images were quantified via ImageJ (ROI Manager->Multi Measure function) from square region of interests (ROIs) matching the network area. Background intensity was determined from adjacent regions (10um distance) of the same size and subtracted from the network intensity. For Arp2/3 and actin, a small (<30% of total intensity in the absence of force for TIRFM imaging, <5% for confocal imaging) fraction of fluorescence in the network area is due to binding to the NPF in addition to the actin network. The intensity of this signal was quantified during the initial lag phase preceding actin network nucleation and subtracted from the network intensity. The fluorescence intensities were plotted as a function of time together with the height of the sample as well the counterforce. Mean fluorescence intensities at were then calculated by averaging over the fluorescence signal during steady growth at a constant force. The variance in fluorescence intensity during these steady state periods was very low (SD<2% total).

5.3 Quantification of free barbed end densities from TIRFM imaging: Fluorescence intensities following network arrest and synchronous TMR-CP addition were determined as described in the previous section and plotted as function of time. Fluorescence intensity traces consisted of a rapid, exponential phase which corresponded to immediate capping of available free ends, as well as a slow, linear phase that can be attributed to slow uncapping and recapping (turnover) of capped ends throughout the branched network. We established in control experiments that this slow turnover can indeed be approximated to be linear over the timescale of our experiment (Supplemental Fig. 4). We thus fitted the data with a sum of an exponential and a linear function: with Ifree being the amplitude of the rapid exponential capping phase. Ifree is therefore a measure of the amount of free uncapped ends.

5.4 Quantification of free barbed end densities from STORM imaging: Actin networks were imaged with the STORM microscope described in section 3.3. We recorded a sequence of images with two actin networks in the frame: one without an applied force and one with a force from the AFM. Each sequence typically contained 15000 images and we recorded an image sequence at multiple focal planes including at the coverslip, 400 nm beyond the coverslip and 800 nm beyond the coverslip. For each image in a sequence, fluorescent spots were identified and fit to an elliptical Gaussian function to find their positions, intensities, widths and ellipticities. Spots too dim, wide or elliptical were discarded from further analysis. Based on the ellipticity of the fitted Gaussian function we were able to localize each molecule in z (Huang et al., 2008). In comparing the forced and unforced networks we looked at the distribution of the localized molecules' positions in z and the total number of localized molecules in each network. To correct for uneven illumination in the field of view containing the two networks which would bias the relative number of localized molecules, we recorded multiple sequences of images containing two networks that were both unforced under identical conditions to those experiments with one forced and one unforced network. These controls allowed us to correct the number of localized molecules according to where in the image plane the network resided.

5.5 Single molecule tracking and classification: For detection and tracking of single actin, Arp2/3 and capping protein molecules in TIRF time-lapse images, we used the u-track software package (Jaqaman et al., 2008). After complete tracking, an additional step classifies tracks into productive (molecules that are incorporated into the network and continuously grow out of the TIRF microscopy field of view as indicated by a progressive drop in fluorescence intensity) or unproductive (stuck and/or blinking molecules at constant intensity and position). This is done in a semi-automated process: All individual tracks of minimum length 5 frames (= 500 ms) are randomly distributed amongst six biological experts. Each expert subsequently classifies all individual tracks of his share as productive or unproductive. In this step, 10% of all tracks are classified by two experts independently to estimate the classification uncertainty. This led to a fraction of tracks of at least 90% over all sample clips that is associated to the same class by both experts. In order to efficiently process significant amounts of microscopy data, we further automated our analysis procedure, by calculating a set of 10 feature parameters for each track. All features are based on the dynamics of intensity and position of each track. The set of features in combination with the combined classification results of the experts was used subsequently for training a supervised random forest classifier. Cross validation yielded correct classification in at least 82% of all tracks. In order to further improve this performance, we followed an active learning strategy in which borderline cases (i.e. tracks for which the decision trees in the forest do not agree well in their classification decision) are decided by an expert. Using cross validation of this semi-automated procedure, the amount of manually classified tracks is tuned to yield a comparably high correct classification performance as the group of experts (i.e. > ~90%). After classification, productive tracks are used in further analyses exclusively.

5.6 Determination of biochemical assembly rates, filament lengths and network densities from single molecule experiments: The mean event rates of productive network incorporation (in counts per network per second) was determined for all network components (actin, Arp2/3 and CP) from single molecule "spike-in" experiments at 5nN and multiplied by the respective labeling ratio to yield the total polymerization, nucleation and capping rate at this force. The average filament length (in number of monomers) at 5nN was calculated by the either ratio of the polymerization rate to the nucleation or capping rate and expressed in nm by assuming 377 actin monomers per 1000nm of filament. Filament lengths determined by either ratio were in excellent quantitative agreement with each other, as a result of the similar nucleation and capping rates. The average network density at 5nN was determined by dividing the average polymerization rate (monomers/s) by the volume rate (product of the network area and the average growth velocity expressed as l/s) and expressed as M. The values of all these quantities determined at 5nN served as a calibration for their corresponding bulk fluorescence measurements which were carried out over the whole force regime. For instance, the normalized actin flux as a function of force (Figure 2E) was multiplied by the polymerization rate at 5nN (Figure 2F) to determine the polymerization rate as a function of force.

5.7 Determination of mechanical, biochemical power and energy efficiency: The mechanical power of the network was determined by the product of the network growth velocity and the external force (Figure 2B) and expressed as k_BT/s. The rate of energy consumption was calculated by the product of the network polymerization rate (monomers/s per network) and the free energy change per monomer polymerized, which was determined by with $k_{on} = 4.8\ s^{-1}\ uM^{-1}$ (which was determined from single filament TIRFM polymerization experiments and found to be slightly lower for our cytoplasmic profilin-actin complex compared to literature values for muscle actin) and $k_{off} = 1\ s^{-1}$ (Kuhn and Pollard, 2005). We therefore assume a free energy change of 3.18 k_BT or 13.07 pN nm per monomer polymerized for our experimental conditions. The ratio of the mechanical power and the rate of energy consumption yields the dimensionless energy efficiency.

5.8 Determination of sample elasticity from microrheology measurements: Based on the definition of viscoelasticity, when a viscoelastic material is deformed by a sinusoidal compression, the elastic modulus (*G'*) could be written as $G' = \frac{\sigma_0}{\varepsilon_0}\cos\theta$, where σ_0 and ε_0 are the amplitudes of stress and strain and θ is the phase shift between them. In our measurements, amplitude (X_0) and phase shift (θ) of the oscillatory normal deflection were detected by a lock-in amplifier. Together with the applied amplitude of z-piezo (D_0) and characterized cantilever spring constant (k), NPF pattern area (A), and network height (H), the amplitude of stress and strain of the network can be written as

$\sigma_0 = \frac{X_0 k}{A}$ and $\varepsilon_0 = \frac{D_0 - X_0}{H}$. Therefore the elastic modulus is re-written as $G' = \frac{X_0 k H}{A(D_0 - X_0)} \cos\theta$. Before each measurement, the oscillating cantilever was put in contact with a hard surface to characterize the reference phase and z-piezo amplitude at different forces to obtain reference values for θ and D_0.

5.9 Estimation of composite network elasticity: To calculate the load force-dependent total elasticity of network that grew under two different growth forces, we first calculated the spring constant of each "layer" from elasticity by $k = \frac{G'A}{H}$, where *A* is the cross section area, *H* is the thickness, and *G'* is the elastic modulus of that layer. With the spring constants of two layers (k_1 and k_2) in series, the total spring constant (k_{total}) follows $\frac{1}{k_{total}} = \frac{1}{k_1} + \frac{1}{k_2}$. In the final, the total elastic modulus of the whole network can be calculated by $G'_{total} = k_{total} \frac{H_{total}}{A_{total}}$, where $A_{total} = A_1 = A_2$ in our experiments. In summary, the elastic modulus of the composite network with two layers can be written as $G'_{total} = \frac{G'_1 G'_2 (H_1 + H_2)}{A_{total}(H_1 G'_2 + H_2 G'_1)}$. Please note that both G'$_1$ and G'$_2$ are load force-dependent as well as H_1 and H_2. The initial H1 and H2 were characterized in each composite measurement.

5.10 Prediction of grow velocity from network and external elasticity: To calculate the growth velocity of the network after changing from force clamp mode to free deflection mode, we have to consider the elasticity of network and the spring constant of cantilever. At the moment of switching the AFM from force clamp to free deflection mode, two assumptions have to be made to predict the growth velocity after disengaging the force clamp: 1) the force applied to the network is the nearly the same is nearly the same before and right after switching off the force clamp; 2) the network and the cantilever are acting physically as two springs in series. Both of these assumptions hold for the short timescale of these experiments. Therefore the growth of network under constant force conditions ($\Delta X_{force\ constant}$) will be equal to the deflection of network ($\Delta X_{network}$) and cantilever ($\Delta X_{cantilever}$) in constant stiffness mode, $\Delta X_{force\ constant} = \Delta X_{network} + \Delta X_{cantilever}$; and force can be written as $F = \Delta X_{cantilever} k_{cantilever} = (\Delta X_{cantilever} + \Delta X_{network}) k_{total}$, where $k_{total} = \frac{k_{cantilever} k_{network}}{k_{cantilever} + k_{network}}$. Under conditions of constant external stiffness, the growth velocity is measured by the change of cantilever deflection, which is $\Delta X_{cantilever}$. By all the equations above, we can obtain $\Delta X_{cantilever} = \Delta X_{force\ constant} \frac{k_{network}}{k_{cantilever} + k_{network}}$. The predicted growth velocity after disengaging the force clamp can thus be obtained from $V_{stiffness\ constant} = V_{force\ constant} \frac{k_{network}}{k_{cantilever} + k_{network}}$, where the spring constant of network can be extracted by $k_{network} = \frac{G'_{network} A}{H}$ ($G'_{network}$, *A*, and *H* are elastic modulus, cross section area, and height of the network).

References:

1. Akin, O., and Mullins, R.D. (2008). Capping protein increases the rate of actin-based motility by promoting filament nucleation by the Arp2/3 complex. Cell *133*, 841–851.
2. Beltzner, C.C., and Pollard, T.D. (2008). Pathway of actin filament branch formation by Arp2/3 complex. J. Biol. Chem. *283*, 7135–7144.
3. Bhattacharya, N., Ghosh, S., Sept, D., and Cooper, J.A. (2006). Binding of myotrophin/V-1 to actin-capping protein: implications for how capping protein binds to the filament barbed end. J. Biol. Chem. *281*, 31021–31030.
4. Bisi, S., Disanza, A., Malinverno, C., Frittoli, E., Palamidessi, A., and Scita, G. (2013). Membrane and actin dynamics interplay at lamellipodia leading edge. Curr. Opin. Cell Biol. *25*, 565–573.
5. Carter, N.J., and Cross, R.A. (2005). Mechanics of the kinesin step. Nature *435*, 308–312.
6. Chaudhuri, O., Parekh, S.H., and Fletcher, D.A. (2007). Reversible stress softening of actin networks. Nature *445*, 295–298.
7. Clark, A.G., Miller, A.L., Vaughan, E., Yu, H.-Y.E., Penkert, R., and Bement, W.M. (2009). Integration of single and multicellular wound responses. Curr. Biol. *19*, 1389–1395.
8. Flanagan, L.A., Chou, J., Falet, H., Neujahr, R., Hartwig, J.H., and Stossel, T.P. (2001). Filamin A, the Arp2/3 complex, and the morphology and function of cortical actin filaments in human melanoma cells. J. Cell Biol. *155*, 511–517.
9. Fletcher, D.A., and Mullins, R.D. (2010). Cell mechanics and the cytoskeleton. Nature *463*, 485–492.
10. Fourniol, F.J., Li, T.-D., Bieling, P., Mullins, R.D., Fletcher, D.A., and Surrey, T. (2014). Micropattern-guided assembly of overlapping pairs of dynamic microtubules. Meth. Enzymol. *540*, 339–360.
11. Gardel, M.L., Valentine, M.T., Crocker, J.C., Bausch, A.R., and Weitz, D.A. (2003). Microrheology of entangled F-actin solutions. Phys. Rev. Lett. *91*, 158302.
12. Gardel, M.L., Shin, J.H., MacKintosh, F.C., Mahadevan, L., Matsudaira, P.A., and Weitz, D.A. (2004a). Scaling of F-actin network rheology to probe single filament elasticity and dynamics. Phys. Rev. Lett. *93*, 188102.
13. Gardel, M.L., Shin, J.H., MacKintosh, F.C., Mahadevan, L., Matsudaira, P., and Weitz, D.A. (2004b). Elastic behavior of cross-linked and bundled actin networks. Science *304*, 1301–1305.
14. Gardel, M.L., Nakamura, F., Hartwig, J.H., Crocker, J.C., Stossel, T.P., and Weitz, D.A. (2006). Prestressed F-actin networks cross-linked by hinged filamins replicate mechanical properties of cells. Proc. Natl. Acad. Sci. U.S.A. *103*, 1762–1767.
15. Gardel, M.L., Sabass, B., Ji, L., Danuser, G., Schwarz, U.S., and Waterman, C.M. (2008). Traction stress in focal adhesions correlates biphasically with actin retrograde flow speed. J. Cell Biol. *183*, 999–1005.
16. Hill, T.L., and Kirschner, M.W. (1982). Bioenergetics and kinetics of microtubule and actin filament assembly-disassembly. Int. Rev. Cytol. *78*, 1–125.

17. Huang, B., Wang, W., Bates, M., and Zhuang, X. (2008). Three-dimensional super-resolution imaging by stochastic optical reconstruction microscopy. Science *319*, 810–813.
18. Insall, R.H., and Machesky, L.M. (2009). Actin dynamics at the leading edge: from simple machinery to complex networks. Dev. Cell *17*, 310–322.
19. Janmey, P.A., and McCulloch, C.A. (2007). Cell mechanics: integrating cell responses to mechanical stimuli. Annu Rev Biomed Eng *9*, 1–34.
20. Janmey, P.A., Euteneuer, U., Traub, P., and Schliwa, M. (1991). Viscoelastic properties of vimentin compared with other filamentous biopolymer networks. J. Cell Biol. *113*, 155–160.
21. Kasza, K.E., Rowat, A.C., Liu, J., Angelini, T.E., Brangwynne, C.P., Koenderink, G.H., and Weitz, D.A. (2007). The cell as a material. Curr. Opin. Cell Biol. *19*, 101–107.
22. MacKintosh, null, Käs, null, and Janmey, null (1995). Elasticity of semiflexible biopolymer networks. Phys. Rev. Lett. *75*, 4425–4428.
23. Maly, I.V., and Borisy, G.G. (2001). Self-organization of a propulsive actin network as an evolutionary process. Proc. Natl. Acad. Sci. U.S.A. *98*, 11324–11329.
24. Marcy, Y., Prost, J., Carlier, M.-F., and Sykes, C. (2004). Forces generated during actin-based propulsion: a direct measurement by micromanipulation. Proc. Natl. Acad. Sci. U.S.A. *101*, 5992–5997.
25. Mogilner, A., and Oster, G. (1996). Cell motility driven by actin polymerization. Biophys. J. *71*, 3030–3045.
26. Mogilner, A., and Oster, G. (2003). Force generation by actin polymerization II: the elastic ratchet and tethered filaments. Biophys. J. *84*, 1591–1605.
27. Mooren, O.L., Galletta, B.J., and Cooper, J.A. (2012). Roles for actin assembly in endocytosis. Annu. Rev. Biochem. *81*, 661–686.
28. Mullins, R.D., Heuser, J.A., and Pollard, T.D. (1998). The interaction of Arp2/3 complex with actin: nucleation, high affinity pointed end capping, and formation of branching networks of filaments. Proc. Natl. Acad. Sci. U.S.A. *95*, 6181–6186.
29. Nakamura, F., Osborn, E., Janmey, P.A., and Stossel, T.P. (2002). Comparison of filamin A-induced cross-linking and Arp2/3 complex-mediated branching on the mechanics of actin filaments. J. Biol. Chem. *277*, 9148–9154.
30. Nakamura, F., Osborn, T.M., Hartemink, C.A., Hartwig, J.H., and Stossel, T.P. (2007). Structural basis of filamin A functions. J. Cell Biol. *179*, 1011–1025.
31. Padrick, S.B., Cheng, H.-C., Ismail, A.M., Panchal, S.C., Doolittle, L.K., Kim, S., Skehan, B.M., Umetani, J., Brautigam, C.A., Leong, J.M., et al. (2008). Hierarchical regulation of WASP/WAVE proteins. Mol. Cell *32*, 426–438.
32. Pantaloni, D., and Carlier, M.F. (1993). How profilin promotes actin filament assembly in the presence of thymosin beta 4. Cell *75*, 1007–1014.
33. Parekh, S.H., Chaudhuri, O., Theriot, J.A., and Fletcher, D.A. (2005). Loading history determines the velocity of actin-network growth. Nat Cell Biol *7*, 1219–1223.
34. Peskin, C.S., Odell, G.M., and Oster, G.F. (1993). Cellular motions and thermal fluctuations: the Brownian ratchet. Biophys. J. *65*, 316–324.

35. Pollard, T.D., and Cooper, J.A. (2009). Actin, a central player in cell shape and movement. Science *326*, 1208–1212.
36. Prass, M., Jacobson, K., Mogilner, A., and Radmacher, M. (2006). Direct measurement of the lamellipodial protrusive force in a migrating cell. J. Cell Biol. *174*, 767–772.
37. Pujol, T., Roure, O. du, Fermigier, M., and Heuvingh, J. (2012). Impact of branching on the elasticity of actin networks. Proc. Natl. Acad. Sci. U.S.A. *109*, 10364–10369.
38. Renkawitz, J., Schumann, K., Weber, M., Lämmermann, T., Pflicke, H., Piel, M., Polleux, J., Spatz, J.P., and Sixt, M. (2009). Adaptive force transmission in amoeboid cell migration. Nat. Cell Biol. *11*, 1438–1443.
39. Reymann, A.-C., Martiel, J.-L., Cambier, T., Blanchoin, L., Boujemaa-Paterski, R., and Théry, M. (2010). Nucleation geometry governs ordered actin networks structures. Nat Mater *9*, 827–832.
40. Reymann, A.-C., Suarez, C., Guérin, C., Martiel, J.-L., Staiger, C.J., Blanchoin, L., and Boujemaa-Paterski, R. (2011). Turnover of branched actin filament networks by stochastic fragmentation with ADF/cofilin. Mol. Biol. Cell *22*, 2541–2550.
41. Schafer, D.A., Jennings, P.B., and Cooper, J.A. (1996). Dynamics of capping protein and actin assembly in vitro: uncapping barbed ends by polyphosphoinositides. J. Cell Biol. *135*, 169–179.
42. Smith, B.A., Daugherty-Clarke, K., Goode, B.L., and Gelles, J. (2013). Pathway of actin filament branch formation by Arp2/3 complex revealed by single-molecule imaging. Proc. Natl. Acad. Sci. U.S.A. *110*, 1285–1290.
43. Storm, C., Pastore, J.J., MacKintosh, F.C., Lubensky, T.C., and Janmey, P.A. (2005). Nonlinear elasticity in biological gels. Nature *435*, 191–194.
44. Stricker, J., Falzone, T., and Gardel, M.L. (2010). Mechanics of the F-actin cytoskeleton. J Biomech *43*, 9–14.
45. Svitkina, T.M., and Borisy, G.G. (1999). Arp2/3 complex and actin depolymerizing factor/cofilin in dendritic organization and treadmilling of actin filament array in lamellipodia. J. Cell Biol. *145*, 1009–1026.
46. Theriot, J.A. (2000). The polymerization motor. Traffic *1*, 19–28.
47. Tilney, L.G., Bonder, E.M., Coluccio, L.M., and Mooseker, M.S. (1983). Actin from Thyone sperm assembles on only one end of an actin filament: a behavior regulated by profilin. J. Cell Biol. *97*, 112–124.
48. Vinzenz, M., Nemethova, M., Schur, F., Mueller, J., Narita, A., Urban, E., Winkler, C., Schmeiser, C., Koestler, S.A., Rottner, K., et al. (2012). Actin branching in the initiation and maintenance of lamellipodia. J. Cell. Sci. *125*, 2775–2785.
49. Wachsstock, D.H., Schwartz, W.H., and Pollard, T.D. (1993). Affinity of alpha-actinin for actin determines the structure and mechanical properties of actin filament gels. Biophys. J. *65*, 205–214.
50. Weichsel, J., Urban, E., Small, J.V., and Schwarz, U.S. (2012). Reconstructing the orientation distribution of actin filaments in the lamellipodium of migrating keratocytes from electron microscopy tomography data. Cytometry A *81*, 496–507.

51. Welch, M.D., and Way, M. (2013). Arp2/3-mediated actin-based motility: a tail of pathogen abuse. Cell Host Microbe *14*, 242–255.
52. Wu, C., Asokan, S.B., Berginski, M.E., Haynes, E.M., Sharpless, N.E., Griffith, J.D., Gomez, S.M., and Bear, J.E. (2012). Arp2/3 is critical for lamellipodia and response to extracellular matrix cues but is dispensable for chemotaxis. Cell *148*, 973–987.
53. Yamaguchi, H., Lorenz, M., Kempiak, S., Sarmiento, C., Coniglio, S., Symons, M., Segall, J., Eddy, R., Miki, H., Takenawa, T., et al. (2005). Molecular mechanisms of invadopodium formation: the role of the N-WASP-Arp2/3 complex pathway and cofilin. J. Cell Biol. *168*, 441–452.
54. Alcaraz, J., Buscemi, L., Grabulosa, M., Trepat, X., Fabry, B., Farré, R., and Navajas, D. (2003). Microrheology of human lung epithelial cells measured by atomic force microscopy. Biophys. J. *84*, 2071–2079.
55. Bhattacharya, N., Ghosh, S., Sept, D., and Cooper, J.A. (2006). Binding of myotrophin/V-1 to actin-capping protein: implications for how capping protein binds to the filament barbed end. J. Biol. Chem. *281*, 31021–31030.
56. Doolittle, L.K., Rosen, M.K., and Padrick, S.B. (2013). Purification of native Arp2/3 complex from bovine thymus. Methods Mol. Biol. *1046*, 231–250.
57. Edelstein, A., Amodaj, N., Hoover, K., Vale, R., and Stuurman, N. (2010). Computer control of microscopes using µManager. Curr Protoc Mol Biol *Chapter 14*, Unit14.20.
58. Fourniol, F.J., Li, T.-D., Bieling, P., Mullins, R.D., Fletcher, D.A., and Surrey, T. (2014). Micropattern-guided assembly of overlapping pairs of dynamic microtubules. Meth. Enzymol. *540*, 339–360.
59. Hansen, S.D., Zuchero, J.B., and Mullins, R.D. (2013). Cytoplasmic actin: purification and single molecule assembly assays. Methods Mol. Biol. *1046*, 145–170.
60. Huang, B., Wang, W., Bates, M., and Zhuang, X. (2008). Three-dimensional super-resolution imaging by stochastic optical reconstruction microscopy. Science *319*, 810–813.
61. Jaqaman, K., Loerke, D., Mettlen, M., Kuwata, H., Grinstein, S., Schmid, S.L., and Danuser, G. (2008). Robust single-particle tracking in live-cell time-lapse sequences. Nat. Methods *5*, 695–702..
62. Keppler, A., Gendreizig, S., Gronemeyer, T., Pick, H., Vogel, H., and Johnsson, K. (2003). A general method for the covalent labeling of fusion proteins with small molecules in vivo. Nat. Biotechnol. *21*, 86–89.
63. Kuhn, J.R., and Pollard, T.D. (2005). Real-time measurements of actin filament polymerization by total internal reflection fluorescence microscopy. Biophys. J. *88*, 1387–1402.
64. Mahaffy, R.E., Shih, C.K., MacKintosh, F.C., and Käs, J. (2000). Scanning probe-based frequency-dependent microrheology of polymer gels and biological cells. Phys. Rev. Lett. *85*, 880–883.

Chapter 4

Mechanosensitive Binding of Regulatory Proteins to Branched Actin Structures: A study of Cofilin and Tropomyosin

This chapter is in collaboration with Tai-De Li, Peter Bieling and Daniel A. Fletcher

Abstract:

The leading edge of a migrating cell consists of two populations of actin structures: the lamellipod, which is characterized by branched networks of short actin filaments, and the lamellum, which is characterized by unbranched networks of long actin filaments. Regulatory proteins such as tropomyosin and cofilin bind preferentially to each population, resulting in divergent architectures and dynamic properties of network assembly and turnover. It remains unclear how actin binding proteins (ABPs) in these and other actin networks are spatially segregated. Elucidating the driving force of ABP spatial segregation is critical for understanding actin network kinetics and function in a broad range of cellular contexts. In this chapter, we explore the role of mechanical cues in regulating cofilin and tropomyosin binding to distinct actin structures. To do so, we used in-vitro reconstitution approaches coupled with atomic force microscopy to grow branched actin networks and subject them to mechanical perturbations. We then followed cofilin and tropomyosin binding to networks nucleated under various growth forces. Our preliminary findings show that cofilin preferentially binds to actin structures under compression while tropomyosin binds to relaxed structures. These effects are time dependent and enhanced under higher growth forces.

Introduction:

Actin filaments are organized intracellularly in distinct structures that are critical to a range of biological functions (Blanchoin, 2014). While sharing the same cytoplasm, actin binding proteins (ABPs) localize differentially to these structures and modulate their dynamic properties. This differential binding is observed despite spatial proximity between distinct actin structures and homology between isoforms of the same family of proteins.

For example, at the leading edge of a cell, the lamellipod and the lamellum are within 0.5-1 μm proximity (Iwasa, 2007). Cofilin has been shown to exclusively bind and sever filaments within the lamellipod whereas tropomyosin binds and stabilizes filaments within the lamellum. Additionally, cytoplasmic tropomyosin isoforms have been shown to localize differentially in cells. While low and high molecular weight isoforms localize in stress fiber regions, only low molecular mass isoforms are found near the leading edge (Lin, 1988; Martin, 2008). In fact, the tropomyosin isoform Tm5NM1 of the γ-TM gene has been shown to promote stress fiber formation and recruit myosin II, whereas the tropomyosin isoform TmBr3 of the α-TM gene has been shown to promote lamellipodia formation and binds cofilin decorated filaments (Bryce, 2003; Gunning, 2005).

A key difference between these populations of filaments is their mechanical state. Filaments at the leading edge are subject to compressive forces and thought to have higher flexibility than filaments within stress fiber bundles which are subject to tensile forces (Finer, 1994). This polymorphism is significant in the context of actin binding proteins not just at the nanometer binding scale but also at the micrometer scale, since many proteins bind cooperatively (Michelot, 2011; Galkin, 2012). In fact, both cofilin and tropomyosin have been shown to drive changes in the actin filament's mechanical properties. Tropomyosin binding to the actin filament is believed to affect helical twist in an isoform-dependent manner by either stabilizing it or generating more disorder (Stokes, 1987; Ujfalusi, 2012). Cofilin in turn has been shown to increase the flexibility of filaments and decrease their crossover by 25% (McGough, 1997).

Furthermore, competition in binding between cofilin and tropomyosin has been reported in multiple studies (Ono, 2002; Bernstein, 1982). Bernstein and Bamburg correlated the stability of tropomyosin decorated F-actin to its protection from disassembly (Bernstein, 1982). Meanwhile, Nishida et al. observed gradual dissociation of bound tropomyosin upon increase in cofilin concentration (Nishida, 1984). While, tropomyosin and cofilin do not share same binding sites on the filament (McGough, 1998), the basis for this competition could be a favored filament structural state as tropomyosin favors stabilization in the actin filament (Gunning, 2005) and cofilin increases its variable twist (Prochniewicz, 2005).

These observations in addition to recent findings of decrease in severing activity of cofilin under tension (Uyeda, 2011) suggest that the mechanical state of the filament acts as a selecting marker for protein binding. In this chapter, we hypothesize that cofilin and tropomyosin binding to actin structures is mechanosensitive. This mechanoregulation could serve as a platform for further cooperative and/or competitive binding of ABPs, leading to spatial segregation of actin binding proteins.

Results:

Evaluating the mechanoregulation of protein binding

Using a combined in-vitro reconstitution assay, atomic force microscopy and confocal microscopy system, we evaluated differential binding of cofilin and skTM to actin structures under various mechanical perturbations.

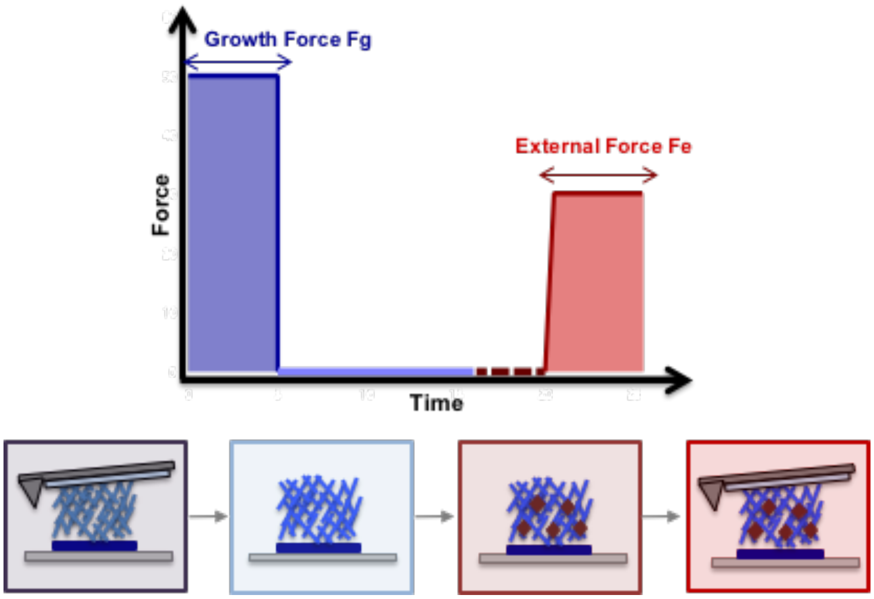

Figure 1: Schematic representation of force perturbations to reconstituted actin networks Networks are first grown under a growth force (Fg) up to 10μm height, fixed with latB and aged. ABP of interest is then introduced and additional mechanical perturbations are applied in the form of external force (Fe).

First, branched actin structures were reconstituted on NPF functionalized square islands using a minimal system of purified proteins (5 μM actin, 5 μM profilin, 100 nM Arp2/3 and 100 nM Capping protein) and as described in Chapter 3 (Bieling, 2016). Network growth was opposed with external compressive forces denoted as Fg and ranging between 0-150 nN. Force application was maintained constant in a feedback controlled clamp mode and achieved using a tipless cantilever. The later was functionalized using silane-PEG-maleimide chemistry and coated with ezrin's actin binding domain to prevent slippage at the actin-cantilever interface. Growth was arrested at a 10 μm height by adding latrunculin B (latB) and the actin binding protein of interest was then introduced. In the case of cofilin, networks were aged for 10 min prior to ABP addition in order to ensure conversion of actin monomers from the ATP to ADP state (Carlier, 1986).

Spatiotemporal binding of ABP to the three dimensional actin structures was followed using a confocal microscope. Z-stacks and time-lapses were acquired in dual color experiments where the actin monomers and binding protein of interest were labeled. In order to evaluate bias in protein binding to a mechanical state, the background corrected ratio of the binding intensity in the protein channel relative to the actin channel was compared between the actin structure that was subject to mechanical perturbation and the control structure. A relative ratio of 1 between the two conditions indicated no bias in binding, whereas a ratio larger than 1 indicated mechanosensitivity and preferential binding of the ABP to the compressive state. All controls were run in parallel to the perturbed network and nucleated in absence of any force input.

Mechanical state of actin structures biases cofilin and tropomyosin binding

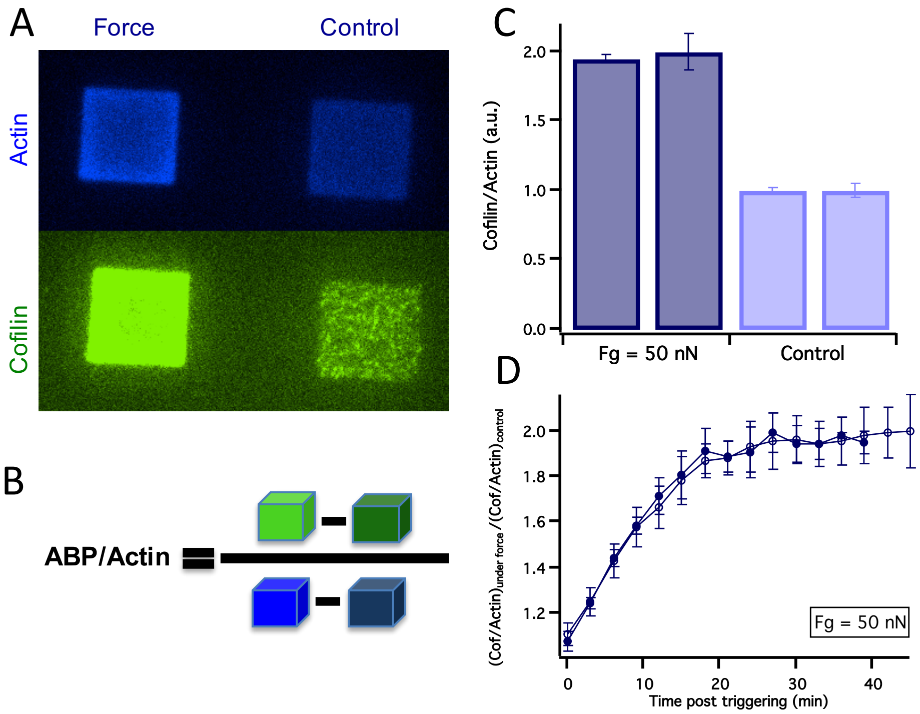

Figure 2: Cofilin preferentially binds to branched actin structures nucleated under compression A: Planar view of actin structures grown under compression (left) and control (right), B: Background adjusted ratiometric formula for binding intensities, C: Comparison of ratiometric values between networks nucleated under 50 nN force and control structures, D: Time dependent variation of mechanosensitive cofilin binding (Fg = 50 nN) (N = 2)

Our findings show that cofilin and tropomyosin are sensitive to the mechanical state of branched actin structures. When networks are grown under compressive forces, the actin density increases relative to the uncompressed networks as it has been observed by Bieling et al. (Bieling, 2016). Interestingly, we found that the amount of cofilin binding per unit volume of actin is double when the network is nucleated under 50 nN growth forces (Figure 2, C). This effect is time dependent and reaches steady state within 20 min of cofilin addition (Figure 2,D).

While cofilin binding is enhanced under compression, tropomyosin exhibits the opposite effect. Binding of tropomyosin to branched actin networks is mechanosensitive and favorable to control structures (Figure 3). These observations are consistent with the differential localization of cofilin and tropomyosin intracellularly as cofilin binds to flexible filaments in the lamellipodia while tropomyosin binds to stable filaments in the lamellum.

We next thought to investigate whether the mechanosensitive binding of these proteins is further enhanced under higher growth forces. Additionally, we asked whether the application of external force following arrest of nucleation can on its own bias ABP binding.

Cofilin and tropomyosin are sensitive to varying growth and external forces

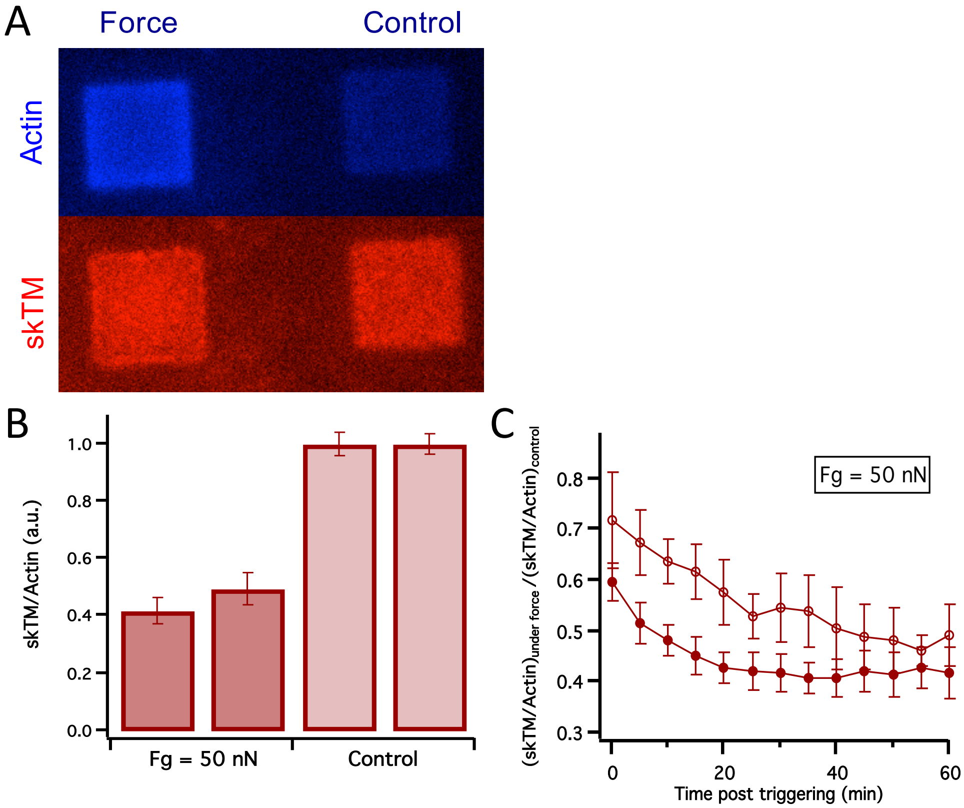

Figure 3: skTM preferentially binds to relaxed actin structures
A: Planar view of actin structures grown under compression (left) and control (right), B: Comparison of ratiometric values of background adjusted intensities between networks nucleated under 50 nN force and control structures, C: Time dependent variation of mechanosensitive tropomyosin binding (Fg = 50 nN) (open and closed circle curves correspond to two independent repeats)

Growing branched networks under higher range of forces further increases the differential in protein binding between the mechanically perturbed and the control network. Under growth forces of 150 nN, cofilin binding per unit actin increases four folds. Furthermore, tropomyosin binding to compressed structures is three folds lower under growth forces of 100 nN (Figure 4). While applying mechanical perturbations to nucleating actin structures alters their architectural and dynamic properties, parsing out the mechanism by which proteins respond to these mechanical perturbations remains challenging.

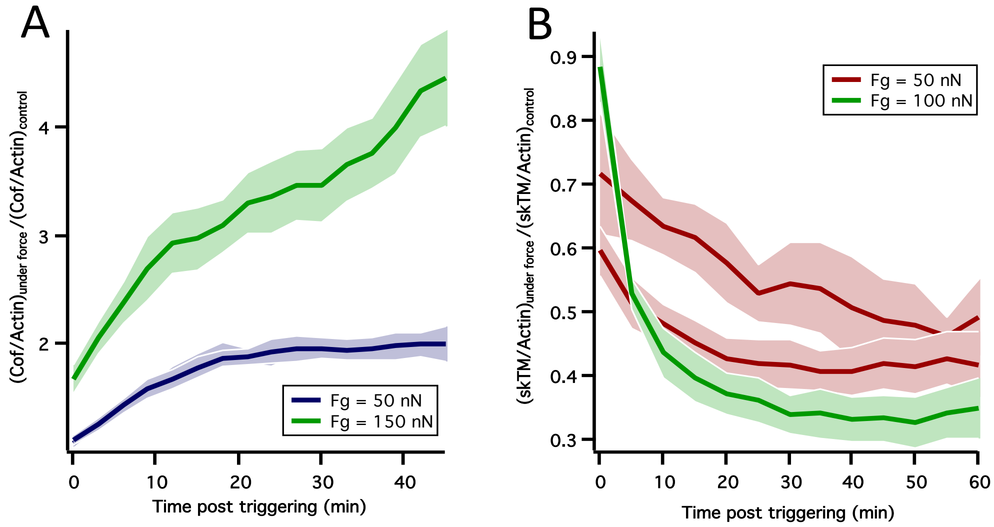

Figure 4: Differential binding of cofilin and tropomyosin is enhanced under higher growth forces A: Differential binding of cofilin between compressed and control networks for Fg = 50 nN and Fg = 150 nN, B: Differential binding of tropomyosin between compressed and control networks for Fg = 50 nN and Fg = 100 nN

To further simplify the system, we investigated whether external force alone applied to branched networks can bias binding in the absence of growth load. As these networks have lower actin density and elasticity, we monitored height data by tracking the cantilever position with time. We found that an external force (Fe) as low as 5 nN collapses the network (Figure 5A). We then asked whether external force applied to stiffer networks (grown under 50 nN load) affects soluble protein distribution. Our preliminary measurements indicate an incremental effect and increase in cofilin binding when networks are subject to 30 nN load following growth under 50 nN (Figure 5B).

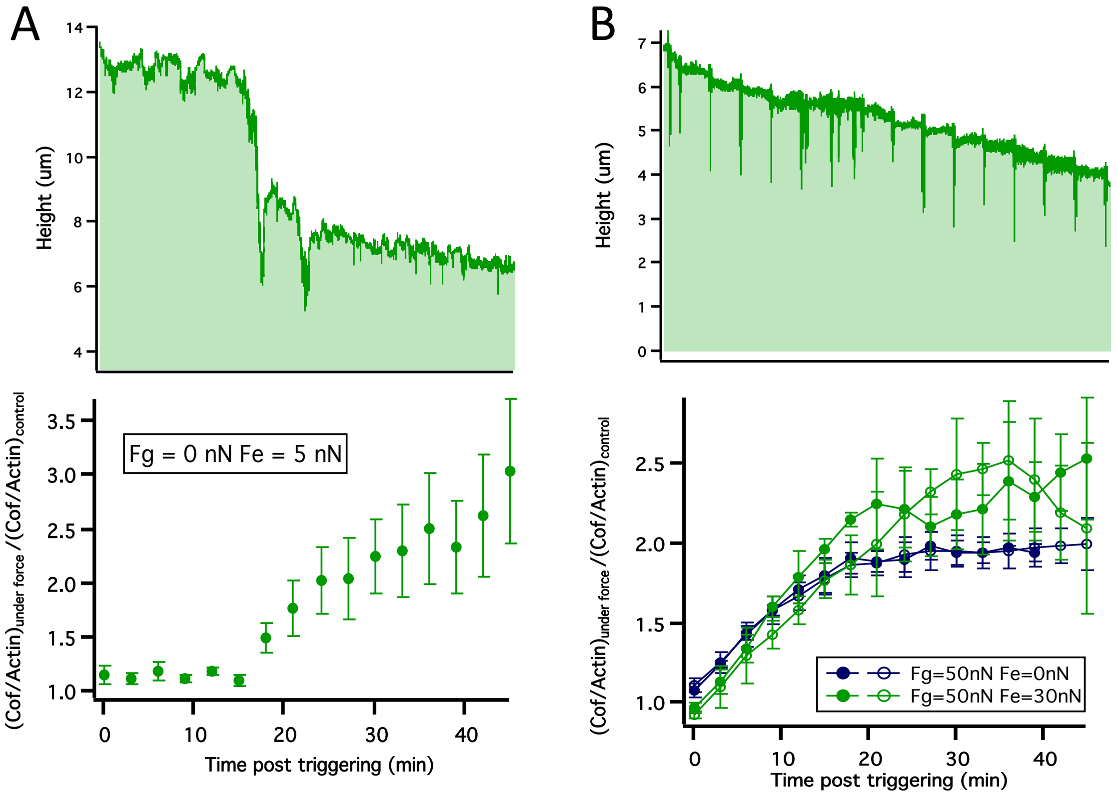

Figure 5: External forces in addition to growth forces bias cofilin binding to actin
Height and ratiometric binding of cofilin to compressed networks relative to control networks for structures subject to the following mechanical perturbations: A) Fg = 0 nN and Fe = 5 nN, B) Fg = 50 nN and Fe = 30 nN (open and closed circle curves correspond to independent experimental repeats)

Discussion:

At the core of the distinct kinetic and dynamic properties of actin structures lies a differential distribution of actin binding proteins. The factors driving the exclusive binding of ABPs and regulation of their corresponding actin networks remain unclear. Two such examples are cofilin and tropomyosin. These proteins are mutually exclusive, yet essential for regulating distinct activities of the actin structures they bind to.

Our findings in this chapter, although based on a limited number of experimental repeats and requiring further investigation, suggest that the mechanical state of the actin structure can bias binding of cofilin and tropomyosin. This bias is exhibited in Supp Figure 1 where actin networks are decorated with distinct levels of cofilin and tropomyosin despite being subject to the same biochemical conditions. The sole difference among these structures is the range of compressive forces and mechanical perturbations they are subject to.

While both cofilin and tropomyosin are sensitive to the mechanical state of the actin structures, cofilin preferentially binds to the compressive state of actin whereas tropomyosin favorably binds to the relaxed/uncompressed state. This effect is further enhanced at higher growth forces and under the application of external forces. Estimation of the elastic modulus of these networks shows mechanical stability over time. This finding suggests that the time dependent aspect of the mechanosensitive response could be due to the cooperativity in protein binding rather than structural remodeling (Supp Fig 2).

In summary, using atomic force microscopy combined with confocal microscopy we have probed the differential binding of cofilin and tropomyosin to branched actin networks. While this approach allows us to understand the effect of mechanical perturbations in a controlled in-vitro reconstituted system, it presents several limitations. In addition to the low throughput, understanding how the mechanical perturbations at a global network level translate to the single filament level is challenging. To address these challenges, we have developed a multi-scale biophysical approach for investigating the mechano-regulation of protein binding at the cellular, network and single filament levels. This study and its findings are discussed in the following chapter.

Methods:

Protein purification and labeling: Amoeba actin, arp2/3 complex, capping proteins, profilin and scar APVCA were purified and labeled as described in chapter 3 (Bieling, 2016). Alexa488 human-cofilin and rhodamine skeletal muscle tropomyosin were kind gifts from Peter Bieling and Viviana Risca respectively.

Cantilever and coverslip functionalization: Coverslips were functionalized as described in Chapter 2 using silane-PEG-maleimide chemistry and coated with mCherry APVCA at a final density of 80% mCherry APVCA (10 μM stock) and 20% dCherry (10 μM stock) in the following buffer: 20 mM Hepes pH 7.4, 350 mM NaCl, 1 mM EDTA. The density of nucleation promoting factor was determined for an optimal growth velocity of 8 μm/min in absence of force.

Tipless silicon cantilevers (Nanoworld, ARROW-TL2-50) with an average force constant of k = 0.03 N/m were used for force application. Force constant of cantilevers was re-measured using a commercial AFM system (BioScope Catalyst, Bruker). Calibrated cantilevers were cleaned, functionalized and coated with KCK-ezrin actin binding domain. Briefly, cantilevers were mounted on custom built Teflon holders and incubated in freshly prepared piranha solution (2:3 hydrogen peroxide: sulfuric acid) for 30 min. Holders were then dip-washed in 2x 1L milliQ beakers. Following piranha cleaning, individual cantilevers were dried on a microscope cover slide and mounted in a custom built PDMS chamber. PDMS chamber was then filled with functionalization mix and cantilevers left to incubate for 1.5hr at room temperature. Mix consisted of the following: 15 mg Ethoxy-silane-PEG maleimide (Nanocs, PG2-MLSL-2k) in 400 μL solution of 95% EtOH, 5% H2O pH = 5.0 (with acetic acid). Functionalized cantilevers were then washed 3x in ethanol (VWR, # V1001) and left to cure in 75deg oven for 1.5 hr. Next, they were dip-washed in 2x ethanol followed by a solution of 2 mM HEPES, pH 7.5. Finally, they were incubated in a 20 μM KCK-ezrin solution (2 mM HEPES, pH 7.5) overnight, washed 3x with 2 mM HEPES, pH 7.5 and stored in the later at 4 deg. For experiments where external force only rather than growth force was applied, cantilevers were piranha cleaned but not functionalized.

Experimental setup: Mechanical perturbations were done in an open configuration where reaction mix was separated from air interface via a mineral oil mix. Oil mix was prepared freshly as follows. PEG30-dipolyhydroxystearate (CRODA Inc, # 70142-34-6) was added to paraffin oil (Acros Organics, # 8012-95-1) at a final concentration of 20 mg/mL, vortexed at maximum speed to homogenize solution and finally sonicated for 30 min at 50 deg.

The final reaction mix was 185 μL in volume and consisted of three main premixes:

1. Base buffer mix (V = 110 μL) in 20 mM HEPES pH 7.0 with KOH:
    a. 1x MEH (20x stock: 400 mM HEPES pH 7.0, 30 mM $MgCl_2$, 20 mM EGTA)
    b. b-casein at a final concentration of 1 mg/mL (stock prepared at 20mg/mL in 20 mM HEPES pH 7.0)
    c. 100 mM KCl (stock: 20 mM HEPES pH 7.0 with KOH, 500 mM KCl)
2. Protein buffer mix (V = 55 μL):
    a. Buffer base: 100 mM KCl, 1x MEH and 100 μg/mL in 20 mM HEPES pH 7.0 with KOH
    b. 1x ATP-bME premix: 50x stock is 50 mM ATP and 1 μM beta-Mercaptoethanol in G-buffer (2 mM Tris-Cl pH 8.0, 0.2 mM ATP, 0.5 mM TCEP in 0.1 mM $CaCl_2$)
    c. Profilin, capping protein and arp2/3: Premix was prepared for a final concentration of 5 μM profilin, 100 nM capping proteins and 100 nM Arp2/3 in 20 mM HEPES, 100 mM KCl pH 7.0
    d. Actin premix: 5 μM final actin concentration in G-buffer. Labeled actin was used at 2% labeling ratio
3. Fixing mix (V = 20 μL):
    a. latrunculinB at final concentration of 15 μM in 20 mM HEPES, 100 mM KCl pH 7.0
    b. skTropomyosin/Cofilin: skTM was added at final concentration of 300 nM. In cofilin experiments, ABP was added in a separate shot after aging and at a final concentration of 100 nM. Cofilin concentration was optimized for a regime where the protein binds but doesn't severe (Andrianantoandro, 2006)

Network growth and mechanical perturbations using AFM: For each independent measurement, a new cantilever was mounted on custom-built holder using paraffin wax. NPF functionalized coverslips were mounted on 3D printed sample holders and clamped on microscope stage magnetically. 20 μL mineral oil was first added around the coverslip edge, the AFM head lowered and cantilever brought in close contact with the surface. Following addition of the 110 μL base buffer mix, 20 μL of mineral oil mix was added on top of aqueous phase. Patterned surface was then localized and cantilever centered on top of nucleating area at 1 μm height. To trigger growth, protein buffer mix was added and force clamp of desired growth force was set. Growth was allowed to proceed until the network reached 10 μm in height. LatB fixing mix was then added and cantilever withdrawn. For cofilin measurements, networks were aged for 10 min then the cofilin premix was added. In the case of tropomyosin, the protein is added along with the fixing mix. Following fixing and aging, external force was applied in force clamp mode.

Rheology measurements: Rheology measurements were taken following fixing and aging of networks. For data acquisition, a force clamp of 5 nN magnitude was applied. Measurements were recorded for 45 min under the following conditions: rheology frequency = 2 Hz, rheology amplitude = 20 nm, sampling frequency = 1000 Hz, iterations = 2, and range = 500 mV.

Imaging and image analysis: Differential protein binding throughout the networks was followed in dual color experiments using a spinning disk confocal microscope (Yokogawa CSU10, Zeiss Observer Z1). 63x 1.4 N.A. oil objective (Zeiss) and a Photometrics Cascade II camera were additionally used in the system. For each measurement, a 45 min timelapse (3 min intervals) was acquired and z-stacks (1 μm frames) were recorded. Ratiometric distributions of ABP binding were measured at three different heights above the surface and averaged for each timepoint.

Supplemental Figures:

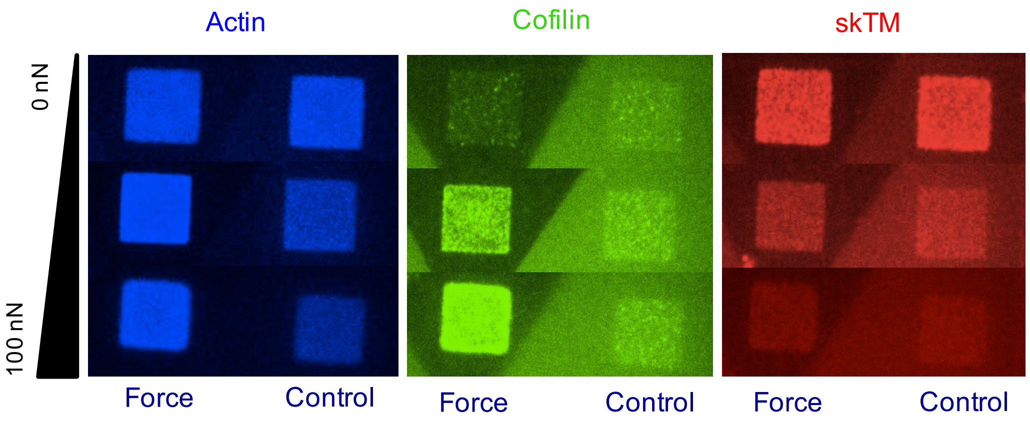

Supplemental Figure 1: Force alone can redistribute binding of cofilin and tropomyosin to actin structures
Planar views of actin, cofilin and skTM binding to branched actin structures grown under increasing levels of forces yet subject to the same biochemical conditions.

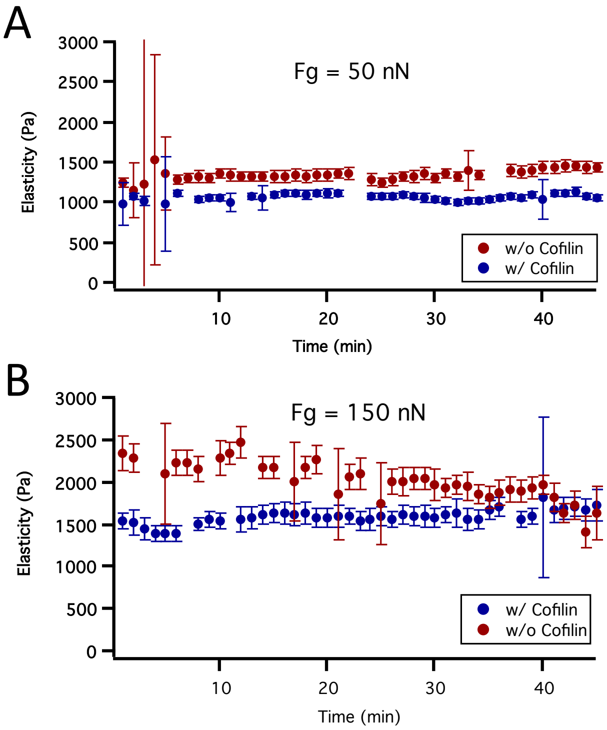

Supplemental Figure 2: Elasticity of actin networks is independent of growth force and cofilin binding
Variation in elasticity with time in presence and absence of cofilin for networks grown under Fg = 50nN (A) and Fg = 150 nN (B)

References:

1. Blanchoin L, Boujemaa-Paterski R, Sykes C, Plastino J. (2014). Actin dynamics, architecture, and mechanics in cell motility. Physiol Rev 94 (1): 235-63
2. Lin J.L. et al. (1988). Differential Localization of Tropomyosin Isoforms in Cultured Nonmuscle Cells. JCB 107: 563-572
3. Martin C and Gunning P (2008). Isoform Sorting of Tropomyosins. Tropomyosin, Landes Bioscience and Springer Science: Chapter 15
4. Bryce N.S. et al. (2003). Specification of Actin Filament Function and Molecular Composition by Tropomyosin Isoforms. Molecular Biology of the Cell 14: 1002-1016
5. McGough A et al. (1997). Cofilin Changes the Twist of F-Actin: Implications for Actin Filament Dynamics and Cellular Function. J Cell Bio. 138 (4): 771-81
6. Stokes et al. (1987). The Variable Twist of Actin and Its Modulation by Actin-Binding Proteins. Journal of Cell Biology 104, 1005-1017.
7. Ujfalusi Z. et al. (2012). Myosin and Tropomyosin Stabilize the Conformation of Formin-nucleated Actin Filaments. Journal of Biological Chemistry 287: 31894-31904
8. Gunning P, Schevzov G, Kee A, Hardeman E (2005). Tropomyosin Isoforms: divining rods for actin cytoskeleton function. Trends in Cell Biology 15 (6): 333 - 341
9. Michelot A and Drubin D (2011). Building Distinct Actin Filament Networks in a Common Cytoplasm. Current Biology 21: 560-569
10. Galkin V.E. et al. (2012). Actin Filaments as Tension Sensors. Current Biology 22, 96-101.
11. Finer J, Simmons R, and Spudich J (1994). Single myosin molecule mechanics: piconewton forces and nanometer steps. Nature 368: 113 - 119.
12. Ono S. and Ono K. (2002). Tropomyosin inhibits ADF/cofilin-dependent actin filament dynamics. Journal Cell Biology 156 (6): 1065-1078.
13. Bernstein B.W. and Bamburg J.R. (1982). Tropomyosin Binding to F-Actin Protects the F-Actin From Disassembly by Brain Actin-Depolymerizing Factor (ADF). Cell Motility 2:1-8.
14. Nishida E. et al. (1984). Cofilin, a Protein in Porcine Brain That Binds to Actin Filaments and Inhibits Their Interactions with Myosin and Tropomyosin. Biochemistry 23: 5307-5313.
15. McGough A. (1998). F-actin binding proteins. Current Opinion in Structural Biology 8: 166-176.
16. Prochniewicz E. et al. (2005). Cofilin Increases the Torsional Flexibility and Dynamics of Actin Filaments. J. Mol. Biol. 353:990-1000
17. Uyeda et al. (2011). Stretching Actin Filaments within Cells Enhances their Affinity for the Myosin II Motor Domain. Plos One 6 (10)
18. Bieling P, Li TD, Weichsel J, McGorty R, Jreij P, Huang B, Fletcher DA and Mullins RD. (2016) Force Feedback Controls Motor Activity and Mechanical Properties of Self-assembling Branched Actin Networks. Cell 164: 115-127
19. Carlier M.F. and Pantaloni D. (1986). Direct Evidence for ADP-Pi-F- Actin as the Major Intermediate in ATP-Actin Polymerization. Rate of Dissociation of Pi from Actin Filaments. Biochemistry 25: 7789- 7792

20. Andrianantoandro E and Pollard T (2006). Mechanism of Actin Filament Turnover by Severing and Nucleation at Different Concentrations of ADF/Cofilin. Molecular Cell 24: 13-23

Chapter 5

Cytoskeletal Stresses Revealed by Force Dependent Binding of Calponin Homology Domains to Actin

This chapter is in collaboration with Andrew Harris and Daniel A. Fletcher

Abstract:

The actin cytoskeleton of metazoan cells is organized by actin-binding proteins into distinct networks of actin filaments with diverse functions. Force transmission through these actin filament networks is central to their roles in cell movements and shape change. However, tracking actin cytoskeletal forces during dynamic cellular processes has not been possible due to the lack of appropriate measurement tools. Here we demonstrate force-dependent protein binding to actin structures and use it as a tool for mapping cytoskeletal stresses on actin filaments. We use the actin-binding domain of utrophin, a commonly used marker of actin filaments in live cells, to create a mutant utrophin whose affinity to filamentous actin scales with tension on the filament. We show that the mutant utrophin binds preferentially to filaments under tension in actin filament gels and single filaments in vitro. By comparing wild type and mutant utrophin binding in live cells, we are able to generate stress maps of actin cytoskeleton forces during cell spreading, blebbing and cytokinesis. Our findings suggest that filament tension may serve as a more general organizing principle for actin filament networks. The ratiometric actin filament force sensor reported here provides a new measurement tool for exploring mechanical regulation of actin-based cellular processes.

Introduction:

Actin filaments form an array of diverse structures that experience different forces during cellular processes including adhesion, division, and motility. Despite sharing a common cytoplasm, these actin structures maintain distinct identities characterized not only by the forces on them but also by the composition of actin binding proteins that organize them. While mapping these forces intracellularly has been challenging, two questions remain unanswered: 1) How do forces regulate actin structures? and 2) How are actin binding proteins directed to these structures.

Recent advances in electron microscopy have shifted the paradigm of actin filaments from a static structure to dynamic cytoskeletal constituent that can adopt various conformations (Galkin, 2012). This polymorphism is not only a result of mechanical perturbations that actin filaments are subject to but is also inherent and manifested under thermal fluctuations (Galkin, 2010). Furthermore, actin binding proteins have been shown to modulate structural properties of filaments upon binding (Ujfalusi, 2012; Hanein, 1997; McCullough, 2008). As a result, actin filaments are structurally diverse with angular twists ranging between 162^o and 170^o and persistence lengths as low as few microns and as high as 18 μm (Galkin, 2012; Chapter 1).

This diversity in structural states that filaments can adopt is relevant at the binding protein length scale and its impact can propagate to the micrometer length scale given the cooperative nature of various actin binding proteins (Michelot, 2011). In fact, correlations between the mechanical state of actin filaments and protein binding have been recently investigated (Jegou, 2016; Romet-Lemonne, 2013). Cofilin severing activity has been shown to decrease under tension whereas myosin binding increases (Hayakawa, 2011; Uyeda, 2011). Force has also been shown to regulate nucleation activity of Arp2/3 and formins. While filament curvatures biases Arp2/3 mediated branch formation, actin polymerization via formins is sensitive to tension as demonstrated in in-vitro and in-vivo assays (Risca, 2012; Higashida, 2013; Courtemanche, 2013).

Based on this preliminary evidence of correlation between stress state and ABP activity in addition to the structural diversity of actin filaments, we hypothesize that the mechanical state of actin filaments can regulate protein binding and, if so, it should be possible to develop an actin filament stress-sensor for mapping of intracellular and cytoskeletal forces. To do so, we examined the localization of actin binding domains within cells, and in response to changes in cytoskeletal tension. To rule out the role of signaling phenomena and cellular architecture, we modulated stress levels on actin gels and single filaments in in-vitro reconstituted assays using laser ablation and fluid shear flow. We then utilized this phenomenon to develop a binding protein probe that reads out the tensional state of an actin filament. To our knowledge, this probe provides the first affinity based read out of actin cytoskeletal tension and intracellular forces on actin filaments.

Results:

We chose to use the actin binding domain of utrophin (denoted as utrn) given its wide use as a generic marker for filamentous actin. This domain contains a type 1 and type 2 calponin homology (CH) domain in tandem (Keep, 1999). Tandem CH domains have 3 actin binding surfaces, two of these are exposed, one on the CH1 (actin binding surface 2, ABS2), one on the CH2 (actin binding surface 3, ABS3), and one that is buried at the inter domain interface (actin binding surface 1, ABS1). The main affinity for actin binding comes from the CH1 (Singh, 2014) with the CH2 thought to play a regulatory role (Galkin, 2010). Furthermore, CH domains have been reported to bind in either closed or open conformations (Chakravary, 2015), can bind filaments with different stoichiometries and with different affinities. Utrophin is reported to bind to actin by an induced fit mechanism (Moores, 2000; Lin, 2011), in an open conformation (Broderick, 2012; Galkin 2003) and with polymorphic stoichiometry (Galkin, 2002).

Calponin-homology domains are distributed non uniformly intracellularly

Given the reported flexibility and efficiency of utrn-ABD in binding filamentous actin (Winder, 1995), we used it as a negative control for localization studies of fluorescently tagged actin binding domains expressed in cells. We imaged the localization of GFP-utrn and Cherry-utrn as an initial test for co-localization. Utrophin ABD expressed in both color channels showed strong co-localization (Figure 1A). Utrophin Cherry also displayed resonable co-localization with lifeact-GFP another widely used f-actin marker (Supp Figure 1).

Interestingly, despite sequence homology, actin binding proteins of the calponin homology domains family localized non-uniformly to actin structures. While the tandem actin binding domain of smoothelin co-localized with utrophin, the domains of BPAG1 and filamin were segregated from the leading edge and mainly bound stress fibers at varying levels of affinities (Figure 1).

We next set to understand these patterns of differential localization. Since utrophin's actin binding domain binds in an open conformation to f-actin (Broderick, 2012) and shows ubiquitous cytoskeletal localization in cells, we postulated that open conformation tandem CH domains, or those with limited inter-domain interactions are stress insensitive. To test this, we introduced a mutation to the actin binding domain of filamin that opens the conformation of this ABD by disrupting an inter-domain salt bridge (Weins, 2007). Cherry-Filamin E254K co-localised GFP-utrophin whereas wild type filamin did not (Figure 1A,C). These results suggest that open-conformation calponin homology domains bind most of the actin structures within the cell with high affinity (Galkin, 2010).

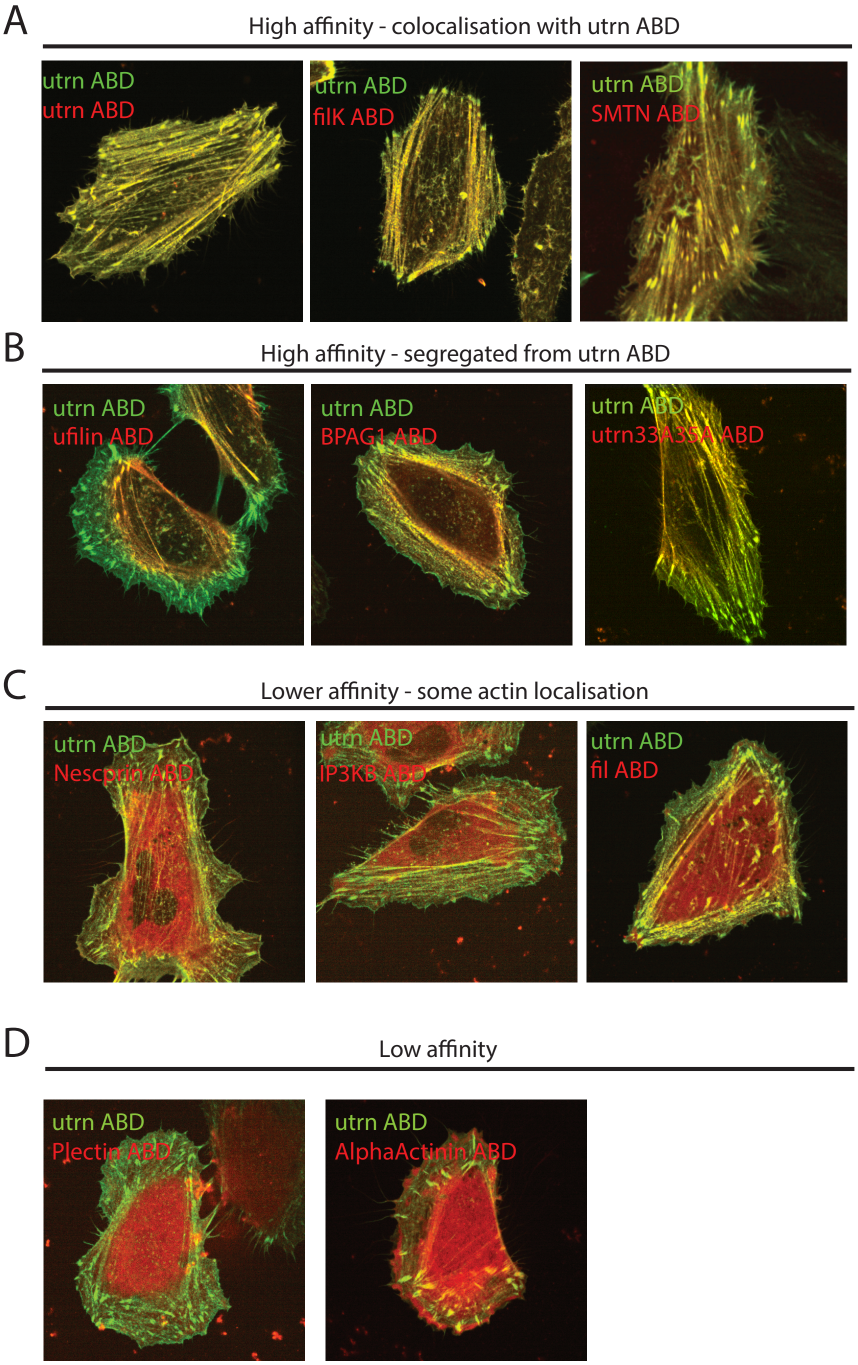

Figure 1: Differential localization of calponin homology domains in HeLa cells
Localization is determined relative to GFP-utrophin ABD and for tandem CH1-CH2 domains of calponin homology proteins. FilK is an open conformation mutant of filamin, Ufilin is a chimera of utrophin CH1, CH2 domains and filamin linker, utrn33A35A is a double alanine mutant of utrophin ABD.

The open conformation of utrophin's actin binding domain reveals all three actin binding surfaces to interface with F-actin. We performed domain analysis to investigate whether different actin binding surfaces were responsible for targeting to particular actin structures. We expressed both the isolated CH1 domain (containing ABS1 and ABS2) and isolated CH2 domain (containing ABS3) to examine their role in actin binding. Cherry-CH2 was largely cytoplasmic, consistent with the notion that it plays a regulatory role, rather than contributing high affinity actin binding (Supplemental Figure 1). In contrast, Cherry-CH1 showed strong segregation from the WT utrn and localized to stress fibers, consistent with previously reported findings for the localization of truncated utrophin constructs (Supplemental Figure 1; Belin, 2015). Meanwhile, previous studies have shown that the isolated CH1 domain has reduced solubility in comparison to the full tandem domain (Singh, 2014). To make subtle changes to the actin binding capability of the different actin binding surfaces without affecting the solubility of the protein, we employed a targeted mutagenesis strategy. We found that a double alanine substitution to ABS1 (utrn 33A 35A) caused the actin binding domain to segregate from the localization of the wild type domain whilst retaining high affinity (Figure 1B). This was also observed with a chimera of the filamin linker region and utrophin actin binding domains.

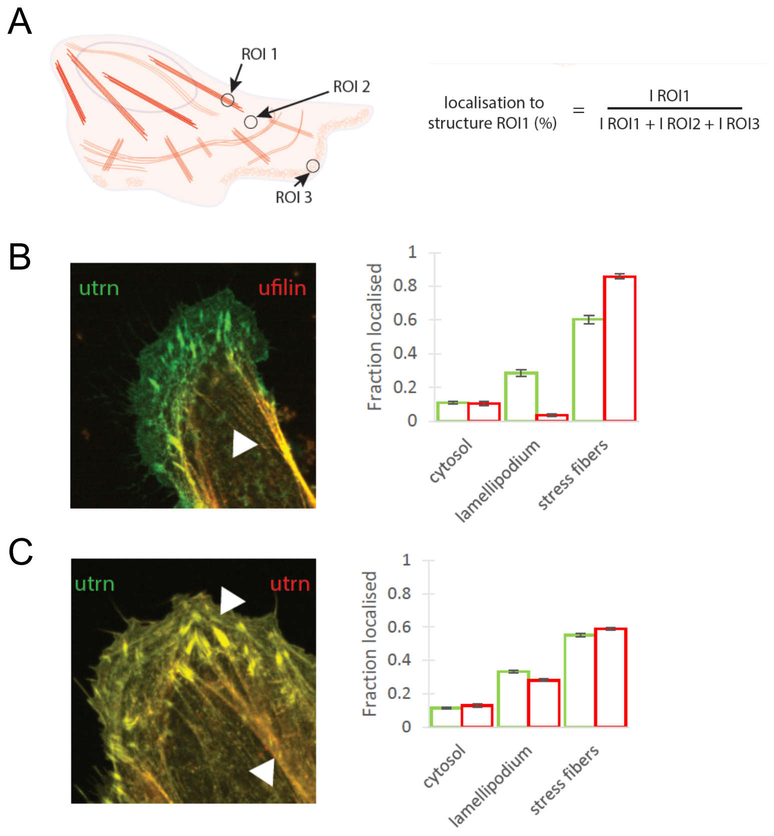

Figure 2: Preferential binding of ufilin to stress fibers A: Schematic representation and formulation of protein binding quantification on stress fibers, lamellipodial structures and cytoplasm, B: Fractions of ufilin localization to various actin structures, C: Control measurements of co-localization of GFP and Cherry utrophin (Error bars are SE)

Interestingly, the structure of tandem calponin homology domains between proteins are highly conserved, with the highest sequence heterogeneity arising in the linker region between the two domains (Bandi, 2015). To test the role of the linker region between the domains we created a chimera of the filamin linker region between the tandem calponin homology domains of utrophin. This chimera, which we refer to as ‘ufilin’, localized to actin bundles within the cell and showed near complete exclusion from lamellipodial like ruffles (Figure 1B). To clarify this preferential localization to stressed actin structures, we expressed equal amounts of utrophin and ufilin in HeLa cells and quantified the distribution of protein throughout the cell. Ufilin in these cells was completely segregated onto the stress fibers of HeLa cells and was almost completely absent from ruffling edges (Figure 2). The localization of ufilin in cells therefore resembles local increases in mechanical stress on the actin cytoskeleton.

In sum, despite sequence homology, calponin homology domains bind to different actin structures characterized by distinct mechanical profiles. While being widely used as an actin marker, subtle changes to utrophin’s actin binding domain can redirect its localization intracellularly. This behavior was significantly manifested with ufilin, a mutated version of utrophin where the linker between the CH1 and CH2 domains was swapped with the filamin linker. With binding profiles that coincides with intracellular tension, we next focus our study on ufilin and hypothesize that it is sensitive to the mechanical state of the filaments and can be leveraged as a tool for tracking and mapping intracellular tension.

Differential binding of ufilin depends only on actin filament stresses

To test whether localization of ufilin was a result of protein sensitivity to actin filament stress alone rather than a signaling phenomena, we developed in vitro assays with minimal constituents and controlled biochemical conditions. We formed actin gels of different levels of network pre-stress by kinetically trapping polymerizing filaments with the actin crosslinker α-actinin (Supp Figure 2; Jensen, 2015).

Under conditions of high concentration of actin monomer (12 μM actin) and α-actinin (2.4 μM), rapid polymerization and crosslinking rates generated stresses in filaments within the gel resulting in an overall internal pre-stress. To create local heterogeneities in pre-stressed actin gels, we locally ablated networks using a piezo-steered nitrogen laser. Post-ablation, the network was destroyed with only a few filament fragments remaining in the ablated region. Within 5 minutes, an actin network reformed in the ablated region under lower levels of prestress (Supp Figure 3). This generated mechanical heterogeneity between the ablation region and surrounding intact structures. The localization of ufilin was then measured in comparison to wild type utrophin as a function of radial distance from the center of the ablation site (Figure 3C). The system was void of any other binding and regulatory proteins allowing us to directly probe the role of actin stress in directing protein localization.

We found that gels that contained utrophin-647 and utrophin-555 as a control did not show ratiometric differences in binding to the reforming actin network (Figure 3E). However, gels containing ufilin (Figure 3D) showed lower ratiometric binding in the ablated region. To further test the role of the amount of pre-stress on the ratiometric binding, we created gels using lower concentrations of α-actinin (600nM), which kinetically trap polymerizing filaments less efficiently and carry a lower intrinsic pre-stress (Schmoller, 2008). Post-ablation, these gels did not show significant differential binding of ufilin relative to utrophin (Figure 3F), reinforcing the notion of its stress dependent segregation.

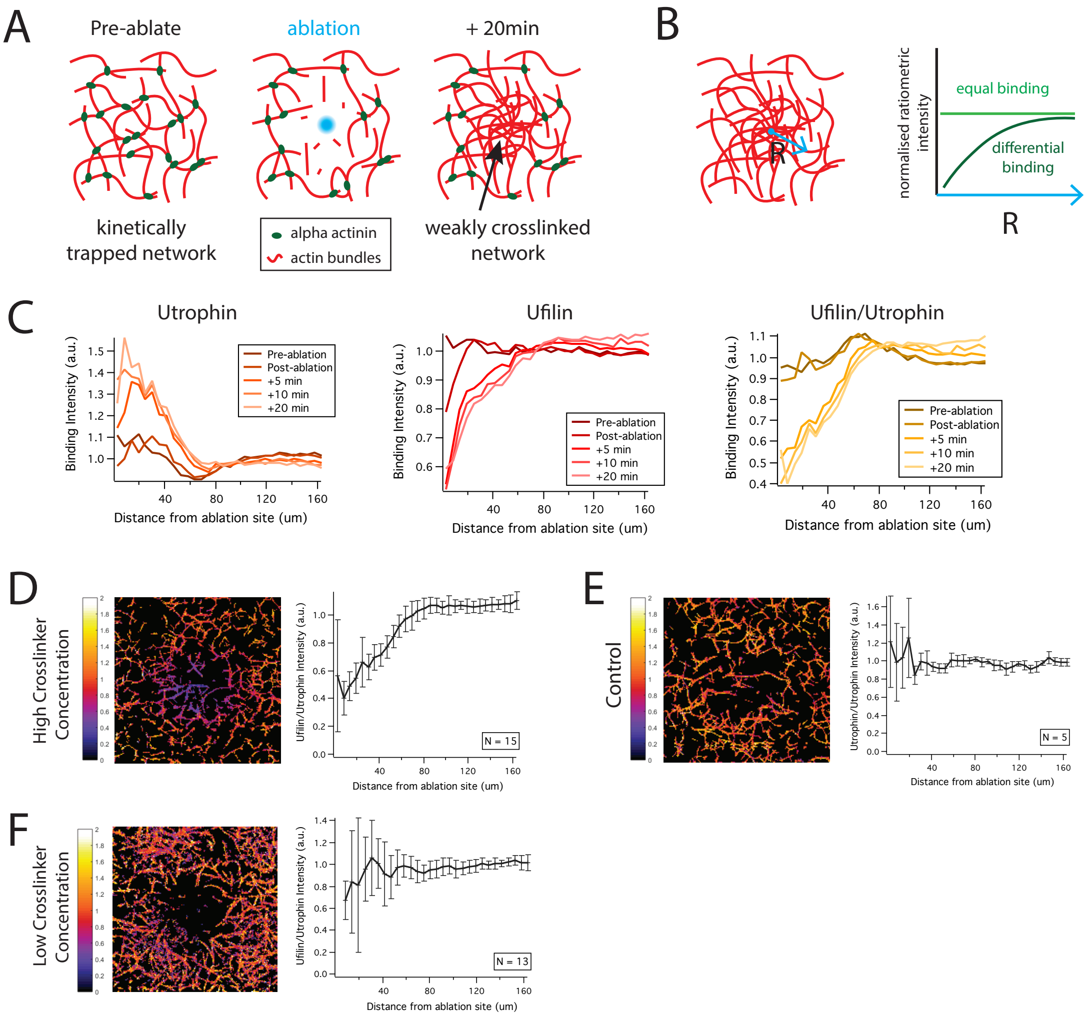

Figure 3: Ufilin distribution in mechanically heterogeneous actin gels
A: Schematic representation of the laser ablation experimental setup, B: Predicted protein binding profiles as a function of radial distance from the ablation site, C: Distribution of utrophin, ufilin and ratiometric binding away from the ablation site in kinetically trapped networks with high crosslinker concentration (2.5 μM), D-F: Ratiometric intensities of ufilin/utrophin binding under (D) high crosslinking conditions (2.5 μM actinin, 647-utrophin, 555-ufilin), (E) control conditions (2.5 μM actinin, 647-utrophin, 555-utrophin), (F) low crosslinking conditions (600 nM actinin, 647-utrophin, 555-ufilin).

Differential binding of ufilin is a function of tension in actin filaments

We developed a single filament in vitro assay to implicitly test whether the binding affinity of ufilin is a function of the level of stress in actin filaments (Jegou, 2016). Here, single actin filaments were suspended between pairs of 200 nm functionalized beads which act as discrete tethering points on the surface of a glass flow chamber. A transient fluid flow into the chamber served to pin filaments between beads at different forces arising from the fluid shear stress. A range of forces were hence generated and depended on the inter-bead distance and fluid flow rate. We roughly estimate the maximum extensional force exerted on an actin filament in the chamber to be ~10 pN at 200 nm above the surface of the coverslip.

In order to estimate the stress level on an individual filament, we used filament thermal fluctuation as a precursor for tension. To visualize fluctuating filaments, WT utrophin was used as a reference channel in all experiments. Using time lapse imaging of filament fluctuations, we were able to collect fluctuation envelopes of filaments from the average and maximum intensity projections of the image stack through time. The brightness in the average intensity projection represents the average amount of time that a given filament spends in the focal plane.

Out of focus fluctuations contribute low intensity frames whereas those in focus contribute bright intensity data. Therefore, a filament that is loosely bound between beads has more low intensity frames contributed to its average intensity projection as it has a higher density of fluctuation states out of the focal plane. On the other hand, filaments that are highly tensed do not fluctuate out of the focal plane and hence have an average intensity projection that is bright, and largely correlates with the maximum intensity that the filament contributes when perfectly in focus. In order to characterize the extent of these fluctuations, we defined the “stretch state” metric. The later corresponds to the ratio of average intensity projection to maximum intensity projections in the WT utrophin channel. Hence, the higher the stretch state value and closer to unity, the more tensed is the filament whereas lower stretch state values indicate higher degrees of fluctuation (Supp Figure 4).

To test for mechanosensitive binding, we introduced ufilin in the shear flow assay along with utrophin. Fluorescence measurements were dual color and imaged as a function of time. Average intensity projections in the ufilin channel contained information about the force on the filament as well as the amount of bound protein. We used the fluctuation spectrum from the WT utrophin channel to normalize out the changes in intensity that result from the fluctuations of the filament. This yielded an unbiased measure of protein binding on the filament.

We tested the validity of the system by introducing predefined amounts of labelled actin monomers into the filaments and used the same approach to measure the fluorescence in the actin channel as we would have for the binding protein (Figure 4C). The fluorescent signal scaled with the molar amount of fluorescent monomers that were incorporated into the filaments, but did not show scaling with stretch state of filaments (Figure 4D). Additionally, when WT utrophin was used in both the reference and binding protein channels, no scaling was observed. In contrast, the binding of ufilin scaled with stretch state linearly (Figure 4E). This effect was consistent under various concentrations of ufilin (Supp Figure 6). These observations support our hypothesis that ufilin is a force sensor and preferentially binds to stressed actin filaments.

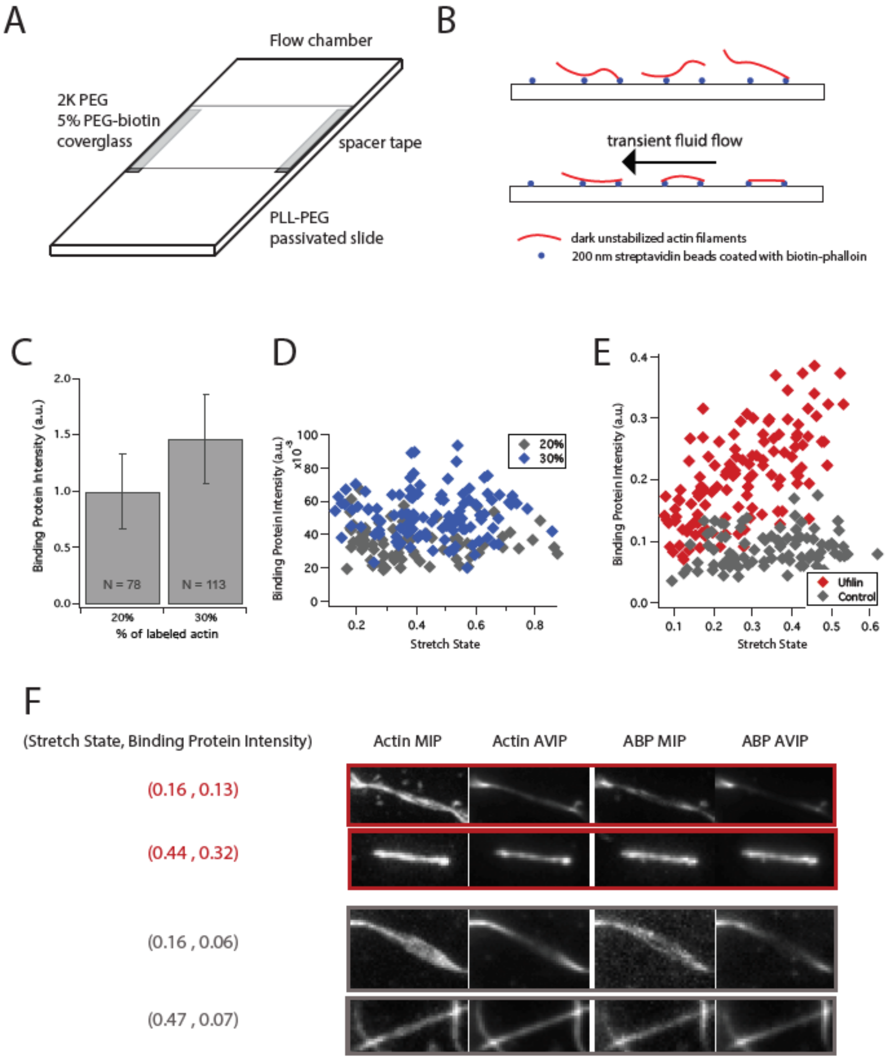

Figure 4: Mechanical perturbations to single actin filaments via shear flow
A-B: Experimental setup of flow chamber and tethered single filaments to 200 nm surface bound beads, C: Measured fluorescence intensity of actin with labeled monomers as proxy for binding proteins and using our analysis algorithm, D: Labeled actin intensity variation as a function of stretch state, E: Stretch state dependency of ufilin and utrophin (control) binding, F: MIP and AVIP in binding protein and actin channels for sample filaments, binding protein is ufilin for upper red panels and utrophin for lower grey panels.

Force sensor is a tool for mapping cytoskeletal stresses during cellular processes

As a force sensor, ufilin presents a significant potential for reading out and mapping tension intracellularly. To further investigate the applicability of this probe in-vivo, we tested its localization during various biological processes for which we predict heterogeneity in the mechanical state of the cytoskeleton.

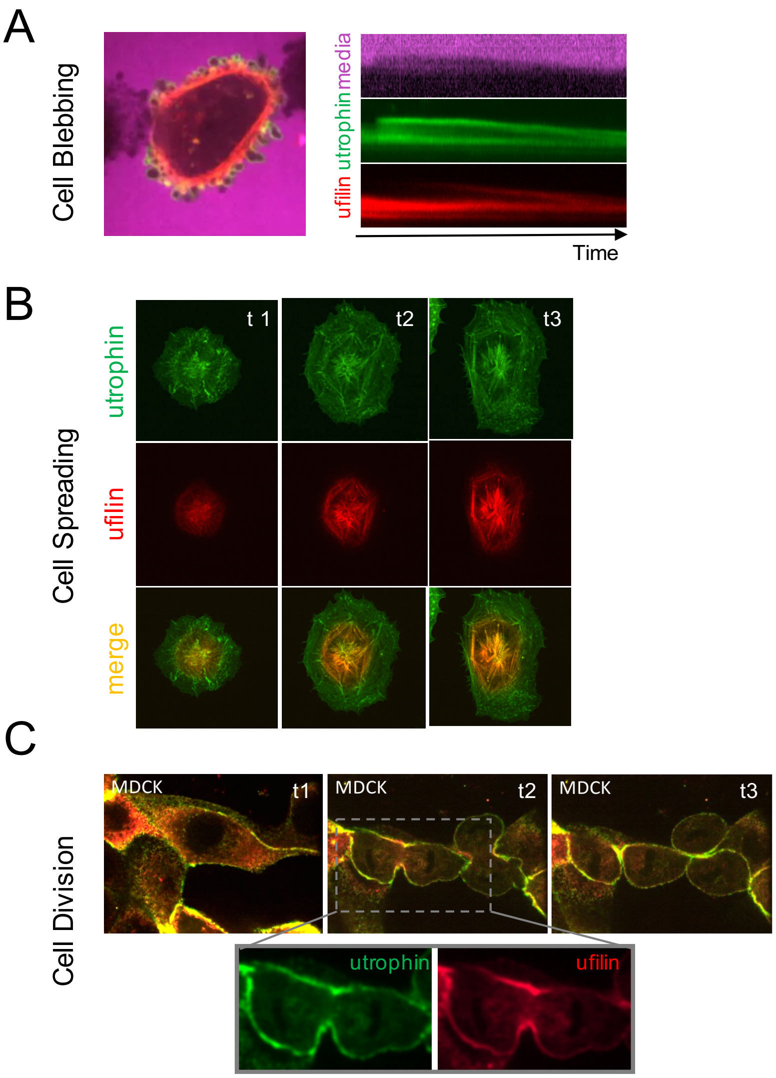

Figure 5: Physiological applications of stress mapping using ufilin
A: Recruitment of ufilin upon inward contraction of blebs in U2OS cells plated on glass surfaces, B: Spatiotemporal binding of ufilin during cell spreading and actin bundle formation in HeLa cells, C: Concentration of ufilin at the cleavage furrow during cell division of MDCK.

During blebbing, the actin cytoskeleton is dynamically remodeled. Initial bleb formation is characterized by low levels of tension and marked by the recruitment of ezrin followed by actin. Subsequently, stress buildup and inward contraction occur upon recruitment of myosin (Fackler, 2008; Charras, 2006/8). We postulated that the recruitment of ufilin will occur during bleb contraction. To test this hypothesis, we imaged bleb formation of U2OS cells plated on glass surface and co-expressed GFP-utrophin and Cherry-ufilin. Utrophin was used as an actin marker and allowed us to track actin recruitment to the bleb. Interestingly, kymographs of utrophin and ufilin recruitment to the blebs showed a delayed buildup of ufilin relative to utrophin. We see that ufilin is recruited at later time points and is more pronounced in the contraction phase of the bleb rather than the initial formation (Figure 5A).

Another critical biological phenomena characterized by distinct spatiotemporal mechanical profiles of cytoskeleton is cell spreading. In fact, during spreading, cells undergo a transition from non-contractile ruffling to contractile tugging and polarization on the surface as cytoskeletal structures such as stress fibers are established (Gauthier, 2011). We followed localization of utrophin and ufilin intracellularly during spreading. To do so, we imaged cell lines expressing both GFP-utrn and Cherry-ufilin over a 2 hour time course. During the first hour, large ruffles could be seen at the cell edge that correspond to lamellepodial based cell spreading. Interestingly, these ruffles were rich in utrophin but did not contain ufilin. It is only after 1 hour of spreading when stress fibers were forming and exerting stresses on the substrate that ufilin recruitment was observed (Figure 5B).

We lastly thought to investigate the recruitment of ufilin during cell division. In fact, one of the most striking cellular processes that requires force is the formation of contractile ring and its tightening during cytokinesis (Miller, 2011). To investigate ufilin localization during division, we imaged MDCK cells over long time periods and co-expressed GFP-utrophin and Cherry-ufilin. While we observed no major difference in localization of utrophin and ufilin prior to cell division, recruitment of ufilin was significantly pronounced at the cleavage furrow as the cells started dividing (Figure 5C). Together these measurements further support a model whereby ufilin binding to actin structures is mechanosensitive; a property that can be leveraged for tracking forces in-vivo.

Discussion:

Using a minimal actin binding domain based on utrophin's tandem CH1-CH2 domains, we have demonstrated that force alone can bias protein binding to actin structures. While understanding the mechanism of this mechanosensitive response is challenging, elucidating how force impact the structural state of actin filaments and how that effect translates to the binding protein remains crucial.

In fact, our understanding of the physical properties of actin filaments is limited to the micrometer length scale and its characteristic fluctuation spectrum. Meanwhile, much smaller length scales are relevant for the actin binding proteins. Advances in modeling techniques and imaging approaches will be needed to understand how force application impact filament fluctuations and further correlates with variability in twist.

While our findings here are based on ufilin, a synthetic protein, we expect this sensitivity to the mechanical state of actin filaments to hold for physiological proteins as well. In fact, as seen in Fig 1, various native calponin homology domains including BPAG1 and filamin are also spatially segregated and mainly bind to stress fibers. Additionally, several proteins including cofilin, tropomyosin and myosin have been shown to induce changes in the filament twist upon binding. This effect is observed with nucleators as well (e.g. formin) and toxins (e.g. phalloidin). Hence, this preferential binding to a stress state of actin can not only lead to differential ABP localization in the cytoskeleton, but also mediate cooperative binding of other proteins as well as regulate biological activity.

Lastly, as a force sensor, ufilin binding to actin filaments in response to tension is linear. Hence, it can be employed as a versatile molecular tool for detecting and mapping various levels of cytoskeletal stresses in vitro. Additionally, it can be used as a reference for investigating the mechanosensitive binding of other binding proteins using co-localization profiles. Exploring the role of mechanics could further shed light on the regulation of various actin structures in addition to their assembly and disassembly mechanisms.

Methods:

Cell Culture and generation of constructs: HeLa cells were cultured at 37 °C in an atmosphere of 5% CO_2 in air in DMEM (Life Tech, #10566024) supplemented with 10% FBS (Life Tech, #16140071) and 1% Penicillin-Streptomycin (Life Tech, #15140122). Live imaging experiments were performed in normal cell culture media using an OKO labs microscope stage enclosure.

To visualize the localization of different constructs with respect two wild type utrophin 261, dual expression plasmids were generated. GFP-UtrCH was a gift from William Bement (Addgene plasmid # 26737). For dual expression a 2a clevable peptide was introduced to the c terminus of GFP-UtrCH followed by cherry fused to the actin binding domain of interest using Gibson assembly of the respective inserts. In all cases the linker region between the constructs and their respective fusion proteins were kept consistent. For imaging experiments HeLa cells were plated onto fibronectin coated glass bottomed wells (Life Tech, #33016015) transfected using effectene (Qiagen, #301425) and imaged 24 hours after transfection.

For generating stable cell lines GFP-UtrCH and the construct of interest were cloned separately into the Lentiviral plasmid PHR. Lentiviruses were then generated by transfecting the plasmids into HEK cells for packaging. Retroviral supernatants were then used to infect HeLa cells.

Cellular confocal imaging: Fluorescent proteins were imaged using the following excitation and emission: GFP was excited at 488 nm and emission was collected at 525 nm, mCherry was excited at 543 nm, and emission was collected at 617 nm.

Protein purification and labeling: Actin was purified from rabbit muscle acetone powder (Pel Freez Biologicals, #41995-1) according to Spudich & Watt, 1971. Alexa-488 dye (Life Technologies, #A10254) was conjugated to purified actin using maleimide chemistry at Cys 374. Both unlabelled and Alexa-488 actin were stored in monomeric form in G-buffer (2mM Tris-Cl pH 8.0, 0.2 mM ATP, 0.5 mM TCEP, 0.1 mM $CaCl_2$) at 4deg.

Utrophin ABD and Ufilin were expressed recombinantly in E. coli BL21 (DE3) pLysS (Promega, #L1191) and purified using affinity chromatography followed by gel filtration. Proteins were stored in 20 mM Tris-Cl pH 7.5, 150 mM KCL, 0.5 mM TCEP and 0.1 mM EDTA and in the presence of 20% glycerol. Utrophin ABD and Ufilin sequences included a KCK linker (GGSGKCKSA) on the C terminus. Both proteins were labeled using Alexa 647 and Alexa 555 maleimide dye (Life Technologies, #A22287 &

#A20346) at the single cysteine site in the linker region. Acanthamoeba α-actinin was a kind gift from Peter Bieling.

Surface functionalization and flow well assembly: Crosslinked network and single filament assays were performed in a flow well configuration consisting of a functionalized coverslip and passivated counter-surface assembled using Tesa double sided tape. 3''X1''X1mm glass slides (VWR, #48300-047) were first cleaned in 1% micro-90, rinsed twice in miliQ, plasma cleaned then passivated using PLL-PEG. PLL-PEG (g = 3.5) was prepared as described in Bieling et al 2010. 22x22mm coverslips (Zeiss, #474030-9020-000) were passivated using PEG-silane chemistry (Bieling, 2010). Briefly, PEG coupling to the silanized surface was achieved by preparing a PEG saturated acetone solution at 95% hydroxy-amino-PEG (Rapp Polymere, #10 3000-20) and 5% biotinyl-amino-PEG (Rapp Polymere, #13 3000-25-20).

Crosslinked actin network assays:

- Oxygen Scavengers Premix: Oxygen scavengers were introduced in all assays to minimize photobleaching and filament breakage. A 10x premix was prepared fresh with each experiment and consisted of 2 mg/ml glucose oxidase (Sigma, #G-2133), 0.35 mg/ml catalase (Sigma, #C-40), 45 mg/ml glucose (Sigma) in 80 mM PIPES (pH 6.8), 1 mM $MgCl_2$, 1mM EGTA (Kueh et al., 2008).

- Assay: All reagents including monomeric actin, crosslinker, binding proteins and oxygen scavengers were added in presence of G-buffer. 1x KMEI was then used to trigger polymerization and network formation. Although, network formed in valap-sealed chambers instantaneously, each sample was given 5 min to equilibrate prior to imaging. Actin and binding proteins were used at final concentrations of 12 μM and 200 nM respectively. Highly crosslinked networks were generated using 2.5 μM α-actinin. This concentration was set at 600 nM for low crosslinking regimes. In order to age networks, samples were left for 3 hrs at room temperature following polymerization.

- Network assay Imaging: For the network assays, cross-linked actin structures were imaged using a spinning disk confocal microscope (Yokogawa CSU10, Zeiss Observer Z1, Cobolt Jive 561nm laser, Coherent OBIS 640nm laser), a 63x 1.4 N.A. oil objective (Zeiss, Plan-Apochromat) and an EMCCD camera (Photometrics Technology). Micromanager V. 1.4.21 was used for image acquisition. A 3x3 grid was initially imaged for each sample. The center field of view was then ablated using a 488 SRS NL100 laser attached to a micropoint galvo steering system. Laser transmission intensity and number of pulses were controlled such that the ablation site covered ~ 75% of field of view. Binding of proteins within the 3x3 grid was monitored at different time points (t = 0, 5, 10, 20 min post ablation).

Single filament assay:

- Beads Functionalization: 200 nm blue carboxylate modified fluoSpheres beads (ThermoFisher, #F8805) were functionalized with streptavidin (Life Technologies, S888). Streptavidin was covalently linked to the carboxyl group of beads via EDAC activation following manufacturer's protocol (Molecular Probes, 2004, Working with FluoSpheres Fluorescent Microspheres). Functionalized beads were stored at a final concentration of 2.5 mg/mL in PBS at 4deg.

- Actin Polymerization: Actin filaments were polymerized at a final concentration of 1 µM at RT and in presence of 1X KMEI (50 mM KCl, 1 mM $MgCl_2$, 1 mM EGTA, 10 mM Imidazole pH 7.0). Polymerized filaments were prepared fresh prior to experiments, left unstabilized and stored at 4deg.

- Assay: Functionalized streptavidin beads were diluted in 20 mM HEPES (pH 7.0) at a final concentration of 150 µg/mL, vortexed then sonicated for 10 min. The solution was then spun at 12 000 rpm for 1 min at RT in order to remove any remaining aggregated beads. The supernatant was incubated in the flow-well chamber for 10 min. To wash unbound beads to biotin-PEGylated surface, excess 20 mM HEPES (pH 7.0) was used. Next, biotin-phalloidin (Life Technologies, #B7474) at 100nM in 20 mM HEPES was incubated in chamber for 5 min, generating anchoring sites for actin filaments. Excess biotin-phalloidin was washed using 20 mM HEPES containing b-casein (Sigma, #C6905) at 100 µg/mL. Polymerized actin filaments were incubated for 10 min in presence of F-buffer containing b-casein. Finally, the protein mix containing binding protein of interest, oxygen scavengers and b-casein in protein buffer (20 mM HEPES pH 7.0, 100 mM KCl) was flown into the chamber. This final flow step served two purposes: introducing actin binding protein of interest and applying a range of forces to surface anchored filaments.

- Single filament assay imaging: For the single filament assays, semi-TIRF imaging approach was used to capture filament fluctuations and protein binding at a high signal/noise ratio (Tokunaga et al, 2008). The imaging system consisted of a Nikon TIRF inverted scope (Nikon Eclipse Ti, 488/560/642nm OPSL lasers) with perfect focus, a 60x N.A. 1.4 APO TIRF oil objective, and an EMCCD camera (Andor iXon Ultra). For each filament, a 30 frame time-lapse was recorded using Micromanager 1.4.23 acquiring each color channel with 100ms exposure.

- Fluctuations and Binding Intensity Analysis: A Matlab routine was implemented to assess extent of filament fluctuations and measure protein binding intensity. The user was initially prompted to manually crop a filament region for subsequent analysis. The routine looped over all timepoints and calculated maximum intensity projections (MIP) and average intensity projections (AVIP) in actin and binding protein channel. Filament length and width were determined based on user-defined point locations.

  In order to assess the extent of fluctuations, a metric for the tension state of the filament was defined as Stretch State and consisted of the mean value of the ratiometric AVIP/MIP image based on intensities measured in the actin channel.

Higher Stretch State values (i.e. closer to unit value) indicated a tensed filament. In order to accurately measure protein binding, out of plane fluctuations were corrected for by normalizing all values to the ratiometric AVIP/MIP image as determined in the actin channel. The resulting calculated value of protein binding intensity consisted of the mean value of fluctuation-normalized AVIP in the protein channel. The half circumference of an ellipse for which the major axis are the filament length and width of fluctuation envelope was calculated to approximate the contour length value.

Supplemental Figures:

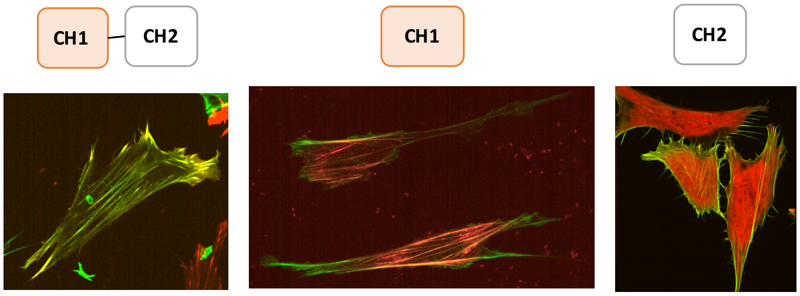

Supplemental Figure 1: Varying affinities of utrophin's isolated CH domains to actin
Co-expression in 3T3 cells of GFP-lifeact with from left to right Cherry-utrophin tandem domains, Cherry-utrophin CH1 domain and Cherry-utrophin CH2 domain

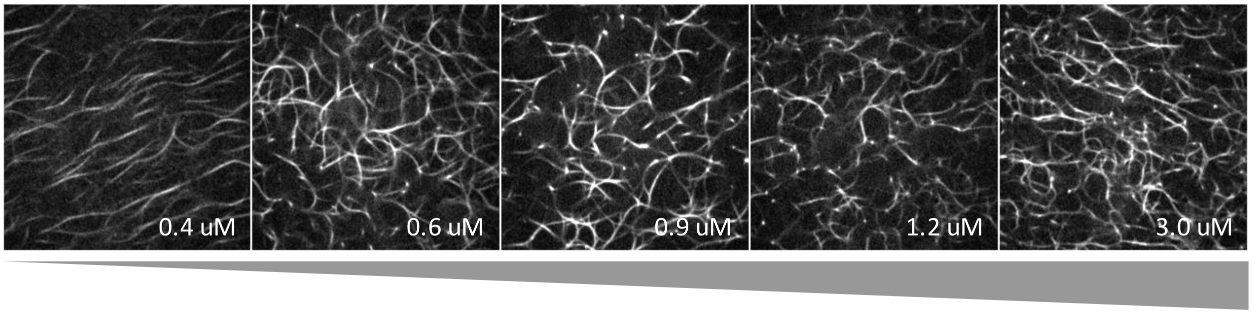

Supplemental Figure 2: Kinetic trapping of actin structures via crosslinker activity
From left to right, increase in mesh density and prestress with increasing concentration of crosslinker in polymerizing actin gels.

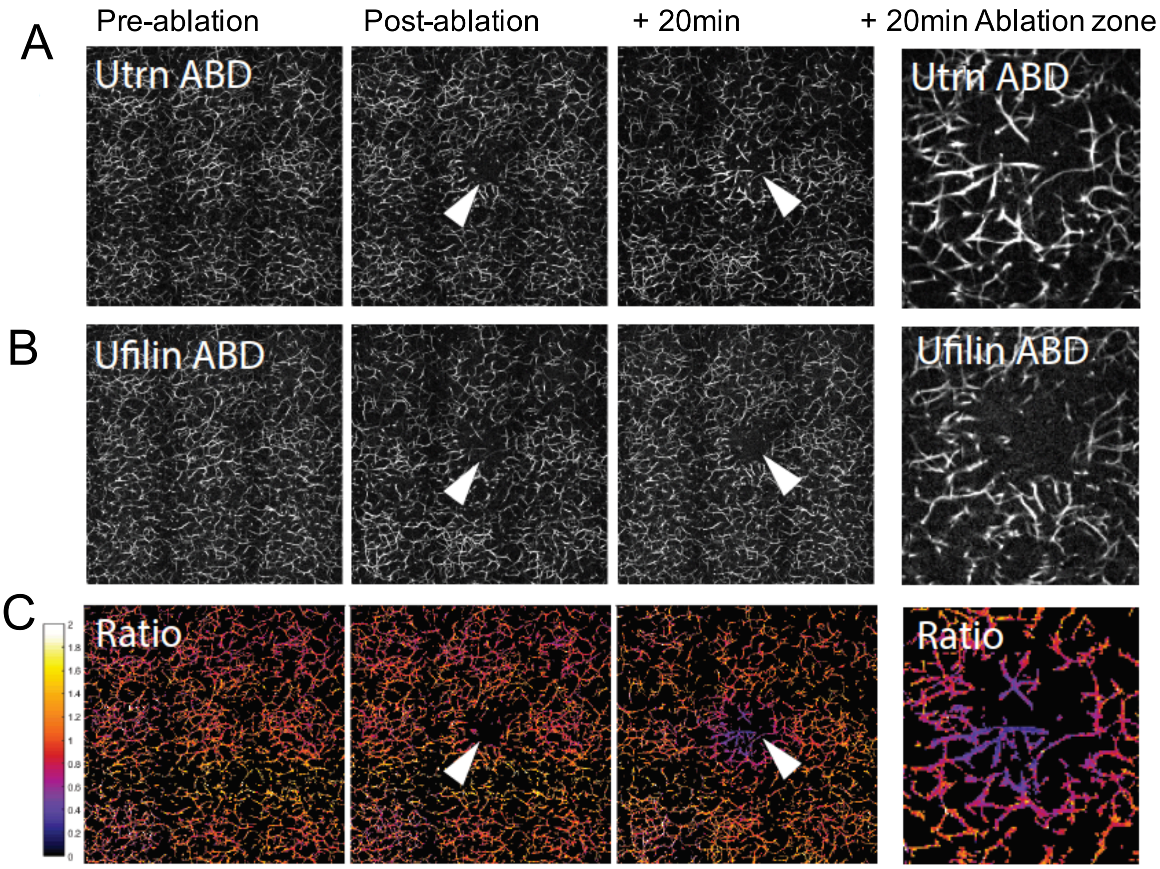

Supplemental Figure 3: Evolution of ablation spots with time in kinetically trapped actin gels Images were acquired before ablation, at t = 0^+ and t = 20 min in the utrophin channel (A) and ufilin channel (B).

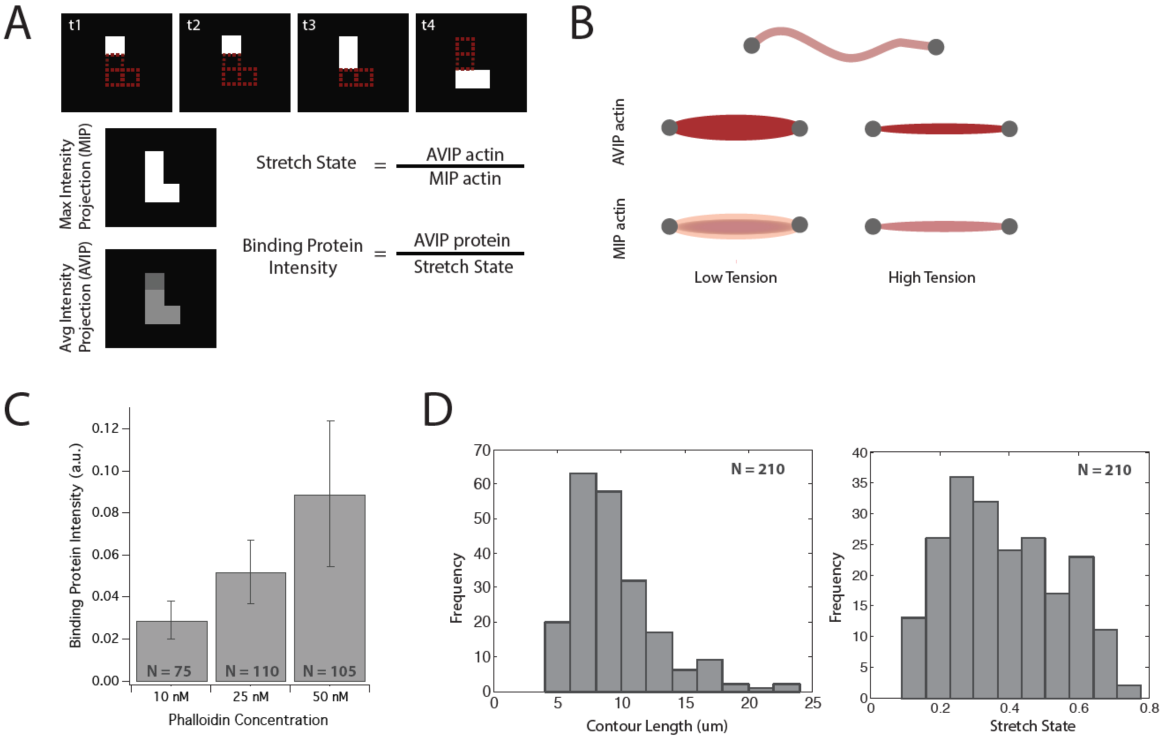

Supplemental Figure 4: Analysis of protein binding intensities in single filament experiments A-B: Estimations of stretch states and binding protein intensities using AVIP and MIP measurements, C: Calibration of analysis routine using different concentrations of phalloidin, D: Sample contour lengths and stretch states distribution in a flow well chamber

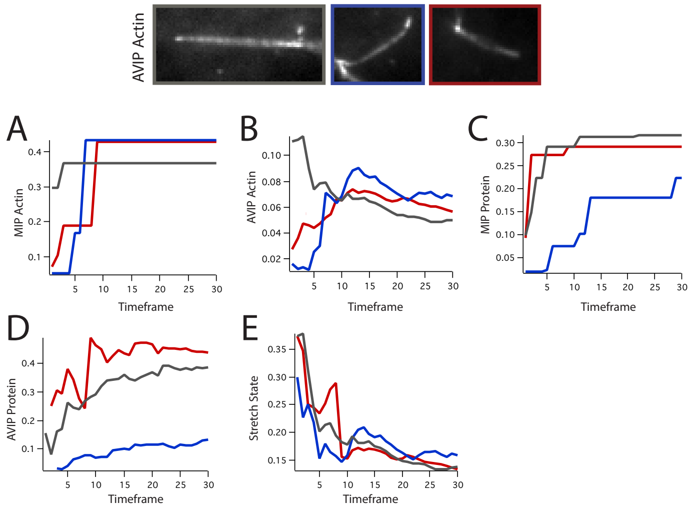

Supplemental Figure 5: Convergence of analysis parameters over acquisition time course Three sample filaments and convergence of their characteristic MIP actin (A), AVIP actin (B), MIP protein (C), AVIP protein (D) and stretch state (E) over the 30 timeframe acquisition.

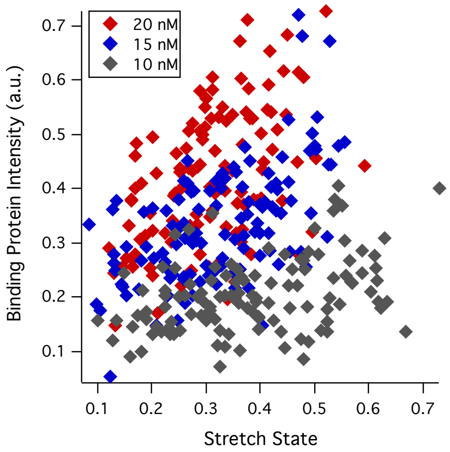

Supplemental Figure 6: Increase of ufilin bias in binding to stretched filaments at higher soluble protein concentrations

References:

1. Galkin V, Orlova A, and Egelman E (2012) Actin Filaments as Tension Sensors. Current Biology 22: 96-101
2. Galkin V, Orlova A, Schroder G, and Egelman E. (2010) Structural Polymorphism in F-actin. Nature Structural and Molecular Biology 17 (11): 1318 - 1324
3. McCullough B.R. et al. (2008). Cofilin Increases the Bending Flexibility of Actin Filaments: Implications for Severing and Cell Mechanics. JMB 381 (3): 550-558
4. Hanein et al. (1997). Evidence for a Conformational Change in Actin Induced by Fimbrin (N375) Binding. Journal of Cell Biology 139, 387-396
5. Ujfalusi Z et al. (2012). Myosin and Tropomyosin Stabilize the Conformation of Formin-nucleated Actin Filaments. Journal of Biological Chemistry 287: 31894-31904
6. Hayakawa et al. (2011). Actin filaments function as a tension sensor by tension-dependent binding of cofilin to the filament. Journal of Cell Biology 195, 721-727
7. Uyeda et al. (2011). Stretching Actin Filaments within Cells Enhances their Affinity for the Myosin II Motor Domain. Plos One 6 (10)
8. Risca et al. (2012). Actin Filament Curvature Biases Branching Direction. PNAS 109, 2913-2918.
9. Higashida et al. (2013). F- and G-actin homeostasis regulates mechanosensitive actin nucleation by formins. Nature Cell Bio 15: 395-405
10. Courtemanche N, Lee J, Pollard TD, Greene EC (2013). Tension modulates actin filament polymerization mediated by formin and profilin. PNAS 110 (24): 9752-9757
11. Michelot A and Drubin D (2011). Building Distinct Actin Filament Networks in a Common Cytoplasm. Current Biology 21: 560-569
12. Jegou A and Romet-Lemonne G (2016). Single Filaments to Reveal the Multiple Flavors of Actin. Biophysical Journal 110: 2138-2146
13. Romet-Lemonne G and Jegou A (2013). Mechanotranduction down to individual actin filaments. European Journal of Cell Biology 92: 333-338
14. Bandi S, Singh S and Mallela M (2015). Interdomain Linker Determines Primarily the Structural Stability of Dystrophin and Utrophin Tandem Calponin-Homology Domains Rather than Their Actin-Binding Affinity. Biochemistry 54: 5480-5488
15. Chakravarty D, Chakrabrti S and Chakabarti P (2015). Flexibility in the N-terminal actin binding domain: Clues from in silico mutations and molecular dynamics. Proteins: 696-710
16. Galkin V, Orlova A, Vanloock M, Rybakova I, Ervasti J and Egelman E (2002). The utrophin actin-binding domain binds F-actin in two different modes: implications or the spectrin superfamily of proteins. JCB 157 (2): 243-251
17. Galkin V, Orlova A, Salmazo A, Djinovic-Carugo K and Egelman E (2010). Opening of tandem calponin homology domains regulates their affinity for F-actin. Nature Structural and Molecular Biology 17 (5): 614-616
18. Lin A, Prochniewicz E, James Z, Svensson B and Thomas D (2011). Large-scale openining of utrophin’s tandem calponin homology (CH) domains upon actin binding by an induced-fit mechanism. PNAS 108 (31): 12729-12733

19. Moores C, Keep N and Kendrick-Jones J (2000). Structure of the Utrophin Actin binding Domain Bound to F-actin Reveals Binding by an Induced Fit Mechanism. J. Mol. Bio. 297: 465-480
20. Singh S, Bandi S, Winder S and Mallela K (2014). The Actin Binding Affinity of the Utrophin Tandem Calponin Homology Domain is Primarily Determined by its N-Terminal Domain. Biochemistry 53: 1801-1809
21. Weins A, Schlondorff J, Nakamura F, Denker B, Hartwig J, Stossel T and Pollak M (2007). Disease-associated mutant a-actinin-4 reveals a mechanism for regulating its F-actin-binding affinity. PNAS 104 (41): 16080-16085
22. Winder S.J., Hemmings L., Maciver S.K., Bolton S.J., Tinsley J.M., Davies K.E., Critchley D.R. and Kendrick-Jones J. (1995). Utrophin actin binding domain: analysis of actin binding and cellular targeting. Journal of Cell Science 108: 63-71
23. Belin BJ, Goins LM and Mullins RD (2014). Comparative analysis of tools for live cell imaging of actin network architecture. Bioarchitecture 4 (6): 189-202
24. Keep N, Winder S, Moores CA, Walke S, Norwood F and Kendrick-Jones J (1999). Crystal structure of the actin-binding region of utrophin reveals a head-to-tail dimer. Structure 7: 1539-1546
25. Galkin V, Orlova A, VanLoock M and Egelman E (2003). Do the Utrophin Tandem Calponin Homology Domains Bind F-actin in a Compact or Extended Conformation? Journal of Molecular Biology 331 (5): 967-972
26. Broderick M, Bobkov A and Winder S (2012). Utrophin ABD binds to F-actin in an open conformation. FEBS 2 (1): 6-11
27. Schmoller K, Lieleg O and Bausch A (2008). Internal stress in kinetically trapped actin bundle networks. Soft Matter 4: 2365-2367
28. Jensen M, Morris E and Weitz D (2015). Mechanics and dynamics of reconstituted cytoskeletal systems. Biochimica et Biophysica Acta 1853 (11): 3038-3042
29. Charras G, Coughlin M, Mitchison T and Mahadevan L (2008). Life and Times of a Cellular Bleb. Biophysical Journal 94 (5): 1836-1853
30. Charras G, Hu C, Coughlin M and Mitchison T (2006). Reassembly of contractile actin cortex in cell blebs. J Cell Bio 175 (3): 477-490
31. Fackler O and Grosse R (2008). Cell motility through plasma membrane blebbing. J Cell Bio 181 (6): 879-884
32. Gauthier N, Fardin M, Roca-Cusachs P and Sheetz M (2011). Temporary increase in plasma membrane tension coordinates the activation of exocytosis and contraction during cell spreading. PNAS 108 (35): 14467-14472
33. Miller A (2011). The Contractile Ring. Current Biology 21(24): 976-978

Chapter 6 – Concluding Remarks

One of the most intriguing properties of the actin cytoskeleton is its ability to convert a molecular process i.e. actin polymerization into work in the form of protrusive force. Not only is this biological system able to exert force but it is also subject to a range of mechanical loads that shape its structure and function. The work presented in this dissertation highlights the significance of these physical parameters in regulating actin network assembly.

At the leading edge of a migrating cell, nucleating actin structures are subject to two types of resisting forces: internal drag forces due to molecular tethering effects to the nucleating surface and global opposing forces due to physical barriers such as the plasma membrane. In chapters 2 and 3, we explored the effect of load force on branched actin network polymerization and showed that resistance makes these structures stronger and more efficient. Additionally, in the absence of external load, we hypothesized that changes in the biochemical composition of these networks modulate dynamic properties of growth by generating different levels of internal drag forces. These forces highly affect the molecular composition, growth velocity, geometry and mechanical properties of resulting actin structures. Meanwhile, the later harnesses the gained resistance to build more power and generate protrusive forces resulting in an overall forward motion.

A crucial component to these systems and to the actin cytoskeleton are actin binding proteins that bind individual actin filaments and regulate their structure and function. While we characterized the bulk response of actin structures to mechanical perturbations in chapters 2-3, we set to understand how these loads propagate to the individual actin filaments and their binding partners in chapters 4-5. Using a multiscale approach, we showed that actin binding proteins are sensitive to actin filaments' mechanical state. This mechanosensitivity could be at the origin of the differential distribution of ABPs in a common cellular environment. Our observations of linear scaling of protein bias in binding to the stretch state of an actin filament has further allowed us to extend this concept into a molecular tool that serves as a force sensor intracellularly.

What we hope to have conveyed through this work is the significance of mechanical forces in regulating cellular processes that are otherwise explored solely with respect to their molecular signaling pathways. Our development of a biosensor based on utrophin's actin binding domain will allow for future exploration of the role of force in the context of cytoskeleton as well as other biological phenomena. This force sensor can be employed as a tracking tool of intracellular forces and their variation in conjunction with biochemical processes. In addition to mapping out forces, it can be used to explore the mechanosentive binding of other actin binding proteins based on co-localization indices with the probe.

The emergence of the field of mechanobiology over the past decade has been in light of studies of the role of mechanical properties of extracellular environment and cellular structure in regulating normal phenotype and activity. Meanwhile, over the past 5 years, recent advances in electron microscopy has allowed us to zoom closer to intracellular structures and study them from a dynamic perspective. In fact, resolving the actin filament down to 10Å resolution has confirmed previous hypothesis that the structure is polymorphic and can adopt multiple states. As a semi-flexible polymer, the actin filament has long been thought to respond to mechanical perturbations by altering its fluctuation spectrum. The added notion of structural polymorphism rendered the multitude of states that the filament can adopt relevant to the actin binding proteins. In this thesis, we addressed the mechanical regulation of protein binding to actin filaments. We foresee that several other cytoskeletal proteins are either mechanosensitive or bind cooperatively/competitively to other mechanosensitive proteins.

In order to further understand the mechanoregulation of the cytoskeleton several questions remain to be answered in the future. How do actin binding proteins sense changes in the mechanical state of the filament? First, being able to understand the effect of force not only on the fluctuation spectrum of the filament but also on its twist will be key to understanding how these perturbations propagate to the ABP binding length scale. Second, additional studies are needed to shed light on the mechanism of force sensing. Does force regulate protein binding by changing the filament conformation itself or the protein conformation? We postulate that bias in binding could either be achieved by locking the filament in a favorable conformation that the protein can dock to or by changing the protein orientation itself in a way that minimizes steric hindrance on the filament. Lastly, breaking down the characteristics of the biased binding in terms of on-rate and off-rate will be significant for establishing the mechanism of mechanosensitivity.

Several applications can arise from this phenomenon. If force can be used as a tool for directing localization of actin binding proteins, then one can harness the activity of these proteins in different contexts and biological processes. Additionally, probes can be potentially created as chimeras of a mechanosensitive binding domain and a potent domain with the first aimed at directing the localization of the complex and the second aimed at fulfilling a cytoskeletal activity. Lastly, with the cytoskeleton serving many biological functions while providing cellular integrity and structural support, its malfunction is associated with several diseases. One can imagine extending the concept of ABP mechanoregulation and its potential application to restructuring cytoskeletal elements and recovering cytoskeletal function.